

**TIME-LAPSE SEISMIC MODELING AND PRODUCTION DATA
ASSIMILATION FOR ENHANCED OIL RECOVERY AND
CO₂ SEQUESTRATION**

A Dissertation

by

AJITABH KUMAR

Submitted to the Office of Graduate Studies of
Texas A&M University
in partial fulfillment of the requirements for the degree of

DOCTOR OF PHILOSOPHY

December 2008

Major Subject: Petroleum Engineering

**TIME-LAPSE SEISMIC MODELING AND PRODUCTION DATA
ASSIMILATION FOR ENHANCED OIL RECOVERY AND
CO₂ SEQUESTRATION**

A Dissertation

by

AJITABH KUMAR

Submitted to the Office of Graduate Studies of
Texas A&M University
in partial fulfillment of the requirements for the degree of

DOCTOR OF PHILOSOPHY

Approved by:

Chair of Committee,	Akhil Datta-Gupta
Committee Members,	Christine Ehlig-Economides
	Daulat D. Mamora
	Richard L. Gibson, Jr.
Head of Department,	Stephen A. Holditch

December 2008

Major Subject: Petroleum Engineering

ABSTRACT

Time-Lapse Seismic Modeling and Production Data Assimilation
for Enhanced Oil Recovery and CO₂ Sequestration. (December 2008)

Ajitabh Kumar, B.Tech., Indian School of Mines, Dhanbad;

M.S., The University of Texas at Austin

Chair of Advisory Committee: Dr. Akhil Datta-Gupta

Production from a hydrocarbon reservoir is typically supported by water or carbon dioxide (CO₂) injection. CO₂ injection into hydrocarbon reservoirs is also a promising solution for reducing environmental hazards from the release of green house gases into the earth's atmosphere. Numerical simulators are used for designing and predicting the complex behavior of systems under such scenarios. Two key steps in such studies are forward modeling for performance prediction based on simulation studies using reservoir models and inverse modeling for updating reservoir models using the data collected from field.

The viability of time-lapse seismic monitoring using an integrated modeling of fluid flow, including chemical reactions, and seismic response is examined. A comprehensive simulation of the gas injection process accounting for the phase behavior of CO₂-reservoir fluids, the associated precipitation/dissolution reactions, and the accompanying changes in porosity and permeability is performed. The simulation

results are then used to model the changes in seismic response with time. The general observation is that gas injection decreases bulk density and wave velocity of the host rock system.

Another key topic covered in this work is the data assimilation study for hydrocarbon reservoirs using Ensemble Kalman Filter (EnKF). Some critical issues related to EnKF based history matching are explored, primarily for a large field with substantial production history. A novel and efficient approach based on spectral clustering to select ‘optimal’ initial ensemble members is proposed. Also, well-specific black-oil or compositional streamline trajectories are used for covariance localization. Approach is applied to the Weyburn field, a large carbonate reservoir in Canada. The approach for optimal member selection is found to be effective in reducing the ensemble size which was critical for this large-scale field application. Streamline-based covariance localization is shown to play a very important role by removing spurious covariances between any well and far-off cell permeabilities.

Finally, time-lapse seismic study is done for the Weyburn field. Sensitivity of various bulk seismic parameters viz velocity and impedance is calculated with respect to different simulation parameters. Results show large correlation between porosity and seismic parameters. Bulk seismic parameters are sensitive to net overburden pressure at its low values. Time-lapse changes in pore-pressure lead to changes in bulk parameters like velocity and impedance.

DEDICATION

To my family members and teachers

ACKNOWLEDGEMENTS

I would like to thank Dr. Akhil Datta-Gupta for guiding and supporting this research work. I would also like to thank Dr Richard Gibson, Jr. for his guidance. I would like to thank Tarun Kashib and David Cooper of EnCana Corporation for providing Weyburn field data. I would like to thank Texas A&M Supercomputing Facility and Texas Tech High Performance Computing Centre (HPCC) for their support with computational resources. I would also like to thank David Chaffin, Alan Sill and Ravi Vadapalli of Texas Tech University for taking care of administrative and software licensing aspects. I would like to thank Long Nghiem of CMG for GEM-GHG license. I would like to thank students at MCERI, Adedayo, Alvaro, Deepak, Eduardo, Hao, Ichiro, Jiang, Jichao, Jong, Matt, Prannay, Sarwesh, Shingo, Xianlin and Yonnie, for their company.

TABLE OF CONTENTS

	Page
ABSTRACT.....	iii
DEDICATION.....	v
ACKNOWLEDGEMENTS.....	vi
TABLE OF CONTENTS	vii
LIST OF FIGURES.....	ix
LIST OF TABLES	xix
CHAPTER	
I INTRODUCTION.....	1
1.1. Literature Review and Present Status	2
1.2. Objectives of Study.....	5
II TIME-LAPSE SEISMIC MONITORING OF CO ₂ SEQUESTRATION	7
2.1. Introduction and Background	7
2.2. Compositional Modeling of CO ₂ Sequestration with Reactive Transport	10
2.3. Models for Time-Lapse Seismic Monitoring of CO ₂ Sequestration.....	20
2.4. Results and Discussion.....	27
III LARGE-SCALE DATA ASSIMILATION USING ENSEMBLE KALMAN FILTER.....	41
3.1. Introduction	41
3.2. Data Assimilation Methodology.....	42
3.3. Application and Results	57
IV TIME-LAPSE SEISMIC STUDY OF THE WEYBURN FIELD	77
4.1. Introduction	77
4.2. Pore-pressure and Pore-fluid Discrimination for the Weyburn Field.....	78

CHAPTER	Page
V CONCLUSIONS AND RECOMMENDATIONS	118
5.1. Large-Scale Hydrocarbon Reservoir Data Assimilation.....	118
5.2. Time-Lapse Seismic Monitoring of CO ₂ Sequestration.....	120
5.3. Recommendations.....	121
REFERENCES.....	123
APPENDIX I: PROPERTIES OF CO ₂ AND CO ₂ -H ₂ O MIXTURE.....	130
APPENDIX II: ROCK PHYSICS MODEL FOR WEYBURN OILFIELD	141
VITA.....	146

LIST OF FIGURES

	Page
Figure 2.1: (a) Permeability and (b) porosity profiles for small correlation length.....	13
Figure 2.2: (a) Permeability and (b) porosity profiles for large correlation length.....	13
Figure 2.3: (a) Effect of brine salinity on CO ₂ solubility (as mole fractions) in the aqueous phase at 80°C and (b) effect CO ₂ dissolution on brine density (in lb/cu ft) at 80°C and 20.7 MPa.....	15
Figure 2.4: (a) Gas saturation, and (b) oil saturation at 6 years (end of gas injection) for heterogeneous field with small correlation length.....	29
Figure 2.5: (a) Pressure, and (b) CO ₂ concentration in brine at 6 years (end of gas injection) for heterogeneous field with small correlation length.....	29
Figure 2.6: (a) Salinity (in ppm) and (b) brine density (in kg/m ³) at 6 years (end of gas injection) for heterogeneous field with small correlation length.....	31
Figure 2.7: (a) Oil density (in kg/m ³), and (b) gas density (in kg/m ³) at 6 years (end of gas injection) for heterogeneous field with small correlation length.....	31
Figure 2.8: Moles of Calcite precipitated at (a)100 years, and (b) 1000 years.....	32
Figure 2.9: Moles of Kaolinite precipitated at (a)100 years, and (b) 1000 years	32
Figure 2.10: Moles of Anorthite precipitated at (a)100 years, and (b) 1000 years	33
Figure 2.11: (a), (b), (c) and (d) represents difference of V _p (in km/s) between t= 6, 10,100 and 1000 years respectively with t=0 years for weakly correlated heterogeneous model	33

Figure 2.12: (a) and (b) represent difference of intercept between $t= 10$ and 1000 years respectively with $t=0$ years for weakly correlated heterogeneous model. (c) and (d) represent same profiles for gradient	34
Figure 2.13: Variation of reflection coefficient values with time and angle of incidence for weakly correlated heterogeneous model	34
Figure 2.14: (a) Gas saturation, and (b) gas density (in kg/m^3) at 6 years (end of gas injection) for heterogeneous field with large correlation length	37
Figure 2.15: (a) Pressure (in MPa) profile, and (b) brine density (in kg/m^3) at 6 years (end of gas injection) for heterogeneous field with large correlation length	37
Figure 2.16: (a), (b), (c) and (d) represents difference of V_p (in km/s) between $t= 6, 10, 100$ and 1000 years respectively with $t=0$ years for heterogeneous field with large correlation length.....	38
Figure 2.17: (a) and (b) represent difference of intercept between $t= 10$ and 1000 years respectively with $t=0$ years for heterogeneous field with large correlation length. (c) and (d) represent same profiles for gradient	39
Figure 2.18: (a) and (b) represents difference of intercept and gradient at 10 years respectively with $t=0$ years for case with no chemical reaction	39
Figure 2.19: Variation of reflection coefficient values with time and angle of incidence for heterogeneous field with large correlation length.....	40
Figure 2.20: Fractional changes in (a) intercept, and (b) gradient due to chemical activities of brine at 10 years for heterogeneous field with large correlation length	40
Figure 3.1: Probability density propagation using ensemble Kalman filter (EnKF). The three phases are (i) drift due to component of object dynamics, (ii) diffusion due to the random component, and (iii) reactive reinforcement due to observation.....	48
Figure 3.2: Schematic of EnKF based data assimilation	50

Figure 3.3: Production history and forecast, Weyburn field, Saskatchewan (adapted from Burrowes, 2001).....	59
Figure 3.4: (a) True Permeability Field for 2D synthetic case, and (b) streamlines for one production well used for localization.....	61
Figure 3.5: (a) Streamlines for time of flight=1000 days, (b) streamlines for time of flight=5000 days, and (c) extra volume swept between the two time of flight values.	61
Figure 3.6: Field water cut before history-match for (a) all 100 members, (b) selected 40 members. Thick black curve shows the response for true model.....	62
Figure 3.7: Field water cut after history-match for (a) all 100 members, (b) selected 40 members. Thick black curve shows the response for true model.....	63
Figure 3.8: (a) Swept pore volume (in cu ft), and (b) differential swept pore volume (in cu ft) with time of flight increments for small section of Weyburn field	63
Figure 3.9: Spread in oil production rates for three wells using all 40 members	64
Figure 3.10: Spread in oil production rates for same three wells as in Figure 3.8, but for selected 20 members	64
Figure 3.11: Comparison of responses for mean permeability fields for all 40 members and the selected 20 members, (a) field oil production rate, and (b) field water-cut.....	65
Figure 3.12: Comparison of field water-cut from mean permeability fields for (a) selected 20 members, and (b) all 40 members.....	65
Figure 3.13: Comparison of field oil production rate from mean permeability fields for (a) selected 20 members, and (b) all 40 members	66

Figure 3.14: Mean permeability values (in md) for layer 6: (a) before history-matching, (b) after history-matching using all 40 members, and (c) after history-matching using selected 20 members.....	66
Figure 3.15: Three dimensional view of the Weyburn reservoir under study	69
Figure 3.16: Initial permeability (in md) for (a) layer 4 - Marly, (b) layer 10 - Upper Vuggy, and (c) layer 24 - Lower Vuggy.....	69
Figure 3.17: Final permeability (in md) after data assimilation using EnKF for (a) layer 4 - Marly, (b) layer 10 - Upper Vuggy, and (c) layer 24 - Lower Vuggy	70
Figure 3.18: Comparison of field oil production rates for mean permeability fields of initial ensemble and history-matched ensemble	70
Figure 3.19: Comparison of field (a) water-cut and (b) water injection rate for mean permeability fields of initial ensemble and history-matched ensemble	71
Figure 3.20: Comparison of field oil production rates for mean permeability fields of history-matched ensembles using EnKF with and without localization.....	71
Figure 3.21: Final permeability (in md) after data assimilation using localized EnKF for (a) layer 4 - Marly, (b) layer 10 - Upper Vuggy, and (c) layer 24 - Lower Vuggy.....	72
Figure 3.22: Oil production rates for well (a) 01_03-04, (b) 01_14-06, (c) 01_14-29, (d) 01_10-01, (e) 01_04-07, and (f) 01_10-32 using initial geologic models. Dark curves show the historical oil production rates for the same wells	72
Figure 3.23: Oil production rates for well (a) 01_03-04, (b) 01_14-06, (c) 01_14-29, (d) 01_10-01, (e) 01_04-07, and (f) 01_10-32 using updated models. Dark curves show the historical oil production rates for the same wells	73

Figure 3.24: (a) Histogram of lower vuggy permeability values before history matching, and after history matching (b) without localization and (c) with localization.....	73
Figure 3.25: (a) A two-dimensional synthetic permeability field with five-spot well pattern, and (b) compositional streamlines for the same	75
Figure 3.26: Compositional Streamlines for the Weyburn oilfield.....	76
Figure 3.27: Comparison of data assimilation results using black-oil and that using compositional model for small section of Weyburn field. (a) Field oil production rate using the means of initial geologic ensemble, and (b) using the means from final updated ensembles. Dark curves show the historical field oil production rate	76
Figure 4.1: Effect of porosity on P- and S-wave velocities (V_p and V_s) and impedances (I_p and I_s) for the marly section	83
Figure 4.2: Effect of porosity on P- and S-wave velocities (V_p and V_s) and impedances (I_p and I_s) for the upper vuggy section	83
Figure 4.3: Effect of porosity on P- and S-wave velocities (V_p and V_s) and impedances (I_p and I_s) for the lower vuggy section	83
Figure 4.4: Effect of net overburden pressure on P- and S-wave velocities (V_p and V_s) and impedances (I_p and I_s) for the marly section	84
Figure 4.5: Effect of net overburden pressure on P- and S-wave velocities (V_p and V_s) and impedances (I_p and I_s) for the upper vuggy section	84
Figure 4.6: Effect of net overburden pressure on P- and S-wave velocities (V_p and V_s) and impedances (I_p and I_s) for the lower vuggy section	84
Figure 4.7: Effect of supercritical CO ₂ saturation on P- and S-wave velocities (V_p and V_s) and impedances (I_p and I_s) for the marly section.....	85

Figure 4.8: Effect of supercritical CO ₂ saturation on P- and S-wave velocities (V_p and V_s) and impedances (I_p and I_s) for the upper vuggy section.....	85
Figure 4.9: Effect of supercritical CO ₂ saturation on P- and S-wave velocities (V_p and V_s) and impedances (I_p and I_s) for the lower vuggy section.....	85
Figure 4.10: Thickness averaged porosity maps for (a) marly, (b) upper vuggy(V1), (c) lower vuggy(V2), and (d) lower vuggy(V4+) sections.....	88
Figure 4.11: Thickness averaged permeability maps for (a) marly, (b) upper vuggy(V1), (c) lower vuggy(V2), and (d) lower vuggy(V4+) sections.....	89
Figure 4.12: Thickness averaged log permeability maps for (a) marly, (b) upper vuggy(V1), (c) lower vuggy(V2), and (d) lower vuggy(V4+) sections.....	90
Figure 4.13: Thickness averaged pressure profiles (in MPa) for marly section at times (a) November 2005, and (b) December 2004.....	91
Figure 4.14: Thickness averaged pressure profiles (in MPa) for upper vuggy(V1) section at times (a) November 2005, and (b) December 2004	91
Figure 4.15: Thickness averaged pressure profiles (in MPa) for lower vuggy(V2) section at times (a) November 2005, and (b) December 2004	92
Figure 4.16: Thickness averaged pressure profiles (in MPa) for lower vuggy(V4+) section at times (a) November 2005, and (b) December 2004	92
Figure 4.17: Thickness averaged CO ₂ mole fraction profiles for marly section at times (a) November 2005, and (b) December 2004.....	93
Figure 4.18: Thickness averaged CO ₂ mole fraction profiles for upper vuggy(V1) section at times (a) November 2005, and (b) December 2004	93
Figure 4.19: Thickness averaged CO ₂ mole fraction profiles for lower vuggy(V2) section at times (a) November 2005, and (b) December 2004	94

Figure 4.20: Thickness averaged CO ₂ mole fraction profiles for lower vuggy(V4+) section at times (a) November 2005, and (b) December 2004.....	94
Figure 4.21: Thickness averaged gas saturation profiles for marly section at times (a) November 2005, and (b) December 2004	95
Figure 4.22: Thickness averaged gas saturation profiles for upper vuggy(V1) section at times (a) November 2005, and (b) December 2004	95
Figure 4.23: Thickness averaged gas saturation profiles for lower vuggy(V2) section at times (a) November 2005, and (b) December 2004	96
Figure 4.24: Thickness averaged gas saturation profiles for lower vuggy(V4+) section at times (a) November 2005, and (b) December 2004	96
Figure 4.25: Thickness averaged P-wave velocity profiles (in m/sec) for marly section at times (a) November 2005, and (b) December 2004	97
Figure 4.26: Thickness averaged P-wave velocity profiles (in m/sec) for upper vuggy (V1) section at times (a) November 2005, and (b) December 2004.....	97
Figure 4.27: Thickness averaged P-wave velocity profiles (in m/sec) for lower vuggy (V2) section at times (a) November 2005, and (b) December 2004.....	98
Figure 4.28: Thickness averaged P-wave velocity profiles (in m/sec) for lower vuggy (V4+) section at times (a) November 2005, and (b) December 2004.....	98
Figure 4.29: Thickness averaged P-wave impedance profiles (in 10 ⁶ kg/m ² /sec) for marly section at times (a) November 2005, and (b) December 2004	99
Figure 4.30: Thickness averaged P-wave impedance profiles (in 10 ⁶ kg/m ² /sec) for upper vuggy(V1) section at times (a) November 2005, and (b) December 2004	99

Figure 4.31: Thickness averaged P-wave impedance profiles (in 10^6 kg/m ² /sec) for lower vuggy(V2) section at times (a) November 2005, and (b) December 2004	100
Figure 4.32: Thickness averaged P-wave impedance profiles (in 10^6 kg/m ² /sec) for lower vuggy(V4+) section at times (a) November 2005, and (b) December 2004	100
Figure 4.33: Thickness averaged S-wave velocity profiles (in m/sec) for marly section at times (a) November 2005, and (b) December 2004	101
Figure 4.34: Thickness averaged S-wave velocity profiles (in m/sec) for upper vuggy (V1) section at times (a) November 2005, and (b) December 2004.....	101
Figure 4.35: Thickness averaged S-wave velocity profiles (in m/sec) for lower vuggy (V2) section at times (a) November 2005, and (b) December 2004.....	102
Figure 4.36: Thickness averaged S-wave velocity profiles (in m/sec) for lower vuggy (V4+) section at times (a) November 2005, and (b) December 2004.....	102
Figure 4.37: Thickness averaged S-wave impedance profiles (in 10^6 kg/m ² /sec) for marly section at times (a) November 2005, and (b) December 2004	103
Figure 4.38: Thickness averaged S-wave impedance profiles (in 10^6 kg/m ² /sec) for upper vuggy (V1) section at times (a) November 2005, and (b) December 2004	103
Figure 4.39: Thickness averaged S-wave impedance profiles (in 10^6 kg/m ² /sec) for lower vuggy (V2) section at times (a) November 2005, and (b) December 2004	104
Figure 4.40: Thickness averaged S-wave impedance profiles (in 10^6 kg/m ² /sec) for lower vuggy (V4+) section at times (a) November 2005, and (b) December 2004	104

Figure 4.41: Scatterplot showing relationship between simulated impedance values and flow parameters for Weyburn field. (marly in red, upper vuggy in green, and lower vuggy in blue).....	105
Figure 4.42: Scatterplot showing relationship between simulated velocity values and flow parameters for Weyburn field. (marly in red, upper vuggy in green, and lower vuggy in blue)	106
Figure 4.43: Thickness averaged pressure difference maps in MPa for (a) marly, (b) upper vuggy(V1), (c) lower vuggy(V2), and (d) lower vuggy(V4+) sections	108
Figure 4.44: Thickness averaged CO2 mole fraction difference maps for (a) marly, (b) upper vuggy(V1), (c) lower vuggy(V2), and (d) lower vuggy(V4+) sections	109
Figure 4.45: Thickness averaged gas saturation difference maps for (a) marly, (b) upper vuggy(V1), (c) lower vuggy(V2), and (d) lower vuggy(V4+) sections	110
Figure 4.46: Thickness averaged P-wave velocity difference maps (in m/sec) for (a) marly, (b) upper vuggy(V1), (c) lower vuggy(V2), and (d) lower vuggy(V4+) sections	111
Figure 4.47: Thickness averaged P-wave impedance difference maps (in 10^6 kg/m ² /sec) for (a) marly, (b) upper vuggy(V1), (c) lower vuggy(V2), and (d) lower vuggy(V4+) sections	112
Figure 4.48: Thickness averaged S-wave velocity difference maps (in m/sec) for (a) marly, (b) upper vuggy(V1), (c) lower vuggy(V2), and (d) lower vuggy(V4+) sections	113
Figure 4.49: Thickness averaged S-wave impedance difference maps (in 10^6 kg/m ² /sec) for (a) marly, (b) upper vuggy(V1), (c) lower vuggy(V2), and (d) lower vuggy(V4+) sections	114

Figure 4.50: Scatterplot showing relationship between simulated time-lapse P-wave properties and time-lapse flow parameters for Weyburn field. (marly in red, upper vuggy in green, and lower vuggy in blue)	115
Figure 4.51: Scatterplot showing relationship between simulated time-lapse S-wave properties and time-lapse flow parameters for Weyburn field. (marly in red, upper vuggy in green, and lower vuggy in blue)	116
Figure 4.52: Two-way time averaged, squared P-wave impedance difference maps for (a) marly, (b) upper vuggy(V1), (c) lower vuggy(V2), and (d) lower vuggy(V4+) sections	117

LIST OF TABLES

	Page
Table 2.1: Reservoir model.....	13
Table 2.2: Hydrocarbon component properties and their initial concentration	14
Table 2.3: Aqueous species and their initial concentrations.....	16
Table 2.4: Minerals and their initial volume fractions	17
Table 2.5: Intra-aqueous reaction coefficients.....	17
Table 2.6: Mineral equilibrium reaction coefficients.....	17
Table 2.7: Rate dependent mineral reaction	19
Table 3.1: Key data for Weyburn field (Burrowes, 2001).....	58
Table 3.2: Geology of Weyburn field (Burrowes, 2001)	58
Table 3.3: Component information for the compositional simulation	75
Table 4.1: Correspondence between time-lapse sections and simulation model layers	82

CHAPTER I

INTRODUCTION

Hydrocarbon reservoir studies include three main steps. First reservoir models are generated using static information such as geological and geophysical data. Next, models are updated using dynamic information such as production and time-lapse seismic data. Finally, updated models are used for performance optimization and forecasting studies. The main focus of this study lies around the second step, i.e. updating prior geologic models using dynamic data. This step includes forward modeling to get the simulated response from the initial set of geologic models and an inversion study based on mismatch between their simulated response and observed field data.

An integrated data study may require simulating different processes. The forward modeling step may include flow simulation and rock-physics modeling. Flow simulation may include black-oil, compositional, geochemical or streamlines simulation. Rock-physics modeling may include bulk velocities, bulk moduli or similar parameter calculation. Hence, all these processes need to be numerically modeled for such a study. Also, various methods are used for an inverse study, of which the

This dissertation follows the style of *Petroleum Science and Technology Journal*.

Ensemble Kalman filter (EnKF) has received significant attention. It has emerged as a powerful yet simple method for assimilating complex data. It updates (or corrects) geologic models based on various covariances between the given set of models and has proved to be equally efficient for non-linear models like ocean and atmosphere modeling.

1.1.Literature Review and Present Status

1.1.1 Flow Simulation

For an oil-field under production using water and CO₂ injection, black-oil, compositional, geochemical, and/or streamline modeling are required to understand its behavior. Also, carbon dioxide injection into a reservoir is beneficial economically by enhanced crude production, but also environmentally by disposing CO₂ (carbon sequestration). Hence, important processes related to enhanced oil recovery as well as carbon sequestration need to be modeled for such studies. Kumar *et. al.* (2005) used compositional and geochemical modeling for flow simulation of carbon dioxide injection into brine aquifers. Key processes which need to be modeled for CO₂ injection in a hydrocarbon reservoir are hydrocarbon component interactions, CO₂ solubility in brine and resulting geochemical reactions in the reservoir. CO₂ interactions with hydrocarbon components are modeled using various equation-of-state (EOS) formulations such as Peng-Robinson EOS, while CO₂ solubility into brine is typically modeled using Henry's law. Different methods of modeling geochemical reactions are

suggested in literature including equilibrium constant based intra-aqueous reactions as well as rate dependent mineral reactions.

1.1.2 Rock-Physics Modeling

Time-lapse seismic data integration includes rock-physics modeling for calculating bulk properties of the reservoir. These properties include bulk moduli and velocities. Also, these bulk properties can be used to calculate the AVO (amplitude versus offset) parameters. Skorstad *et al.* (2006) used time-lapse seismic data to update the prior geologic models. Measurements on core samples have shown that the CO₂ can decrease the velocity of both compressional and shear waves by up to 10% (Wang and Nur, 1989; Wang *et al.*, 1998). Seismic monitoring of two basic categories of changes in reservoir conditions may be possible over the long term. First, the seismic response may be affected by changes in pore fluid properties because the injected CO₂ can exist in three separate forms, viz. supercritical fluid CO₂, gaseous CO₂, or dissolved CO₂ in aqueous solutions, depending on the brine salinity, pore pressures, and temperatures in the reservoir (Wang *et al.*, 1998). Second, the seismic response may change because of petrophysical alterations such as cementation, secondary porosity formation and compaction.

1.1.3 Data Assimilation

Data assimilation or history matching is the technique by which dynamic data comprising production responses and 4-D seismic surveys are used to build reservoir models that enable better prediction in model forecasts (Scorstad *et. al.*, 2006; Dong *et. al.*, 2006). A good history-matched reservoir model is one that is conditioned to all available production history while retaining prior geologic information. One such approach that has gained popularity in the recent past is the Ensemble Kalman Filter (EnKF). The EnKF uses covariances to update the model parameters sequentially as and when more data become available (Evensen, 2003). In other words, it starts with a number of initial geologic models and updates them sequentially for each time step for which data are available. It should be noted that the EnKF is optimal only in linear and Gaussian systems, and is sub-optimal for non-linear and non-Gaussian systems. Integrated data analysis requires simulating different processes and hence is computationally expensive when the number of models used is also large. Dong *et. al.*(2006) suggested selection of key models from a larger group of initial models by using analysis of the difference matrix of static measure for the whole set of geologic models available. However as flow simulation is a highly non-linear process, selection of models using only static measures may not be optimal. Also, a full flow simulation before the history match required for understanding the dynamic behavior of each model is also undesirable. In this study, a pseudo-dynamic difference measure based on streamline is proposed for member selection.

1.2.Objectives of Study

The main focus of this study is to use different production related information, such as well production rates and time-lapse seismic response changes, to update a group of large-size geologic models using the Ensemble Kalman filter. Three key issues studied are the selection of optimal initial members while preserving the spread of their dynamic response, localization of the large domain for removing spurious covariances, and usage of geology in handling the problems due to non-linearity of the system. Various linear and non-linear feature extraction methods have been tested to identify the key models to be used in conditioning.

Another focus area of this study is to understand the feasibility of seismic monitoring of CO₂ sequestration in carbonate reservoirs using an integrated flow simulation and seismic modeling study. While combining reservoir simulation and time-lapse studies, it is important to account for the various subsurface physical and chemical processes that occur during CO₂ sequestration. Reservoir simulation-assisted time-lapse studies require these processes to be modeled correctly. Compositional simulation coupled with reactive transport is needed to correctly simulate the CO₂ movement during the sequestration process. The sequestration of CO₂ into geologic formations, specifically into existing and depleted oil and gas reservoirs, is a promising solution for reducing environmental hazards from the release of green house gases into the earth's atmosphere. A critical component of long term sequestration will be our ability to

adequately monitor the movement of CO₂ fronts in the subsurface. This work examines the viability of time-lapse seismic monitoring using an integrated modeling of fluid flow, including chemical reactions, and seismic response. Modeling of CO₂ injection is complicated by the various interactions between CO₂, reservoir fluids and the minerals in the formation. These interactions change fluid and bulk rock properties with time, which in turn impact the seismic signatures. The gas injection process accounting for the phase behavior of CO₂-reservoir fluids, the associated precipitation/dissolution reactions and the accompanying changes in porosity and permeability is simulated. The simulation results are then used to model the changes in seismic response with time. The general observation is that gas injection decreases bulk density and wave velocity of the host rock system. Seismic amplitude attributes therefore change with time as well, and these effects provide a tool for tracking the movement of the CO₂ front. Analysis of the results also confirms that much of the change can be attributed to chemical effects which should therefore be considered in studies of long term sequestration projects. Finally, sensitivities of simulated time-lapse seismic parameters to simulated time-lapse flow-related parameters are studied to understand the underlying relationships.

CHAPTER II

TIME-LAPSE SEISMIC MONITORING OF CO₂ SEQUESTRATION*

2.1. Introduction and Background

Carbon dioxide sequestration remains a compelling and important topic as a potential approach for mitigating the effects of greenhouse gases on global warming (*e.g.*, Hepple and Benson, 2005; Bachu, 2003; Grimston *et. al.*, 2001). While CO₂ can be sequestered in oceanic or terrestrial biomass, the most mature and effective technology currently available is sequestration in known hydrocarbon reservoirs (Hepple and Benson, 2005). However, challenges in the design and implementation of sequestration projects remain, especially over long time scales (Wilson and Monea, 2004). One problem is that the low density and viscosity of CO₂ under subsurface conditions may significantly increase its risk of leaking from the sequestration site into overlying rock compared to other liquid wastes (Tsang *et. al.*, 2002). Furthermore, the CO₂ will likely interact chemically with the rock in which it is stored, so that understanding and predicting its behavior during sequestration is difficult. Leaks of CO₂ can lead to such

*Reprinted with permission from "Modeling Time Lapse Seismic Monitoring of CO₂ Sequestration in Hydrocarbon Reservoirs Including Compositional and Geochemical Effects" by Kumar, A., Datta-Gupta, A., Shekhar, R., and Gibson, R.L., 2008, *Petroleum Science and Technology*, 26:887-911, Copyright 2008 by Taylor & Francis.

problems as acidification of ground water and killing of plant life, in addition to contamination of the atmosphere. The development of adequate policies and regulatory systems to govern sequestration therefore requires improved characterization of the media in which CO₂ is stored and the development of advanced methods for detecting its flow and movement.

Existing and depleted oil and gas reservoirs are attractive candidates for CO₂ sequestration for two principal reasons. First, the economic benefits associated with enhanced oil recovery through CO₂ injection are commercially proven and the method is widely practiced by the industry. This industrial experience can be an invaluable resource in the sequestration effort. Second, oil and gas reservoirs are likely to provide abundant data sources for subsurface characterization, design and performance assessment of any potential CO₂ sequestration project. These data will result in important constraints on reservoir properties such as porosity, permeability and seismic velocity.

Both, laboratory data and field experiments, suggest that the influence of CO₂ on seismic properties is sufficiently strong to be detectable, confirming that seismic methods are viable monitoring tools, especially at the interwell scale. Measurements on core samples have shown that the CO₂ can decrease the velocity of both compressional and shear waves by up to 10% (Wang and Nur, 1989; Wang *et. al.*, 1998). Likewise, some field experiments have successfully measured such velocity variations using

crosswell techniques (Harris *et. al.*, 1995; Nolen-Hoeksema *et. al.*, 1995). Seismic monitoring of two basic categories of changes in reservoir conditions may be possible over the long term. First, seismic response may be affected by changes in pore fluid properties, because the injected CO₂ can exist in three separate phases, viz. supercritical fluid CO₂, gaseous CO₂, or dissolved in aqueous solutions, depending on the pore pressures and temperatures in the reservoir (Wang *et al.*, 1998). Second, the seismic response may change because of petrophysical alterations such as cementation, secondary porosity formation and compaction.

In this chapter, the feasibility of seismic monitoring of CO₂ sequestration in carbonate reservoirs using an integrated flow simulation and seismic modeling of the process is examined. While combining reservoir simulation and time-lapse studies, it is important to account for the various subsurface physical and chemical processes that occur during CO₂ sequestration. Carbon-dioxide injection can have a large impact on reservoir fluids, as it changes the physical and chemical properties of all reservoir gas, oil, and brine contacted. One of the key fluid properties altered upon CO₂ mixing is density. Also, when carbon-dioxide comes in contact with formation brine, it forms carbonic acid which reacts with the formation minerals and alters rock composition as well as brine salinity. Reservoir simulation assisted time-lapse studies require these processes to be modeled correctly. Compositional simulation coupled with reactive transport is needed to correctly simulate the CO₂ movement during the sequestration process.

The organization of our paper is as follows. First, the flow simulator used in this study and the modeling of CO₂-reservoir fluid phase behavior, reactive transport and the associated precipitation/dissolution reactions are discussed briefly. One of the goals of our study is to investigate the role of geochemical reactions and their implications on the time-lapse seismic monitoring of CO₂ fronts. Next, the details of modeling the seismic response from the CO₂ injection are discussed. Specifically, the rock-physics models and the relevant correlations used to derive the seismic attributes used for detecting the CO₂ movement in the reservoir are outlined. Finally, CO₂ injection in a five-spot pattern with two different spatial distributions of permeability is illustrated using our approach.

2.2. Compositional Modeling of CO₂ Sequestration with Reactive Transport

Modeling of CO₂ sequestration is complicated by the many different mechanisms and complex interactions that contribute to the sequestration process. First, the injected CO₂ can be trapped in a separate phase. Depending upon the reservoir conditions, the CO₂ phase can be gaseous or liquid-like, although under most conditions (reservoir depths >800 m) the CO₂ is expected to be in a supercritical state with liquid-like properties. The CO₂ can be trapped structurally or via hydrodynamic mechanisms. The structural trapping of the CO₂ will rely on the integrity of the reservoir seals because the buoyancy forces will cause the CO₂ to move towards the top of the structure. On the other hand, the hydrodynamic trapping of CO₂ will be governed by rock-fluid

properties such as permeability, relative permeabilities and also the phase behavior of the reservoir fluids and injected CO₂. Specifically, the phase behavior of CO₂ will play a significant role in the trapping of CO₂ as a residual (immobile) phase which can contribute substantially to the overall sequestration (Kumar et al., 2005). Another important mechanism for sequestration will be CO₂ dissolution in the reservoir brine. The dissolved CO₂ can migrate away from the injection point by convective and dispersive forces. However, such migration can only be significant over very long time scales as the water velocity is likely to be small in the reservoir. More importantly, the dissolution of CO₂ will lead to acidification of the in-situ brine. The low pH brine can trigger a variety of geochemical reactions in the reservoir leading to mineral precipitation and dissolution. In particular, the CO₂ trapping in carbonate minerals can be a significant sequestration mechanism. The mineral precipitation can also cause changes in reservoir properties such as porosity and permeability. All these will impact CO₂ transport calculations.

GEM simulator developed by the Computer Modeling Group to model CO₂ sequestration is used (Nghiem, 2002; 2003). This is a fully compositional simulator that incorporates phase and chemical equilibrium models and rate dependent mineral dissolution/precipitation reactions. The strongly coupled flow and reactive transport equations are solved simultaneously using an adaptive implicit method (Nghiem, 2002). Also GEM can be used to model gas trapping with Land's equation (Kumar et al., 2005), and this capability, along with the other features, makes it a better candidate for

the research problem than other commercial simulators. The reservoir model studied here is a two dimensional model of a carbonate reservoir (Table 2.1). Two different permeability distributions are considered. The first case has a low spatial correlation (correlation length, $\lambda_D \sim 0.01$) and thus, almost a random distribution of permeability. The second case has a high spatial correlation ($\lambda_D \sim 0.3$) leading to distinct flow channels. A porosity-permeability relationship representative of a carbonate reservoir was used in this study (Jennings and Lucia, 2003). The permeability and porosity distributions for these two cases are shown in Figure 2.1 and Figure 2.2 respectively.

CO₂ sequestration under post-waterflood conditions is examined, and thus a high water saturation of 60% is used as the initial condition. Critical properties and initial concentration for various components used in the study are shown in Table 2.2. A five spot pattern with a central injector and four producers is simulated with CO₂ injection for six years, after which all the wells are shut down. The results at 6 years (end of gas injection), 10 years, 100 years and 1000 years are then used to model the seismic response corresponding to the reservoir conditions. The seismic modeling will be discussed in the next section. Some specific details related to the flow simulation are briefly discussed.

Table 2.1: Reservoir model

Grid	41 × 41 × 1
Grid Size (m)	
$\Delta x = \Delta y$	22.43
Δz	20
Heterogeneity	
Case I	Weakly correlated
Case II	Strongly correlated
Reservoir compressibility	1.E-08
Reference pressure	1 MPa
Initial reservoir pressure	19.58 MPa
Initial water saturation	0.6

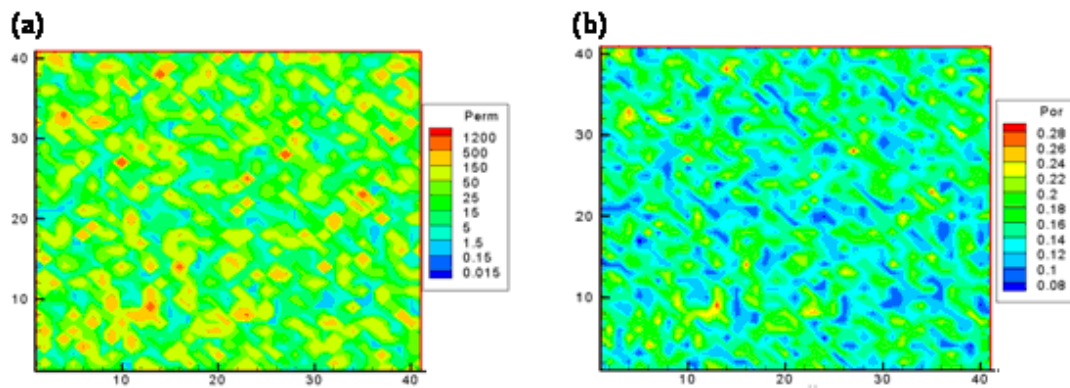
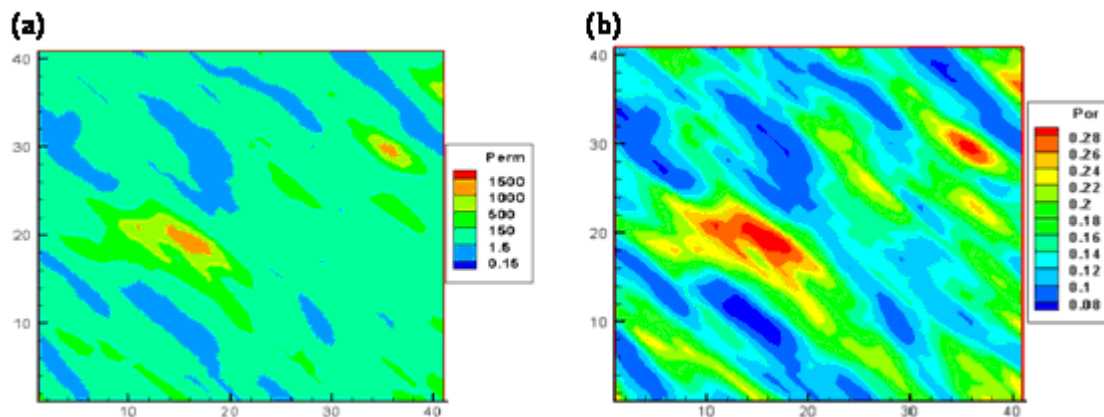
**Figure 2.1: (a) Permeability and (b) porosity profiles for small correlation length****Figure 2.2: (a) Permeability and (b) porosity profiles for large correlation length**

Table 2.2: Hydrocarbon component properties and their initial concentration

Name	Molecular Weight (g)	Boiling Point (°C)	Critical Pressure (atm)	Critical Temperature (°K)	Initial Overall Mole Fraction
CO2	44.01	-78.45	72.9	304.7	0.001
C7+1	107.779	110.001	27.950	465.618	0.33
C7+2	198.562	259.248	16.846	587.799	0.33
C7+3	335.198	432.628	10.916	717.717	0.339

2.2.1 Phase Behavior and CO₂ Dissolution

The phase behavior of the CO₂ and reservoir fluids controls the CO₂ dissolution, which in turn affect the mineral precipitation and dissolution. Oleic and gaseous phase equilibria are calculated using the Peng-Robinson equation of state (Li and Nghiem, 1986). For the gas-brine equilibria, it is assumed that the dissolution occurs instantaneously, and the gas and the aqueous phase are in thermodynamic equilibrium. The equilibrium conditions require that the fugacities of the components in the gaseous and the aqueous phases be equal as shown in Eqn. 2.1 below:

$$f_{ig} - f_{iw} = 0, \quad i = 1, \dots, n_g \quad (2.1)$$

Here n_g is the number of components in the gas phase and f_{ig} and f_{iw} are the fugacities of component 'i' in gaseous and aqueous phase respectively. The gas phase fugacities are computed using the Peng-Robinson equation of state whereas the fugacities of the components in the aqueous phase are given by the Henry's law (Eqn. 2.2),

$$f_{iw} = y_{iw} H_i \quad (2.2)$$

where H_i is the Henry's law constant for component i and is a function of salinity (Li and Nghiem, 1986). Figure 2.3 shows the CO_2 solubility in brine and the effects of CO_2 dissolution on brine density used in this study. These results were derived from various experiments and correlations reported in the literature (Firoozabadi *et al.*, 1988; Garcia, 2001; Hnedkovský *et al.*, 1996; Parkinson and Nevers, 1969; Rumpf *et al.*, 1994; Simonson *et al.*, 1994; Scharlin, 1996; Spycher *et al.*, 2002; Teng and Yamasaki, 1998; Teng *et al.*, 1997; Wagner and Pruß, 2002). Appendix I lists some more relevant properties of CO_2 and CO_2 - H_2O mixture. These results, along with previous validations presented in paper SPE89343 (Kumar *et al.*, 2005), show that the simulations provide accurate solutions. Also, in order to maintain stability of the system, injection rate was kept low relative to the pore volume. For any time-step the injected fluid volume in any grid was less than one-third of its pore-volume.

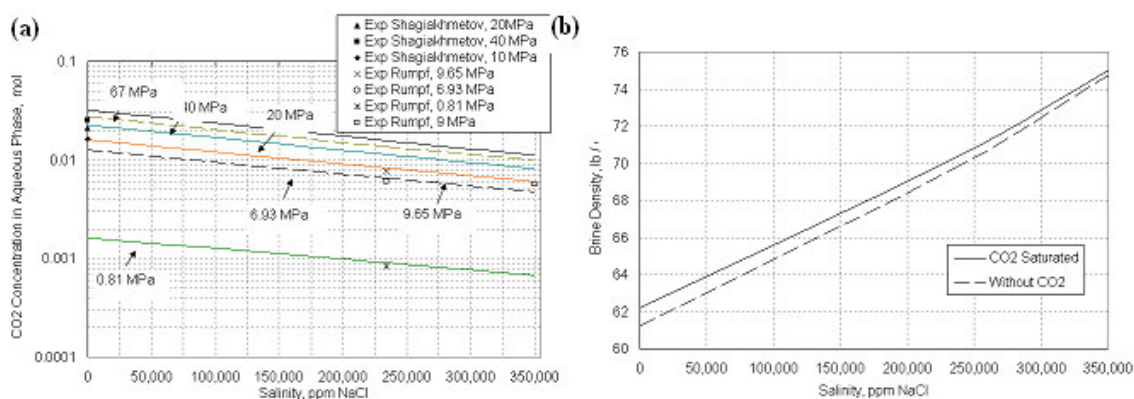


Figure 2.3: (a) Effect of brine salinity on CO_2 solubility (as mole fractions) in the aqueous phase at 80°C and (b) effect CO_2 dissolution on brine density (in lb/cu ft) at 80°C and 20.7 MPa

2.2.2 Modeling Geochemical Reactions

The storage of CO₂ as a mineral precipitate can be an important mechanism for sequestration. Carbon-dioxide injection into the formation leads to the formation of Carbonic acid, which can trigger a variety of chemical reactions (Stumm and Morgan, 1996; Lichtner *et. al.*, 1996). These reactions also alter rock composition and brine salinity, and any consequent changes in density or bulk modulus of the pore fluids will affect the seismic response of the system. Of the full set of geochemical species only a few, viz. 3 aqueous reactions and 3 mineral reactions, are considered to represent the basic dynamics of the chemical transformations during CO₂ injection. Table 2.3 and Table 2.4 show different aqueous species and minerals considered. Table 2.5 and Table 2.6 show various aqueous and mineral reactions included in this study.

Table 2.3: Aqueous species and their initial concentrations

Species Name	Initial Molality (Moles/kg of water)
H ⁺	1E-07
Ca ⁺⁺	9.118492E-05
Al ⁺⁺⁺	2.317806E-11
SiO ₂ (aq)	2.345433E-08
Na ⁺	0.5
Cl ⁻	0.52
HCO ₃ ⁻	2.489299E-02
CO ₃ ⁻⁻	1.170273E-05
OH ⁻	5.456322E-07

Table 2.4: Minerals and their initial volume fractions

Mineral	Chemical formula	Molecular weight	Density(kg/m ³)	Initial volume fraction
Calcite	CaCO ₃	100.0869	2710	0.97
Kaolinite	Al ₂ Si ₂ O ₅ (OH) ₄	258.1616	2410	0.0176
Anorthite	CaAl ₂ Si ₂ O ₈	278.2082	2740	0.0088

Table 2.5: Intra-aqueous reaction coefficients

Reaction	Coeff 1	Coeff 2	Coeff 3	Coeff 4	Coeff 5
CO ₂ (aq) + H ₂ O = H ⁺ + HCO ₃ ⁻	-6.549243	0.009002	-1.02E-04	2.76E-07	-3.56E-10
HCO ₃ ⁻ = H ⁺ + CO ₃ ⁻	10.60796	-0.01277	1.20E-04	-3.02E-07	2.69E-10
H ⁺ + OH ⁻ = H ₂ O	14.92816	-0.04188	1.97E-04	-5.55E-07	7.58E-10

Table 2.6: Mineral equilibrium reaction coefficients

Reaction	Coeff 1	Coeff 2	Coeff 3	Coeff 4	Coeff 5
Calcite + H ⁺ = Ca ⁺⁺ + HCO ₃ ⁻	31.74573	-0.20125	-1.02E-04	2.76E-07	-3.56E-10
Kaolinite + 6H ⁺ = 5 H ₂ O + 2Al ⁺⁺⁺ + 2SiO ₂ (aq)	2.068889	-0.01427	1.20E-04	-3.02E-07	2.69E-10
Anorthite + 8H ⁺ = 4H ₂ O + Ca ⁺⁺ + 2Al ⁺⁺⁺ + 2SiO ₂ (aq)	9.729544	-0.0989	1.97E-04	-5.55E-07	7.58E-10

Chemical equilibrium requires the forward and backward reaction rates to be the same for each reaction. In GEM, the simulator used in this study, chemical equilibrium is modeled using the equality conditions of Eqn. 2.3 (Nghiem, 2002; 2003).

$$Q_{\alpha}^a - K_{eq,\alpha}^a = 0, \quad \alpha = 1, \dots, R_{aq} \quad (2.3)$$

where Q_{α}^a is the activity product for the intra-aqueous reaction α given by,

$$Q_{\alpha}^a = \prod_{k=1}^{n_s} a_k^{v_{k\alpha}^a}, \quad \alpha = 1, \dots, R_{aq}, \quad a_k \text{ is the activity coefficient for component } k, \quad v_{eq,\alpha}^a$$

is the stoichiometric coefficient of the intra-aqueous reaction α , and R_{aq} is the number

of aqueous reactions. Also, $K_{eq,\alpha}^a$ is the chemical equilibrium constant for the intra-aqueous reaction α and is given as follows,

$$K_{eq,\alpha}^a = \exp\left[-\frac{1}{RT} \sum_{k=1}^{n_s} \nu_{k\alpha}^a (\Delta G_f^o)_k\right], \quad \alpha = 1, \dots, R_{aq}$$

where R is the Gas constant, T is the temperature, and ΔG^o is the standard-state Gibbs energy.

Activity coefficients for water and minerals are taken to be unity. Aqueous solutions are considered ideal, and hence activity coefficients for aqueous species are taken equal to their molalities (moles/kg of water). The chemical equilibrium constant is modeled as a fourth order polynomial of temperature (Nghiem, 2003; Stumm and Morgan, 1996),

$$\log(K_{eq,\alpha}) = a_{0,\alpha} + a_{1,\alpha}T + a_{2,\alpha}T^2 + a_{3,\alpha}T^3 + a_{4,\alpha}T^4$$

where, T is the reservoir temperature. These coefficients for the various intra-aqueous reactions are summarized in Table 2.5 and Table 2.6.

The mineral equilibrium reactions are typically slower than intra-aqueous reaction and these are modeled as rate-dependent reactions based on their distance from the equilibrium (Nghiem, 2002). Eqn. 2.4 shows the formulation for the rate-dependent reaction.

$$r_\beta = \hat{A}_\beta k_\beta \left[1 - \left(\frac{Q_\beta}{K_{eq,\beta}} \right) \right] \quad (2.4)$$

Here, \hat{A}_β is reactive surface area of mineral reaction β per unit bulk volume of porous medium, k_β is the rate constant of the mineral reaction, Q_β is the activity product of mineral dissolution/precipitation reaction, $K_{eq,\beta}$ is the chemical equilibrium constant of mineral dissolution/precipitation reaction. The parameters used for the mineral reactions in the study are given in Table 2.7.

One important consequence of the precipitation/dissolution reactions is the potential changes in reservoir properties, specifically porosity and permeability. Because ultimate goal here is to examine the viability of seismic monitoring of CO₂ sequestration, changes in reservoir properties, specifically porosity changes will impact seismic response. In GEM, the changes in porosity are modeled based on the changes in reactive surface area as in Eqn. 2.5 below (Nghiem, 2002; 2003).

$$\frac{d\phi}{dt} = -\sum_{k=1}^{n_m} \hat{N}_k \cdot (4\pi\hat{r}_k^2) \frac{dr_k}{dt} \quad (2.5)$$

where ϕ is the porosity, \hat{r}_k is the mean grain size of the mineral, \hat{N}_k is the number of mineral grains per unit volume of rock and r_k is the rate of dissolution of mineral k .

Table 2.7: Rate dependent mineral reaction

Mineral	k_β [mol/(m ² s)] at 25°C	\hat{A}_β [m ² /m ³]
Calcite	-8.79588	88
Kaolinite	-13.0	17600
Anorthite	-12.0	88

2.3. Models for Time-lapse Seismic Monitoring of CO₂ Sequestration

Seismic data have the potential to provide valuable insights into the success or failure of a CO₂ sequestration project. Previous experiments show the feasibility of detecting the motion of CO₂ in the subsurface (Harris *et. al.*, 1995; Nolen-Hoeksema *et. al.*, 1995), which will be very important for ensuring that leakage from the storage site is not taking place. However, the feasibility of long term storage is a more complex issue, because most studies are based on short term field efforts where chemical processes are likely of minimal importance. In this study, conventional models are used, combined with the fluid flow and geochemical simulations, to demonstrate the potential of seismic data to monitor changes in a sequestration site over periods as long as hundreds of years.

This simulation requires models for the changes in seismic properties that are caused by changes in fluid properties and chemical effects. The models used to predict changes in seismic velocity and formation density caused by changes in fluid properties and that in formation properties are summarized here. These provide the essential parameters for simulating the seismic response of the reservoir. This response could be determined using a full simulation of seismic wave propagation, generating synthetic seismograms that would be processed for interpretation applications. Applying amplitude variation with offset (AVO) processing, which is based on measurements of the change in seismic reflection amplitudes with angle of incidence, which is equivalent to changes in the offset between source and receiver in a common midpoint gather, is the primary

interest. Conventional processing fits a line to the amplitude measured as a function of the squared sine of the angle of incidence, reducing a large number of observations to a pair of seismic attributes, the intercept and slope, or gradient, of the line. Simple analytic solutions are available to compute these two attributes for a homogeneous reservoir, and they provide a much faster solution than trying to directly simulate the seismograms and process them for the equivalent results. The basic features of the solutions as well as the models for rock and reservoir properties are outlined here as well as in Kumar *et. al.* (2008).

2.3.1 Seismic Rock Properties

The amplitude of seismic waves reflecting from a formation containing CO₂ or another fluid will depend on the properties of both the fluid itself and of the porous rock matrix. Specifically, seismic compressional and shear wave velocities will change as fluid properties vary, and a common model describing these variations is the Gassmann equation (Gassmann, 1951). This solution assumes isostress conditions for an isotropic, homogenous, monominerallic rock at the low frequency limit. While the shear modulus μ of the rock is predicted to remain constant by this theory, the bulk modulus of the saturated rock depends on several properties of the fluid and solid components as hown in Eqn. 2.6.

$$K_{sat} = K_{dry} + \frac{(1 - K_{dry})^2}{\phi \left(\frac{1}{K_f} - \frac{1}{K_s} \right) + \frac{1}{K_s} \left(1 - \frac{K_{dry}}{K_s} \right)} \quad (2.6)$$

Here K_{dry} is the bulk modulus of the rock sample when dry, K_s is the bulk modulus of the mineral comprising the rock grains, K_f is the fluid bulk modulus, and ϕ is the porosity.

In most cases, the formation will be partially saturated with brine, oil and another fluid such as CO₂. All three fluids are present in the cases studied, and Eqn. 2.7 shows the Wood's equation which gives the bulk modulus of the mixture (Mavko *et. al.*, 2003).

$$\frac{1}{K_f} = \frac{S_{oil}}{K_{oil}} + \frac{S_{CO_2}}{K_{CO_2}} + \frac{S_{brine}}{K_{brine}}, \quad (2.7)$$

where K_i is the bulk modulus of fluid i , and S_i is the saturation of that fluid. The bulk density of the formation (ρ_{bulk}), as shown in Eqn. 2.8, is simply the volume average of the density of each component present in the fluid-saturated rock:

$$\rho_{bulk} = (1 - \phi)\rho_{solid} + \phi(\rho_{oil}S_{oil} + \rho_{CO_2}S_{CO_2} + \rho_{brine}S_{brine}) \quad (2.8)$$

These results provide simple estimates of the properties of the reservoir fluid and the density.

Given these models for bulk and shear moduli, and density of the CO₂ bearing formation, Eqn. 2.9 gives the P- and S-wave velocities.

$$V_p = \sqrt{\frac{K_{sat} + \frac{4}{3}\mu}{\rho_{bulk}}} \quad \text{and,} \quad V_s = \sqrt{\frac{\mu}{\rho_{bulk}}} \quad (2.9)$$

where μ is the shear modulus. The S-wave velocity is comparatively weakly dependent on the fluid properties, because only density changes affect it. However, the change in the P-wave velocity is more significant because of its dependence on the bulk modulus.

In a general case, seismic properties will change with pore pressure as well. However, in our simulations the changes in pore pressure are comparatively small, on the order of several MPa, especially after CO₂ injection stops. Test calculations show that pressure effects cause much smaller changes in seismic velocity than saturation and other effects, so those are ignored in this study.

2.3.2 Acoustic Properties of Reservoir Fluids

While the Gassmann and Wood's equations provide models for changes in seismic properties with changes in fluid saturations, integration of seismic and fluid flow simulations also requires relationships to quantify the effects of changing temperature, salinity and pore pressure. The density of brine, which depends upon salinity, pore-pressure and temperature, was taken directly from the simulation results, but the P-wave velocity changes for the relevant fluids require additional models. The models used for the fluids of interest, viz. brine, oil and supercritical fluid CO₂ are summarized next:

Brine. Batzle and Wang (1992) provide empirical relationships for changes in brine P-wave velocity as shown in Eqn. 2.10:

$$V_p = V_w + S(1170 - 9.6T + 0.055T^2 - 8.5 \times 10^{-5}T^3 + 2.6P - 0.0029TP - 0.0476P^2) + S^{1.5}(780 - 10P + 0.16P^2) - 1820S^2 \quad (2.10)$$

Here pressure P is in MPa, temperature T is in degree Celsius, salinity S is in parts per million divided by 10^6 . The acoustic velocity in pure water, V_w , in m/s is

$$V_w = \sum_{i=0}^4 \sum_{j=0}^3 w_{ij} T^i P^j ,$$

and the coefficients w_{ij} are as provided by Batzle and Wang (1992). The acoustic velocity and density can be used to determine the bulk moduli of brine using

$$V_p^2 = K / \rho$$

Oil. The acoustic velocity in dead oil, oil with minimal gas present, depends upon pore-pressure and temperature and is shown in Eqn. 2.11 (Batzle and Wang, 1992).

$$V_p (m/s) = 2096 \left(\frac{\rho_r}{2.6 - \rho_r} \right)^{1/2} - 3.7T + 4.64P + 0.0115[4.12(1.08\rho_r^{-1} - 1)^{1/2} - 1]TP \quad (2.11)$$

Here ρ_r is reference standard density. The density of dead oil is directly taken from simulation results.

Supercritical Carbon dioxide (SCF CO₂). The CO₂ phase diagram shows a critical temperature of 31°C and a critical pressure of 7.38 MPa. Below this temperature and /or pressure, CO₂ exists either in liquid or vapor phase. Above critical temperatures and pressures, the pure CO₂ exists in supercritical state. Supercritical CO₂ still behaves like a gas occupying all the available volume but has a liquid density that increases from 200 kg/m³ to values on the order of 900 kg/m³, depending upon pressure and temperature conditions. The density of supercritical CO₂ is directly obtained from simulation results, while the bulk modulus of supercritical CO₂ can be calculated using Eqn. 2.12 (Vargaftik, 1975).

$$K_{CO_2} = 4.2911 \times 10^{-2} - 8.3309 \times 10^{-3} P + 5.8377 \times 10^{-4} P^2 - 4.3896 \times 10^{-4} P^3 \quad (2.12)$$

2.3.3 Calculation of Seismic AVO Attributes

The amplitude of a seismic reflection from a boundary between two materials is approximately a linear function of the squared sine of the angle of incidence i (Shuey, 1985):

$$R(i) \approx R(0) + G \sin^2 i$$

Appropriately processed prestack seismic data, when sorted into common reflection point, or common midpoint, gathers, provide a measure of this reflection coefficient. Typical *amplitude variation with offset* (AVO) analysis fits a line to these measured reflection amplitudes to estimate the intercept $R(0)$ and gradient G . The intercept is

equal to the normal incidence reflection coefficient and can be considered an estimate of the seismic amplitude that would be observed in a typical seismic section. The values of these two parameters generated by hydrocarbon or CO₂ bearing formations are often significantly different from those of brine-saturated rock, providing a valuable tool for detecting fluids of interest.

However, the reservoir, with thickness $b=20$ m, is sufficiently thin that reflections from the top and bottom of the layer will interfere for seismic frequencies typical of surface seismic data (about 30 Hz) and so the Shuey (1985) result cannot be utilized directly. Lin and Phair (1993) showed that composite reflection associated with this superposition or “tuning” still has the same general functional form, but the intercept and gradient of the line take the form:

$$R_t(0) = \frac{4\pi b f R(0)}{V_g} \quad \text{and} \quad G_t = \frac{4\pi b f}{V_g} \left(G - \frac{R(0)}{2} \right) \quad (2.13)$$

In the Eqn. 2.13 above, f is frequency, V_g is the interval velocity in the reservoir formation, and $R(0)$ and G are the conventional AVO intercept and gradient respectively for the upper interface of the reservoir. By using “tuned” AVO solution, results could be achieved faster as compared to a simulation of the synthetic seismograms followed by processing.

2.4.Results and Discussion

In this section the results from the modeling of reactive transport associated with CO₂ injection and the impact on the seismic response as the CO₂ front propagates in the reservoir are discussed. The primary objective is to examine the feasibility of seismic monitoring of CO₂ movement under the specific conditions studied here. Two different cases of CO₂ injection into a five spot pattern are considered. For CASE1, the properties correspond to a ‘vuggy’ carbonate reservoir whereas for CASE2, the properties are representative of a ‘marly’ limestone. Mean properties of the carbonates were taken from measurements presented by Brown (2002). The results from the fluid flow and seismic modeling are discussed below.

2.4.1 CASE 1: Small Spatial Correlation of Permeability

The permeability distribution for this case has a low spatial correlation with a minimum of 0.1 md and a maximum of 2200 md. CO₂ is injected for 6 years and then all the wells are shut-in. The reservoir conditions are then monitored at 10 years, 100 years and 1000 years. Figure 2.4 shows the gas and oil saturation in the reservoir at the end of 6 years. The gas phase is primarily supercritical CO₂. In addition, pressure and the dissolution of CO₂ in brine are shown in Figure 2.5. As time progresses, the reservoir pressure equilibrates to a near constant value of 22.72 MPa at the end of 1000 years. The decrease in pressure is mainly due to the formation of bicarbonate ions from the mixing

of CO₂ and brine. This reduces the amount of gas present in the reservoir, and in turn reduces the pressure. The mixing of CO₂ into the reservoir brine will change the brine density and pH due to chemical interactions. The distribution of salinity and brine densities are shown in Figure 2.6. Brine salinity change (calculated as TDS) of 10% is noticed after 6 years of injection, and this in turn changes the density of the brine. As the gas-aqueous system comes into equilibrium, the salinity changes become very slow at later times. This can be attributed to fact that fast aqueous reactions are predominant only during the first few years while gas is being injected, and after that only slow mineral reactions shift the equilibrium.

The oil density also changes because of mixing with CO₂. Whereas the brine density increases because of CO₂ dissolution, the effect on the oil density will be opposite as shown in Figure 2.7a, and the corresponding gas density distribution is shown in Figure 2.7b. CO₂ injection and associated geochemical reactions lead to precipitation of Calcite and Kaolinite, and dissolution of Anorthite. Figure 2.8 through Figure 2.10 show the mineral precipitation/dissolution profiles for Calcite, Kaolinite, and Anorthite respectively at 100 and 1000 years. Positive values indicate mineral precipitation, while negative values indicate dissolution. For example, with time both Calcite and Kaolinite precipitate whereas Anorthite dissolves. Porosity changes due to these mineral reactions are of order of 0.15%, and 1.5% are observed at times 100 years, and 1000 years respectively.

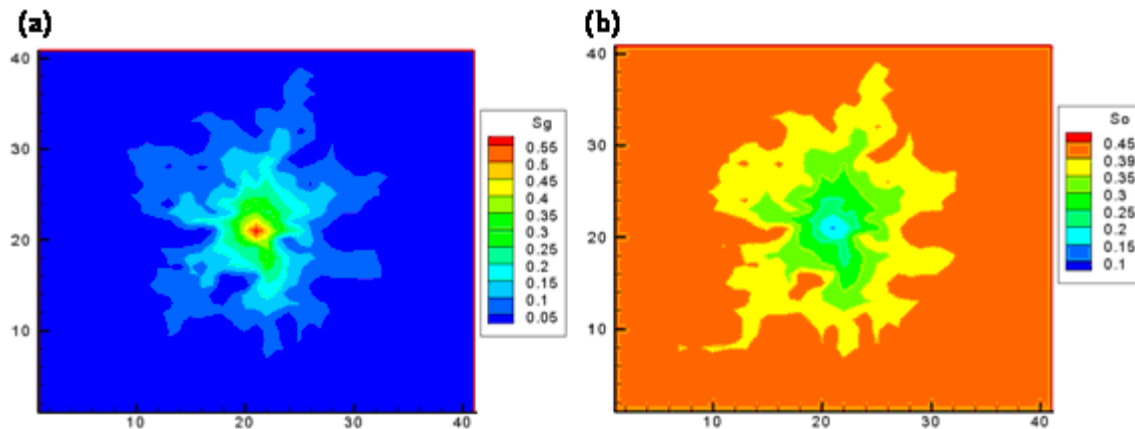


Figure 2.4: (a) Gas saturation, and (b) oil saturation at 6 years (end of gas injection) for heterogeneous field with small correlation length

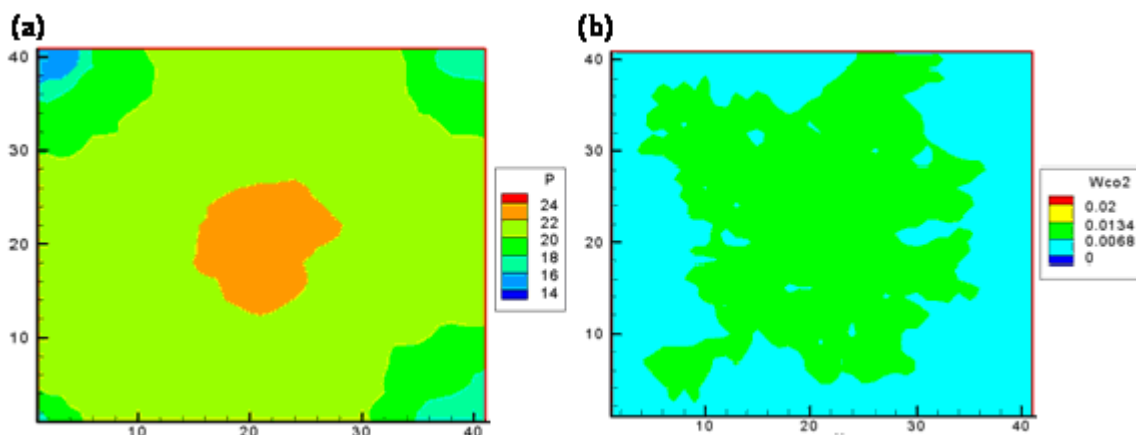


Figure 2.5: (a) Pressure, and (b) CO2 concentration in brine at 6 years (end of gas injection) for heterogeneous field with small correlation length

Changes in seismic properties computed using the Gassmann equation including changes in densities, are measurable. For this model, the reservoir is assumed to be located at a depth of 2 Km, overlain by an isotropic and homogenous medium of $V_p = 4.5$ Km/s, $V_s = 2.5$ Km/s and density = 2.2 g/cc. Figure 2.11 shows the changes P-wave velocity, V_p , at $t = 6, 10, 100$ and 1000 years. These changes are computed with

respect to the initial conditions at $t = 0$. Because of CO_2 injection and the mineral precipitation/ dissolution with accompanying porosity changes, the velocity decreases by 2.73%, 2.75%, 2.765% and 2.87% at $t = 6, 10, 100$ and 1000 years respectively. The AVO intercept and gradient parameters provide important insights into the seismic detectability of the CO_2 front. The intercept parameter, $R(0)$, which undergoes a decrease of 13.63%, 14.14%, 13.85% and 11.6% at the monitoring times, $t = 6, 10, 100$ and 1000 years, and the corresponding changes in gradient are 5.02%, 5.07%, 5.09% and 5.45% respectively (Figure 2.12). Not surprisingly, most of the change takes place during the six years of CO_2 injection, but it is important to note that the reservoir continues to undergo changes that affect seismic amplitudes. In particular, the changes in the intercept show that seismic data will undergo changes in amplitude that are related to chemical processes, not fluid movements as system attains pressure equilibrium soon after end of injection. Figure 2.13 shows the variation of reflection coefficient with variation in angle of incidence at different times. Upon CO_2 injection, reflection coefficient value decreases by 15% at angle of incidence value of zero. This is mainly because of corresponding decrease in the intercept term. Decrease from initial value for reflection coefficient remains nearly same as the angle of incidence increases. This is because gradient term decreases only by 5% upon CO_2 injection.

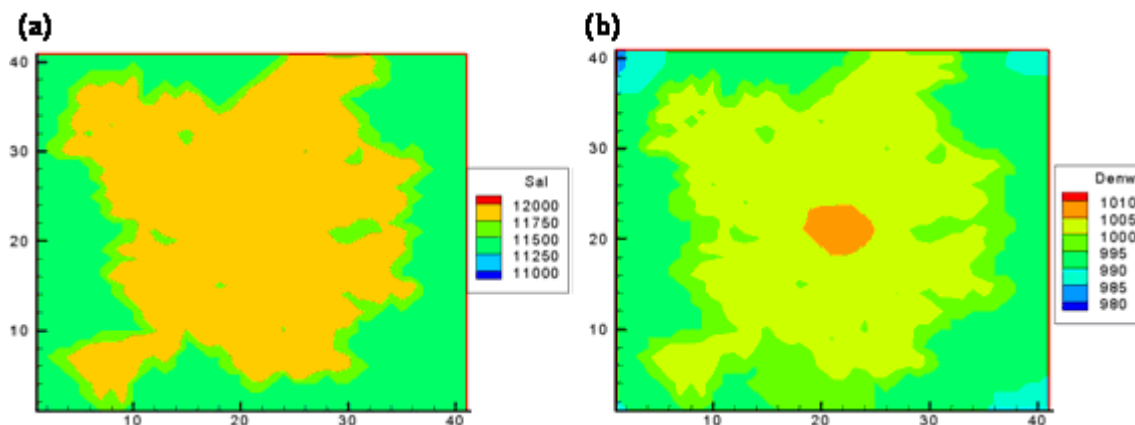


Figure 2.6: (a) Salinity (in ppm) and (b) brine density (in kg/m^3) at 6 years (end of gas injection) for heterogeneous field with small correlation length

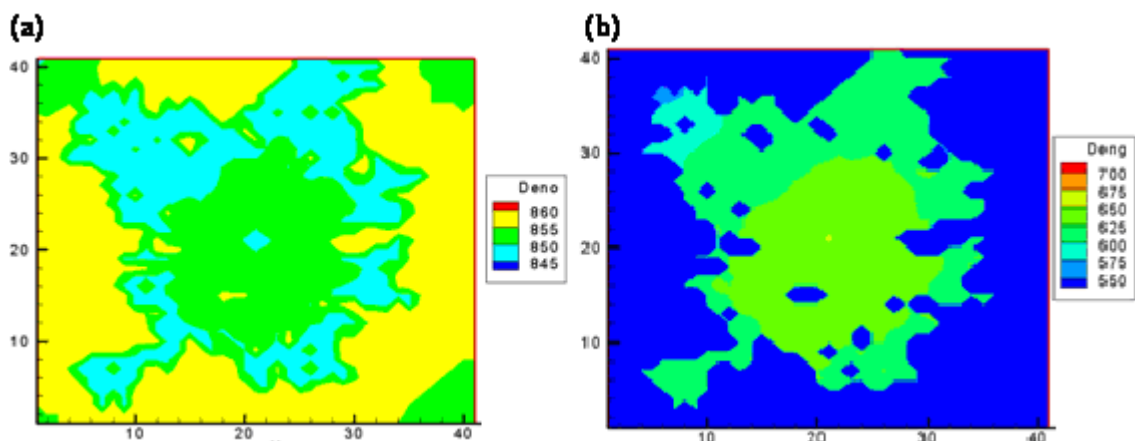


Figure 2.7: (a) Oil density (in kg/m^3), and (b) gas density (in kg/m^3) at 6 years (end of gas injection) for heterogeneous field with small correlation length

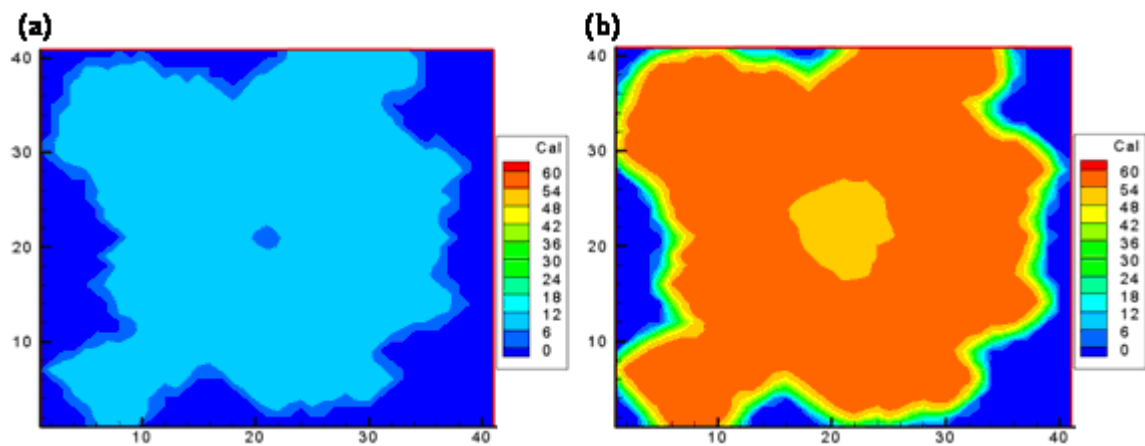


Figure 2.8: Moles of Calcite precipitated at (a)100 years, and (b) 1000 years

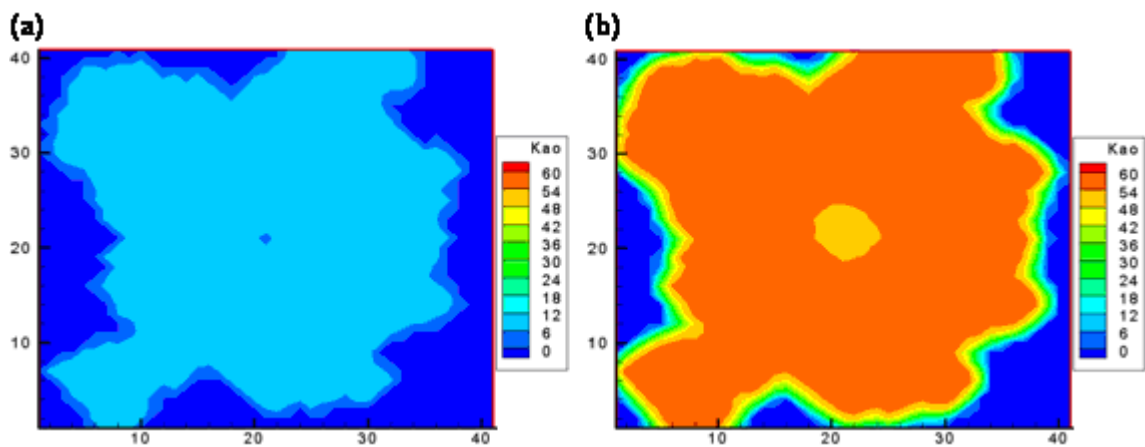


Figure 2.9: Moles of Kaolinite precipitated at (a)100 years, and (b) 1000 years

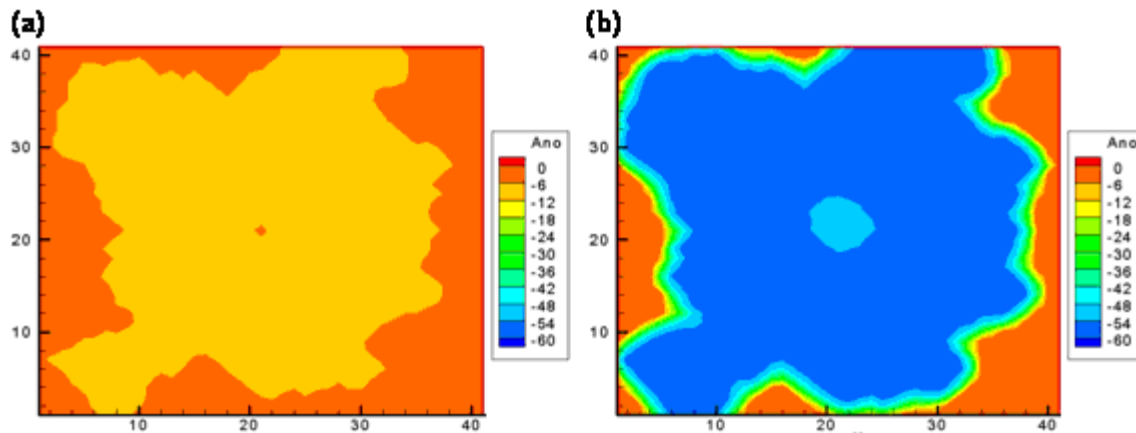


Figure 2.10: Moles of Anorthite precipitated at (a)100 years, and (b) 1000 years

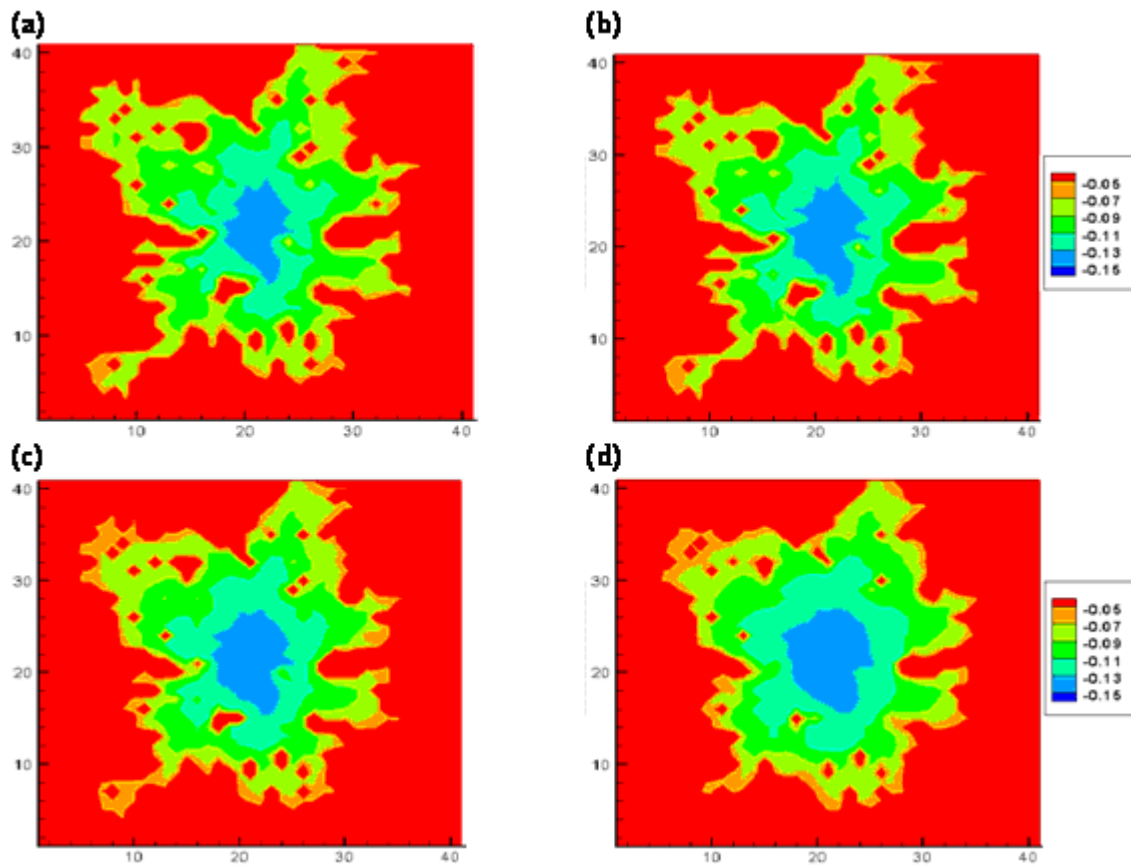


Figure 2.11: (a), (b), (c) and (d) represents difference of V_p (in km/s) between $t= 6, 10, 100$ and 1000 years respectively with $t=0$ years for weakly correlated heterogeneous model

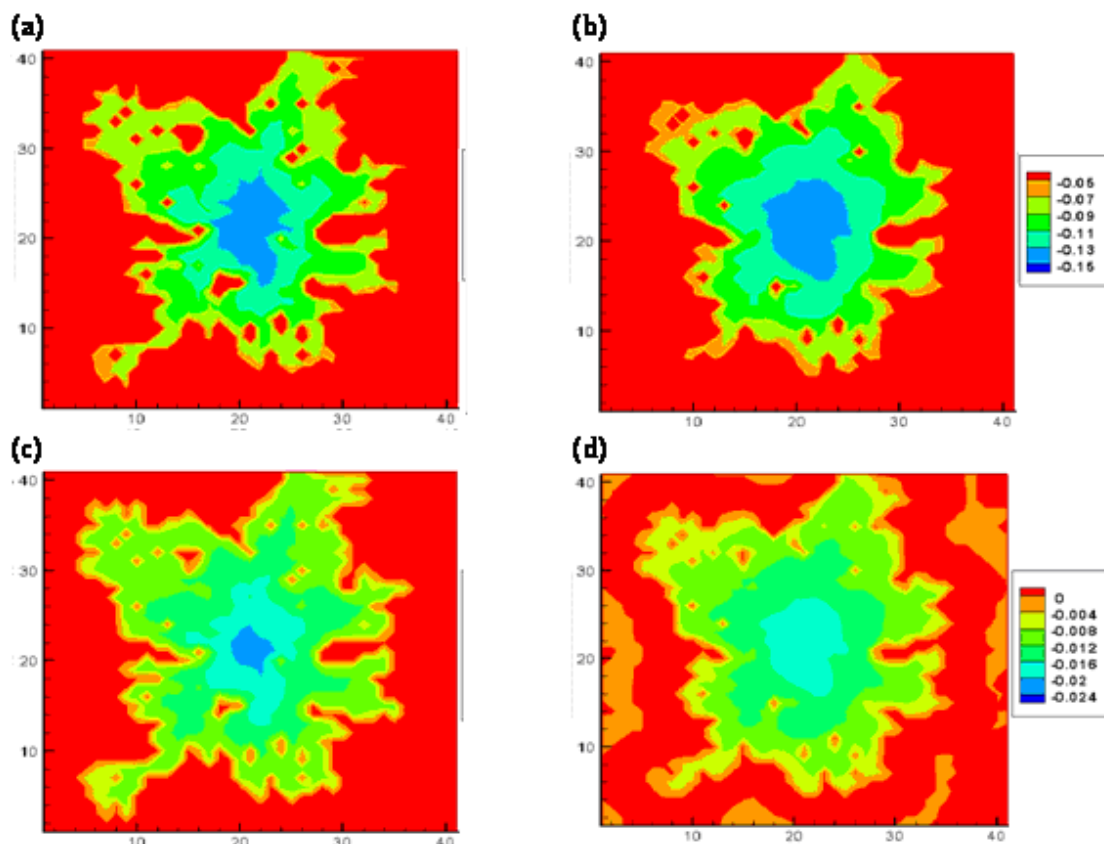


Figure 2.12: (a) and (b) represent difference of intercept between $t=10$ and 1000 years respectively with $t=0$ years for weakly correlated heterogeneous model. (c) and (d) represent same profiles for gradient

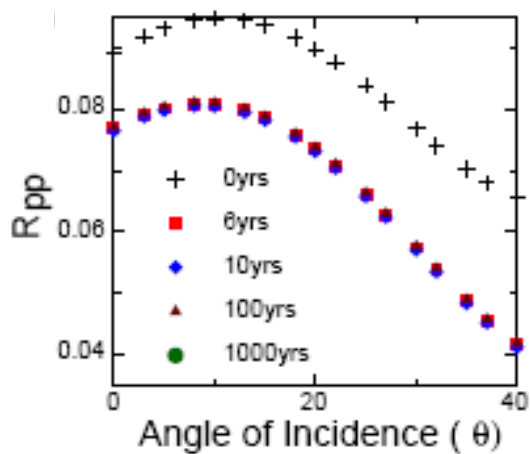


Figure 2.13: Variation of reflection coefficient values with time and angle of incidence for weakly correlated heterogeneous model

2.4.2 CASE 2: Large Spatial Correlation of Permeability

The permeability distribution in this example shows strong anisotropy and long range spatial correlation as shown in Figure 2.2a. The gas phase saturation and gas density at the end of 6 years of CO₂ injection are shown in Figure 2.14. The effects of the permeability anisotropy and large spatial correlation are quite apparent from the preferential south-east movement of the CO₂ front. The reservoir pressure distribution and brine densities are shown in Figure 2.15.

For seismic modeling, the reservoir is assumed to be overlain by an isotropic and homogenous medium having $V_p = 3.55$ Km/s, $V_s = 2.8$ Km/s and density = 1.6 g/cc. Figure 2.16 shows the change in v_p at $t = 6, 10, 100$ and 1000 years with respect to the v_p at time $t=0$. As for CASE 1, the changes in P-wave velocity appear to closely follow the CO₂ saturation distribution. The same features can also be seen in the AVO parameters. For example, Figure 2.17 shows change in the intercept and the gradient at $t = 10$ and 1000 years respectively with respect to $t = 0$ years.

To better infer the causes of the changes in seismic attributes, we tested the effects of including the geochemical reactions on the viability of seismic monitoring of CO₂ sequestration. The driving force of the geochemical reactions is the acidification of the brine from CO₂ dissolution. A case where the brine is made chemically inert and thus, no intra-aqueous or mineral reactions take place is examined next. The changes in AVO attributes (intercept and gradient) after 10 years for this case are shown in Figure 2.18.

Figure 2.19 shows variation in reflection coefficient with variation in angle of incidence at different times. Upon CO₂ injection, reflection coefficient value decreases by 15% at angle of incidence value of zero as in previous case. But decrease from initial value for reflection coefficient increases as the angle of incidence increases for this case. This is because gradient term for this case decreases by 13% upon CO₂ injection. This difference in seismic behavior as compared to previous case is mainly because of difference in overburden properties for the two cases. For comparison purposes, in Figure 2.20 we show the fractional changes in the intercept and gradient parameters with and without including the chemical reactions. Increased changes from 2-10% are seen in the intercept and gradient when the CO₂ solubility in brine and resulting geochemical reactions are taken into account. It is important that the largest changes take place at the boundaries of the portion of the reservoir with significant CO₂ saturation. This implies that seismic data have strong potential to help in defining this region, which can be very important for detecting suspected leaks in the sequestration site.

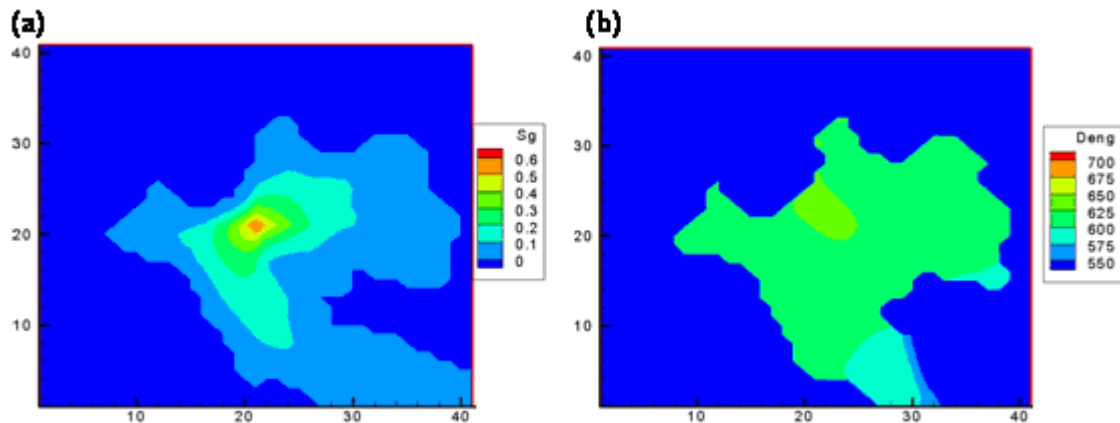


Figure 2.14: (a) Gas saturation, and (b) gas density (in kg/m³) at 6 years (end of gas injection) for heterogeneous field with large correlation length

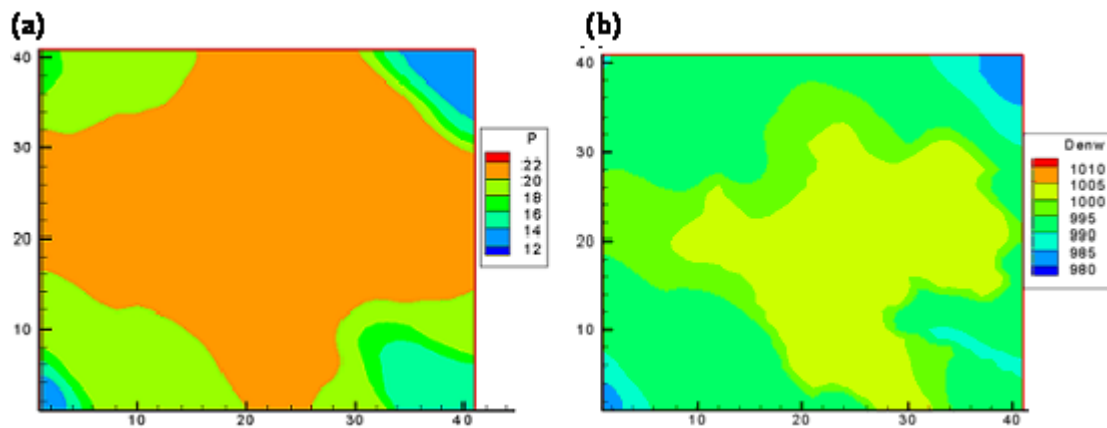


Figure 2.15: (a) Pressure (in MPa) profile, and (b) brine density (in kg/m³) at 6 years (end of gas injection) for heterogeneous field with large correlation length

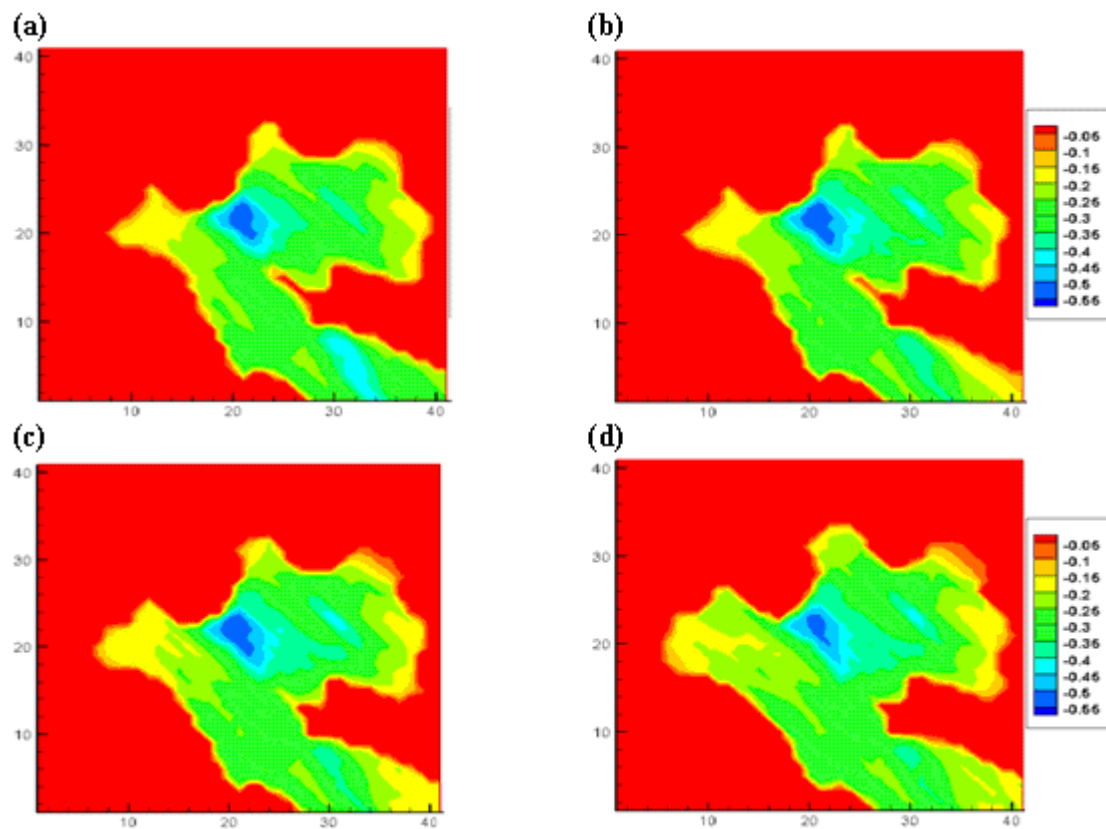


Figure 2.16: (a), (b), (c) and (d) represents difference of V_p (in km/s) between $t= 6, 10, 100$ and 1000 years respectively with $t=0$ years for heterogeneous field with large correlation length

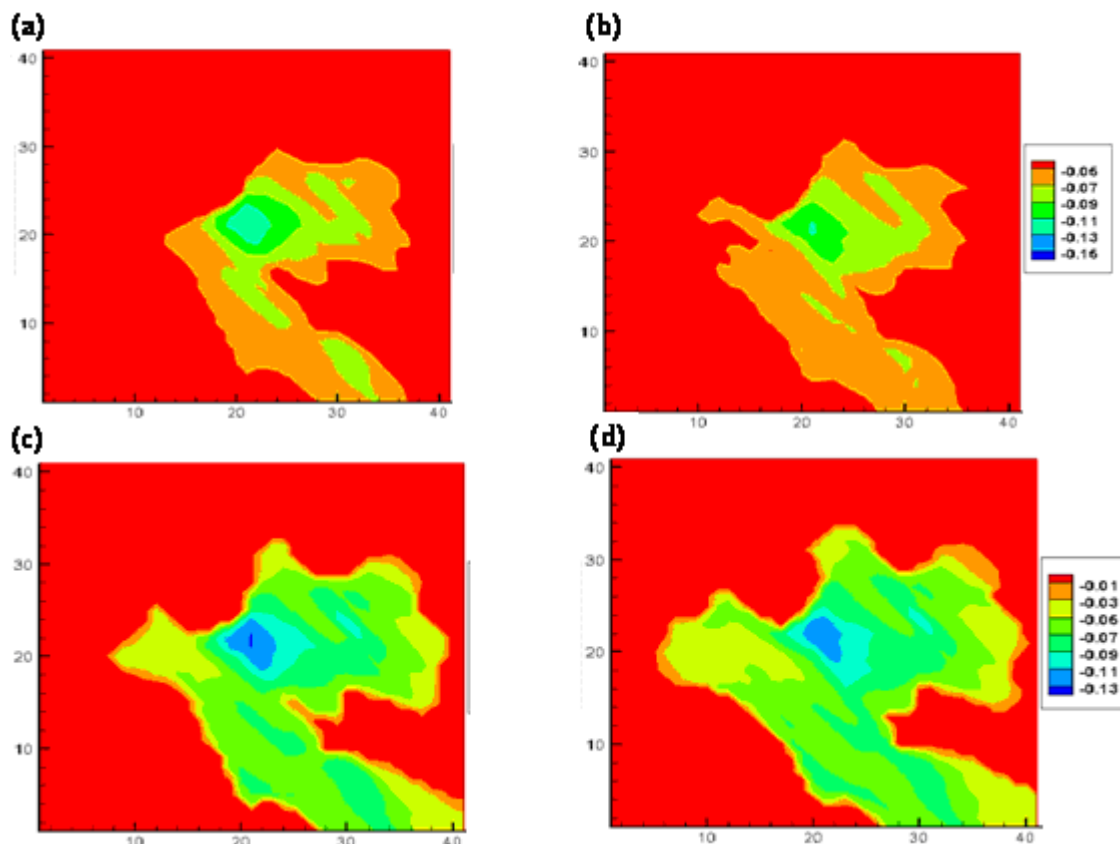


Figure 2.17: (a) and (b) represent difference of intercept between $t=10$ and 1000 years respectively with $t=0$ years for heterogeneous field with large correlation length. (c) and (d) represent same profiles for gradient

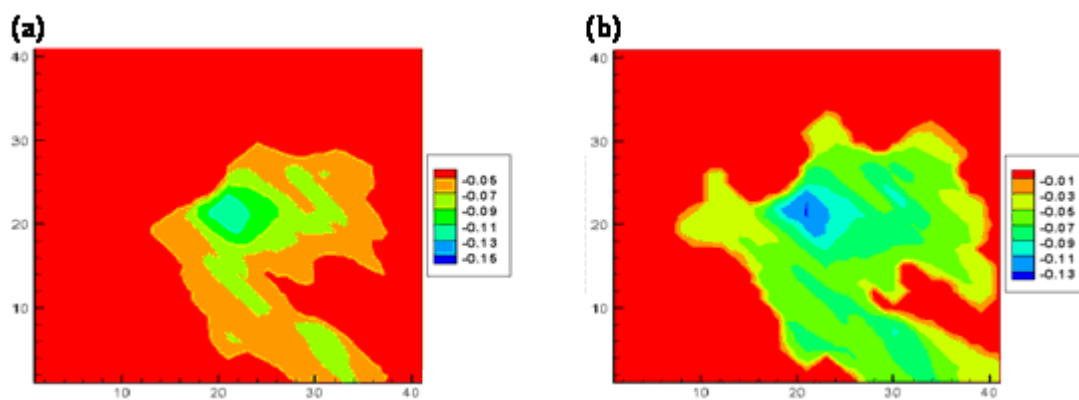


Figure 2.18: (a) and (b) represents difference of intercept and gradient at 10 years respectively with $t=0$ years for case with no chemical reaction

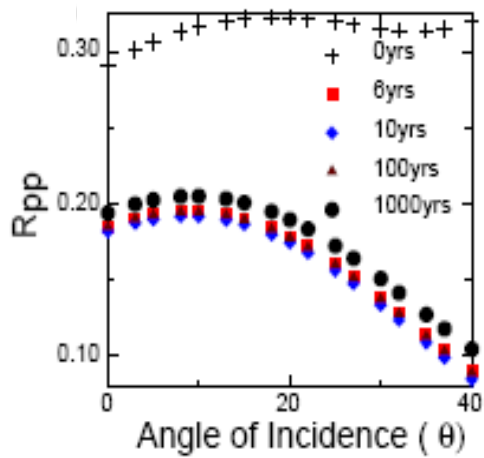


Figure 2.19: Variation of reflection coefficient values with time and angle of incidence for heterogeneous field with large correlation length

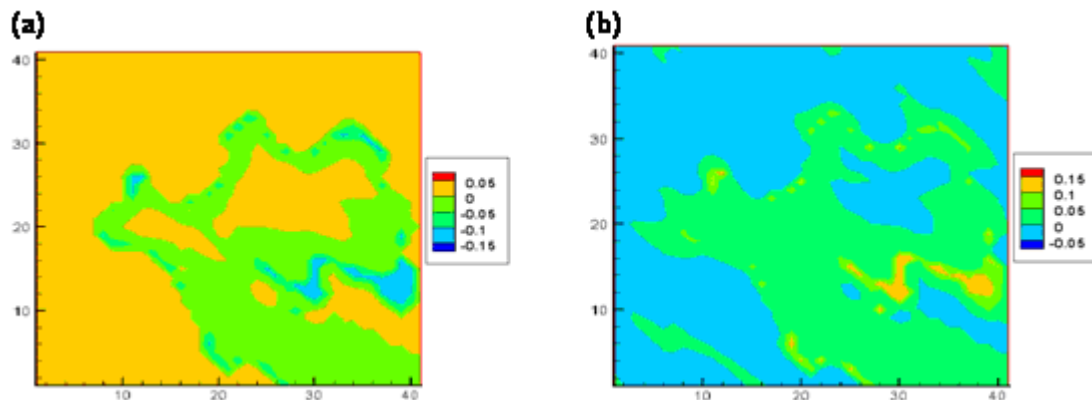


Figure 2.20: Fractional changes in (a) intercept, and (b) gradient due to chemical activities of brine at 10 years for heterogeneous field with large correlation length

CHAPTER III

LARGE-SCALE DATA ASSIMILATION USING ENSEMBLE KALMAN FILTER

3.1.Introduction

Geologic models are built based on static data only typically do not reproduce the dynamic response of the reservoir such as pressure, water-cut & GOR. The goal of is to update the geologic models in such a way that the simulated field response matches the observed field response, while preserving geologic realism. Various methods have been proposed in the literature for accomplishing this task, including the Ensemble Kalman filter algorithm (Deng *et. al.*, 2006; Arroyo *et. al.*, 2006). Ensemble Kalman Filters (EnKF) have gained increasing interest for history matching and continuous reservoir model updating. It is a Monte-Carlo approach that works with an ensemble of reservoir models. Because the model adjustments by EnKF are within the space spanned by the ensemble members, the optimal ensemble member selection plays a critical role in the performance of the EnKF.

Some critical issues related to history matching a large field with substantial production history are explored in this chapter, specifically with regard to history matching using EnKF. These include optimal initial member selection while maintaining the required spread in their dynamic response, covariance localization to remove spurious

covariance calculations, and preserving geologic realism during history matching. A novel and efficient member selection approach is proposed which uses spectral clustering to select ‘optimal’ initial ensemble members using their dynamic response in terms of sweep efficiency computed from the streamline time-of-flight. Also, well-specific black-oil or compositional streamline trajectories that are generated from the velocity field, computed during flow simulation with little additional expense, are used for covariance localization.

The approach is first validated using a two-dimensional synthetic example. Next it is applied to the Weyburn field, a large carbonate reservoir in Canada, for history matching the production response from both the water and CO₂ injection phase using a finite-difference compositional simulator.

3.2.Data Assimilation Methodology

Different approaches of data assimilation for hydrocarbon reservoirs have been proposed in the literature. The key idea behind these studies is to update the initial geologic models of a hydrocarbon reservoir using the actual flow-related observations from the field. Initial geologic models are prepared using the static information such as log, core, and 3-D seismic data. Once dynamic data such as production and 4-D seismic become available, the initial models are updated such that the numerically simulated results using updated reservoir models honor the observed dynamic data.

3.2.1 Bayesian Inference and Data Assimilation

From a Bayesian perspective, observables and parameters of a statistical model are treated alike and are considered random quantities. Let Y be the observed data and X the model parameters. The inference requires calculating joint probability distribution $P(Y, X)$ over all random quantities as shown in Eqn. 3.1.

$$P(Y, X) = P(Y | X)P(X) \quad (3.1)$$

where $P(X)$ is the prior distribution, and $P(Y | X)$ is the likelihood. Once data Y is observed, Bayes theorem may be used to determine the distribution of X conditional on Y (Eqn. 3.2)

$$P(X | Y) = \frac{P(X)P(Y | X)}{\int P(X)P(Y | X)dx} \quad (3.2)$$

where $P(X | Y)$ is called the posterior distribution of X .

Also, for a system defined by the ordinary differential equation (Eqn. 3.3):

$$\frac{dx}{dt} = F(t, x) \quad (3.3)$$

the maximum likelihood estimate for the trajectory that best fits the observations may be formulated as shown in Hunt *et. al.* (2007). The likelihood of a trajectory $x(t)$, as shown in Eqn. 3.4, is proportional to

$$\exp\left(-\frac{1}{2} \left[y_j^o - H_j(x(t_j)) \right]^T R_j^{-1} \left[y_j^o - H_j(x(t_j)) \right] \right) \quad (3.4)$$

Here at any time t_j , y_j^o is a vector of observed values, H_j defines the relationship between y_j^o and $x(t_j)$:

$$y_j^o = H_j(x(t_j)) + \varepsilon_j$$

where ε_j is a zero-mean Gaussian random variable with covariance matrix R_j . Then, the most likely trajectory is the one that minimizes the cost function J^o in Eqn. 3.5.

$$J^o = [y_j^o - H_j(x(t_j))]^T R_j^{-1} [y_j^o - H_j(x(t_j))] \quad (3.5)$$

3.2.2 Nonlinear Systems under White Noise Excitation

A non-linear system under external and/or parameter type excitation, as shown in Paola and Sofi (2002), is discussed here to set-up the background for the optimal solution.

Let's start with Eqn. 3.6, which is the stochastic differential equation in Stratonovich form:

$$\dot{X} = f(X, t) + g(X, t)W(t) \quad (3.6)$$

where \dot{X} denotes time derivative, $f(X, t)$ and $g(X, t)$ are arbitrary nonlinear functions for the response process $X(t)$ and time t , and $W(t)$ denotes zero-mean white noise characterized by:

$$E(W(t_1)W(t_2)) = q\delta(t_1 - t_2)$$

where $E[\cdot]$ indicates stochastic average, $\delta[\cdot]$ is Dirac's delta function, and q denotes the strength of the white noise.

It may be converted into the $It\hat{o}$ type equation as shown in Eqn. 3.7:

$$dX = m(X, t)dt + g(X, t)dB(t) \quad (3.7)$$

where $B(t)$ is the Wiener process such that $W(t) = dB/dt$. $m(X, t)$ is called the drift coefficient and is related to $f(X, t)$ and $g(X, t)$ as shown in Eqn. 3.8:

$$m(X, t) = f(X, t) + \frac{1}{2}qg(X, t)\frac{\partial g(X, t)}{\partial X} \quad (3.8)$$

3.2.3 Nonlinear Filtering Using Fokker-Planck-Kolmogorov Probability Density Evolutions

For a continuous time state and discrete time observations, the state probability density function may be propagated by solving the Fokker-Planck-Kolmogorov equation (FPKE). Let's consider Eqn. 3.9 which is the $It\hat{o}$ stochastic system as discussed in the previous section:

$$\dot{X}_t = f(X_t, t) + g(X_t, t)W(t) \quad t \geq t_o \quad (3.9)$$

Also, observations Y_{t_k} for the system at discrete times t_k are taken as:

$$Y_{t_k} = H(X_{t_k}, t_k) + v_{t_k}, \quad k = 1, 2, \dots$$

where $H(X_{t_k}, t_k)$ is a linear/nonlinear function of the states of the system and v_{t_k} is a white Gaussian noise with covariance matrix R_{t_k} . If the prior density exists, and is once continuously differentiable with respect to t and twice continuously differentiable

with respect to X_t , then the conditional density $P(X, t | Y^{t_{k-1}})$ satisfies the FPKE between observations (Challa and Bar-shalom, 2000; Jazwinski, 1970), i.e.,

$$\frac{\partial P}{\partial t} = -\sum_{i=1}^n \frac{\partial [Pf(X_t, t)_i]}{\partial x_i} + \frac{1}{2} \sum_{i=1}^n \sum_{j=1}^n \frac{\partial [P(g(X_t, t)q_i g(X_t, t)^T)_{ij}]}{\partial x_i \partial x_j}, \quad t_k > t \geq t_{k-1} \quad (3.10)$$

where $P(X, t | Y^{t_{k-1}})$ was replaced by P in Eqn. 3.10.

Following an observation at t_k , the conditional density satisfies Bayes' formula in Eqn. 3.11.

$$P(X, t_k | Y^{t_k}) = \frac{P(X, t_k | Y^{t_{k-1}})P(Y_{t_k} | X)}{\int P(X, t_k | Y^{t_{k-1}})P(Y_{t_k} | X)dX} \quad (3.11)$$

where, $Y^{t_k} \triangleq \{Y_{t_k}, Y^{t_{k-1}}\}$ and $P(Y_{t_k} | X)$ is given by:

$$P(Y_{t_k} | X) = \frac{1}{|2\pi R_{t_k}|^{1/2}} e^{-1/2[Y_{t_k} - H(X_{t_k})]^T R_{t_k}^{-1}[Y_{t_k} - H(X_{t_k})]}$$

The two equations, Eqns. 3.10 and 3.11, are respectively the predictor and corrector equations of the density evolution method.

3.2.4 Ensemble Kalman Filter (EnKF) for Non-linear System

As discussed in the previous section, Fokker-Planck-Kolmogorov equation propagates the probability distribution of system states during the forecast step. This approach is

computationally intensive for small dimensional system, and not feasible for large dimensional system. So, two practical alternative approaches are Monte Carlo and Kalman filter. The Monte Carlo approach uses a large ensemble of system states to approximate the probability distribution, while Kalman filter assumes Gaussian distributions and tracks their mean and covariance (Hunt *et. al.*, 2007). Ensemble Kalman filter has elements of both the methods. It uses a Gaussian approximation while following the time evolution of the mean and covariance by propagating an ensemble of states. The ensemble is used only to parameterize the distribution and not to sample it thoroughly. It is desired that the ensemble should be large enough to approximately span the space of possible solutions at any assimilation step. EnKF analysis basically determines the linear combination of the ensemble members which forms the best estimate of the current state, given the current observations. Figure 3.1 shows the schematic of the density propagation using EnKF. The density function evolves deterministically, spreads stochastically, and is then reinforced due to observation (Isard and Blake, 1998).

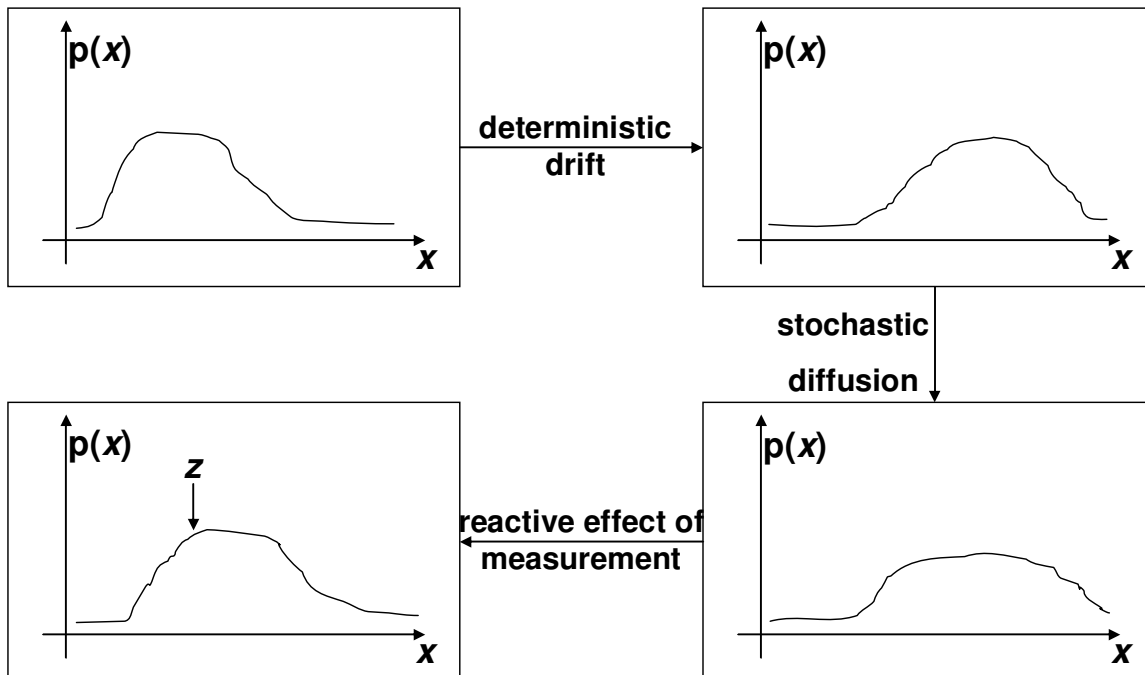


Figure 3.1: Probability density propagation using ensemble Kalman filter (EnKF). The three phases are (i) drift due to component of object dynamics, (ii) diffusion due to the random component, and (iii) reactive reinforcement due to observation

3.2.5 EnKF Formulation

The Ensemble Kalman Filter was proposed by Evensen (1994) and is summarized in Evensen (2003). It is a sequential filter method and starts with an ensemble of initial models. The models are integrated forward in time up to the time when the next set of observations is available, which are then used to update the models before the integration continues. Eqn. 3.12 shows the key EnKF analysis equation.

$$x^a = x^f + P^f H^T (HP^f H^T + R)^{-1} (d - Hx^f) \quad (3.12)$$

with the analysis error covariances as given in Eqn. 3.13.

$$P^a = P^f - P^f H^T (HP^f H^T + R)^{-1} HP^f \quad (3.13)$$

Here, H is the measurement operator relating the true model state x^t to the observations d allowing for measurement errors ε .

$$d = Hx^t + \varepsilon$$

Models are updated using a weighted linear combination of the forecast models, and covariances $P^f H^T$ corresponding to measurements d . The weights are determined by an innovation term, which is the difference between the prediction and the measurements, the error covariances for the model prediction projected onto the measurements $HP^f H^T$, and the measurement error covariances R .

The above analysis equation is often expressed as Kalman gain, K , of Eqn. 3.14.

$$K = P^f H^T (HP^f H^T + R)^{-1} \quad (3.14)$$

The error covariance matrices for the forecast and analyzed estimates, P^f and P^a , are defined in the Kalman filter in terms of true state as:

$$P^f = \overline{(x^f - x^t)(x^f - x^t)^T}$$

$$P^a = \overline{(x^a - x^t)(x^a - x^t)^T}$$

where x is the model state vector, and superscripts f , a , and t represent forecast, analysis, and true state, respectively. However, since the true state is not known, the ensemble mean \bar{x} is used to define the covariances as shown in Eqns. 3.15 and 3.16.

$$P^f \cong P_e^f = \overline{(x^f - \bar{x}^f)(x^f - \bar{x}^f)^T} \quad (3.15)$$

$$P^a \cong P_e^a = \overline{(x^a - \bar{x}^a)(x^a - \bar{x}^a)^T} \quad (3.16)$$

These covariances from an ensemble of finite size provide an approximation to the error covariance matrices. As the size of the ensemble, N , increases, the errors in Monte Carlo sampling will decrease proportional to $1/\sqrt{N}$. Figure 3.2 shows the schematic of EnKF based data assimilation.

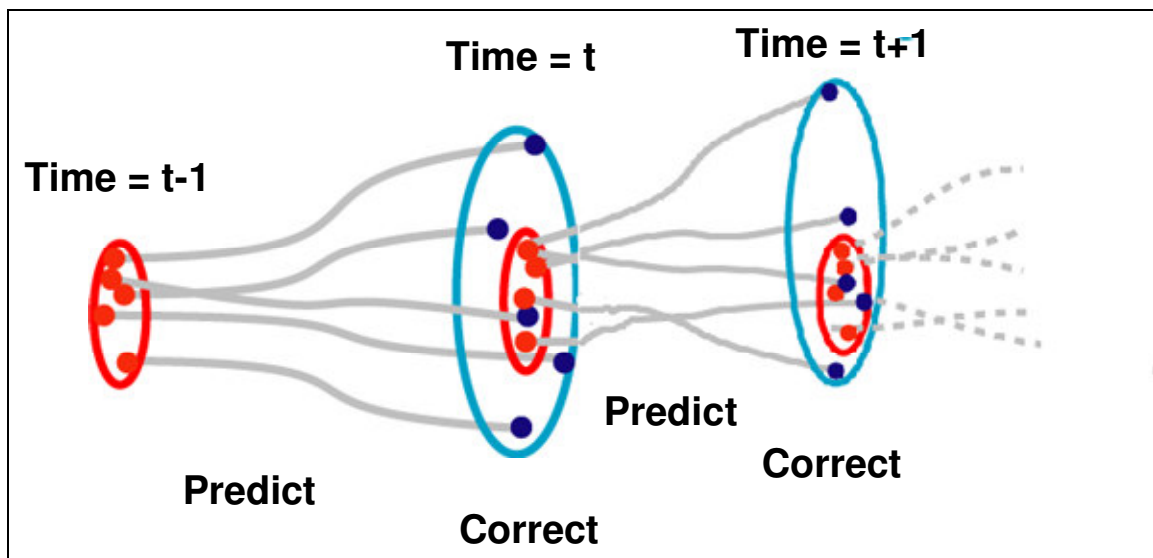


Figure 3.2: Schematic of EnKF based data assimilation

3.2.6 EnKF Enhancements for Field Applications

Covariance Localization and Inflation. As mentioned in the previous section, defining error covariance matrices using an ensemble can lead to an analysis with a biased mean state and insufficient variance. If the background errors are underestimated, then the analysis ignores observations and the posterior resembles the prior. This phenomenon is called filter divergence (Hamill *et. al.*, 2001). Another source of filter divergence is

when the magnitude of background covariances between an observation location and far-off grid is overestimated due to sampling errors, i.e., the posterior for the far-off grid is adjusted too much. This is true when the model under study has a large number of dimensions. Filter divergence causes the analysis to drift away from the true state, and this problem only grows with subsequent assimilation cycles.

Different approaches have been suggested in the literature to mitigate filter divergence. One approach is to localize the covariances using a Schur product with a correlation function (Houtekamer and Mitchell, 2001). This results in the removal of spurious covariances for the far-off cells and thus prevents unrealistically large changes to the model parameters. Different correlation functions have been suggested in the literature. One approach is to use cut-off distances for each observation location. For the cells which are at a larger distance, covariances are set to zero. Another method proposed in reservoir studies is to localize the covariance matrix with the use of streamlines (Arroyo-Negrete *et. al.*, 2006). In this study also, the streamline trajectories are used for localizing the algorithm.

Another approach for controlling filter divergence is proposed in Anderson and Anderson (1999) where the background error covariances are increased by inflating the deviation of background members with respect to their mean by a small amount as shown below in Eqn. 3.17.

$$x^f \leftarrow (1+r)x^f - r\bar{x}^f \quad (3.17)$$

Here the value of inflation factor r suggested in the literature generally varies from 0.0025 to 0.04. The operator \leftarrow denotes a replacement of previous values of x^f . By applying inflation, we discount the influence of past observations on the current analysis. Thus, the influence of an observation on future analyses decays exponentially with time. Thus, covariance inflation localizes the analysis in time.

Optimal Initial Member Selection. Another key issue with EnKF is the selection of initial ensemble members. Because the background covariances are estimated using a finite set, a larger set should provide a better approximation for the covariances. But for the studies involving large-dimensional models, it becomes important that a smaller set of members be considered in order to reduce the computational requirements. Evensen (2004) proposed the use of singular value decomposition (SVD) of the model parameter-based difference matrix for the ensemble. Deng *et. al.* (2006) applied this approach to model selection for reservoir studies. They created a difference matrix using the initial permeability fields of the members. Members are plotted along orthonormal directions using eigen-decomposition of this matrix, and then key members are selected along the first few directions of maximum change. There are two issues with this approach which need to be resolved. First, members are selected based on the permeability values which are static measures, and contain no information regarding flow-related non-linearity. Second, the difference matrix based on permeability values has a dimension equal to the model size. Hence, for real field studies involving hundreds of thousands of cells, eigen-decomposition becomes

computationally intensive. Scheidt and Caers (2007) proposed taking into account the dynamic responses of the models for ranking of members. They use fast streamline simulators to make flow simulations and then select members based on the dissimilarities in the response using kernel principal component analysis (KPCA) and k-means clustering method.

The approach suggested in this work follows various approaches discussed above, but has some key improvements. Firstly, dissimilarities in this study are based on the evolution of swept pore volume with time-of-flight of streamlines as compared to (static) permeability based measure or streamline based flow-simulation. In other words, the dynamic response for the model is approximated only by tracing streamlines and computing time of flight without making any flow simulation. These streamline trajectories are generated using the fluid-flux information from a finite-difference simulator. Dissimilarity is defined such that it honours self-similarity ($\delta_{ii}=0$) and symmetry ($\delta_{ij}=\delta_{ji}$). Various measures have been proposed in the literature (Borg and Groenen, 2005) such as Euclidean distance and Canberra distance shown below.

$$\text{Euclidean distance, } \delta_{ij} = \left(\sum_{a=1}^m (x_{ia} - x_{ja})^2 \right)^{1/2}$$

$$\text{Canberra distance, } \delta_{ij} = \sum_{a=1}^m \frac{|x_{ia} - x_{ja}|}{|x_{ia} + x_{ja}|}$$

Different measures are suitable for different applications/datasets. For example, Canberra distance corrects the absolute difference along each dimension for the size of

the coordinates along the axis. These measures give the vertex to vertex distances, but various other complex distance measures have also been proposed in literature. Such as Hausdorff distance between two surfaces S and S' given by:

$$d(S, S') = \max_{p \in S} \min_{p' \in S'} \|p - p'\|_2$$

It is more useful for comparing topology rather than calculating simple vertex to vertex distances. Secondly, it is desired from a sequential data assimilation point of view that the variance for the dynamic response of members be preserved throughout the production history. For this reason, evolution of swept pore volumes for various time-of-flight values is considered as dissimilarity measure shown in Eqn. 3.18.

$$d_{p,q} = \left(\sum_i (SPV_{p,\tau_i} - SPV_{q,\tau_i})^2 \right)^{1/2} \quad (3.18)$$

where $d_{p,q}$ is the dissimilarity between member p and q , and $SPV_{j,i}$ is the swept pore volume for member j at time-of-flight value of i . And finally, the dynamic responses are non-linearly separable in real space and so spectral clustering is used to extract the key members. Out of various spectral clustering algorithms proposed in the literature, we use the formulation suggested in Ng *et. al.* (2001). The key steps in spectral clustering of a given set of points $S = \{s_1, s_2, \dots, s_n\}$ in \mathfrak{R}^l into k subsets are as follows:

(i). An affinity matrix $A \in \mathfrak{R}^{n \times n}$ defined by $A_{ij} = \exp\left(-\|s_i - s_j\|^2 / 2\sigma^2\right)$ if $i \neq j$, and $A_{ii} = 0$ is formed.

(ii). A diagonal matrix D whose (i, i) -element is the sum of A 's i -th row is defined, which is used to construct the matrix $L = D^{-1/2} A D^{1/2}$.

(iii). The k largest eigenvectors of L is chosen to form the matrix

$X = [x_1 x_2 \dots x_k] \in \mathfrak{R}^{n \times k}$ by stacking the eigenvectors in columns.

(iv). The matrix Y is formed by renormalizing each of X 's rows to have unit length; i.e.

$$Y_{ij} = X_{ij} / \left(\sum_j X_{ij}^2 \right)^{1/2} .$$

(v). K-means or any other clustering algorithm is then used to cluster Y into k clusters, using each of Y 's row as a point in \mathfrak{R}^k .

(vi). Finally, the original point s_i is assigned to cluster j if and only if row i of the matrix Y was assigned to cluster j .

Eqn. 3.19 shows radial basis function $A(\cdot, \cdot)$ which is used to calculate the similarity between members using the dissimilarity values.

$$A(x_p, x_q) = \exp \left(-\frac{d_{p,q}^2}{2\sigma^2} \right) \quad (3.19)$$

where $A(\cdot, \cdot)$ is the radial basis function, and σ is the characteristic scale length which has a large impact on the cluster tightness. This similarity measure is further used in formulating the affinity matrix. In this study, within cluster sum of squares is used as the measure of cluster tightness and the clustering process is iterated to find the optimal σ value.

3.2.7 Compositional Data Assimilation Study

Oil-production in the reservoir may be supported by either water-injection or carbon-dioxide (CO₂) injection. In case of water-injection, simpler black-oil mode of reservoir simulation is used, but for CO₂ injection supported production, a more complex compositional mode of reservoir simulation is required. Also, we require compositional streamlines for localizing the EnKF algorithm based on the observation location. Molar flux information from the finite-difference simulator is converted to phase fluxes for tracing compositional streamlines as shown in Eqn. 3.20 below:

$$\bar{u}_t = \left(\frac{R}{B_g} + \frac{1-R}{B_o} \right) \sum_{k=1}^{n_c} \bar{u}_{t,k} + \frac{\bar{u}_w \bullet \rho_w}{B_w} \quad (3.20)$$

The above equation shows the calculation of overall phase velocity \bar{u}_t (rb/day) from the molar velocity $\bar{u}_{t,k}$ for each component (lb-m/day), phase velocity of water \bar{u}_w (stb/day), molar density of water ρ_w (lb-m/stb), phase reservoir molar density B_i (lb-m/rb), and gas/oil potential ratio, $R = \phi_g / \phi_o$.

Once total flux has been calculated, streamlines are generated using the algorithm discussed in Jiminez *et. al.* (2008) and the time of flight is computed as follows:

$$\tau = \int \frac{ds}{v_t}$$

where s is the distance along the streamline and v_t is the interstitial velocity given by $|u_t|/\phi$.

3.3.Application and Results

The EnKF algorithm as mentioned above was used for hydrocarbon reservoir data assimilation study. Results from different data assimilation for a synthetic and a field case are discussed in detail in this section. First, a two-dimensional synthetic case with a five-spot well pattern is studied for verification of the EnKF algorithm. Next, EnKF is used for data assimilation study of Weyburn field which is situated in the Saskatchewan province of Canada and is operated by EnCana. Table 3.1 shows some key information about the oilfield. It has been under production since 1957 as shown in Figure 3.3. Production was supported by water injection until October 2002, after which both water and carbon-dioxide were injected. Table 3.2 shows the geologic information of the reservoir. There are three key geological zones in the producing Midale reservoir of the Weyburn field. The upper zone is a dolostone, marly reservoir which has good matrix permeability (upto 100md) and low to moderate fracture density. The lower two geologic zones are limestone, vuggy reservoir. Upper vuggy has relatively low matrix permeability (upto 20md) and high fracture density, while lower vuggy zone has higher matrix permeability (upto 500md) and moderate to high fracture density.

Table 3.1: Key data for Weyburn field (Burrowes, 2001)

Discovered	1954
Area	70 sq miles
Depth	4760 ft
Original oil in place (OOIP)	1400 MMbbls
Cumulative oil production (Pan, 2006)	~390 MMbbls
Current oil production rate	18,000 BOPD
Number of wells	1016 (total)
Vertical producers	660
Horizontal producers	158
Injectors	197

Table 3.2: Geology of Weyburn field (Burrowes, 2001)

Reservoir zone	Lithology & Texture	Porosity	Matrix Permeability (md)	Heterogeneity	Fracture Density
Marly	Dolostone	0.2-0.37	<0.1-100	Low	Low-Moderate
Upper vuggy	Limestone	0.02-0.15	<0.01-20	Medium	High
Lower vuggy	Limestone	0.05-0.2	<1-500	High	Moderate-High

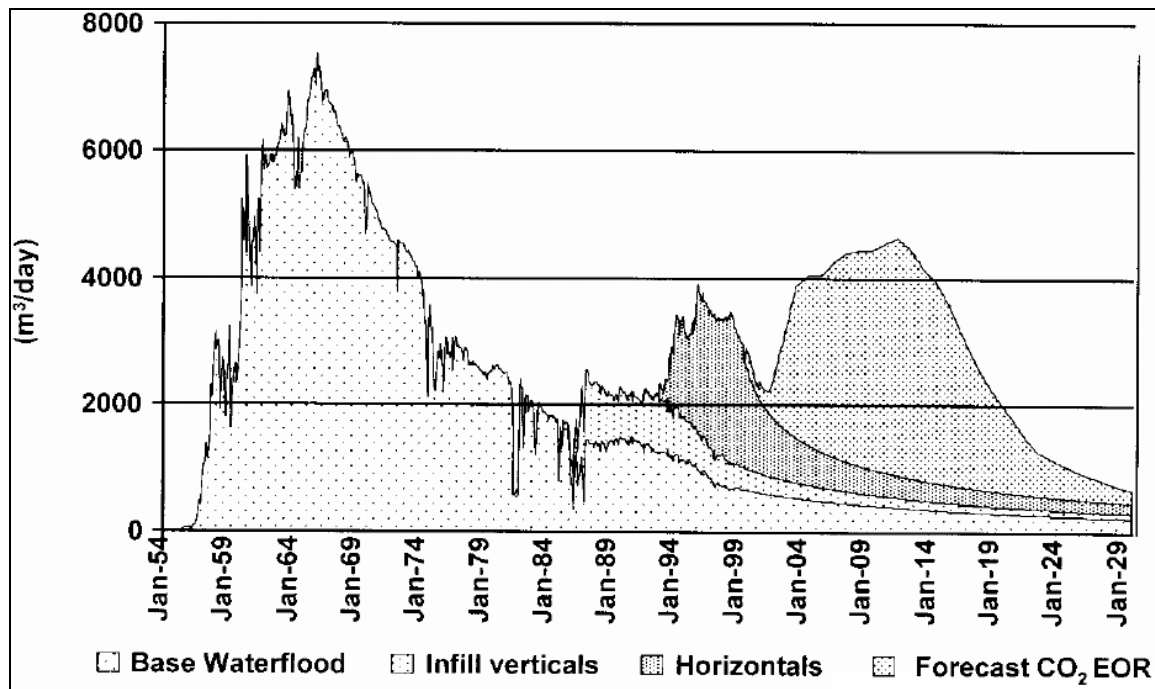


Figure 3.3: Production history and forecast, Weyburn field, Saskatchewan (adapted from Burrowes, 2001)

3.3.1 Optimal Member Selection

As discussed above, the EnKF algorithm starts with a number of initial geologic models which have sufficient variance so as to contain the true solution within the subspace. This in turn requires generating a very large number of models to capture the various possibilities for a complex production scenario like Weyburn. It would be computationally challenging to use all models in the data assimilation study for a large field case; therefore it is desired to reduce the ensemble size while keeping the solution subspace large enough. The true permeability field for the five-spot, two-dimensional synthetic case is shown in Figure 3.4(a), while Figure 3.4(b) shows the streamline for one of the four production wells. Observations from this well are used to update

permeabilities for the grids through which these streamlines pass. Streamline derived swept pore volume is used for selecting the key members as illustrated in Figure 3.5. Figure 3.6 compares the field water cut for all 100 members and that for a 40-members selection before history-match. Throughout the production history of 4000 days, spread in the water-cut response has been preserved by the selected members. Figure 3.7 shows the same comparison but after data assimilation using EnKF. Even after data assimilation, spread in the water-cut response is the same for 100 members as that for the selected 40 members. Next, we show the results for member selection for a small section of Weyburn field. Streamlines were traced for all initial 40 geologic models. Figure 3.8(a) shows the evolution of swept pore volume with time of flight values for each model, while Figure 3.8(b) shows the differential swept pore volume for different time of flight values. 20 members were selected using the spectral clustering approach described earlier. Figure 3.9 shows the spread in oil production rates for three wells using all 40 initial members, while Figure 3.10 shows the same but using the 20 selected members. Selected members are able to capture the production response spread throughout the 45 years of history, which is critical for a sequential filtering algorithm like EnKF. Before assimilating data, we compare the responses from the mean of all 40 members and that from the mean of the selected 20 members in Figure 3.11 to verify if bias in the response was introduced at the field level due to the member selection process. There was no bias introduced at the field level, and both mean permeability fields gave similar responses. Figure 3.12 and Figure 3.13 compare the data assimilation results using mean permeability fields for all 40 members and for the

selected 20 members. Both means shows improved match after assimilation, but because the EnKF algorithm has stochastic component, the degree of improvement varies a little for the two cases. Figure 3.14 shows the mean permeability for layer 6 before and after history-matching. Changes in permeabilities are of similar nature for both the assimilation studies.

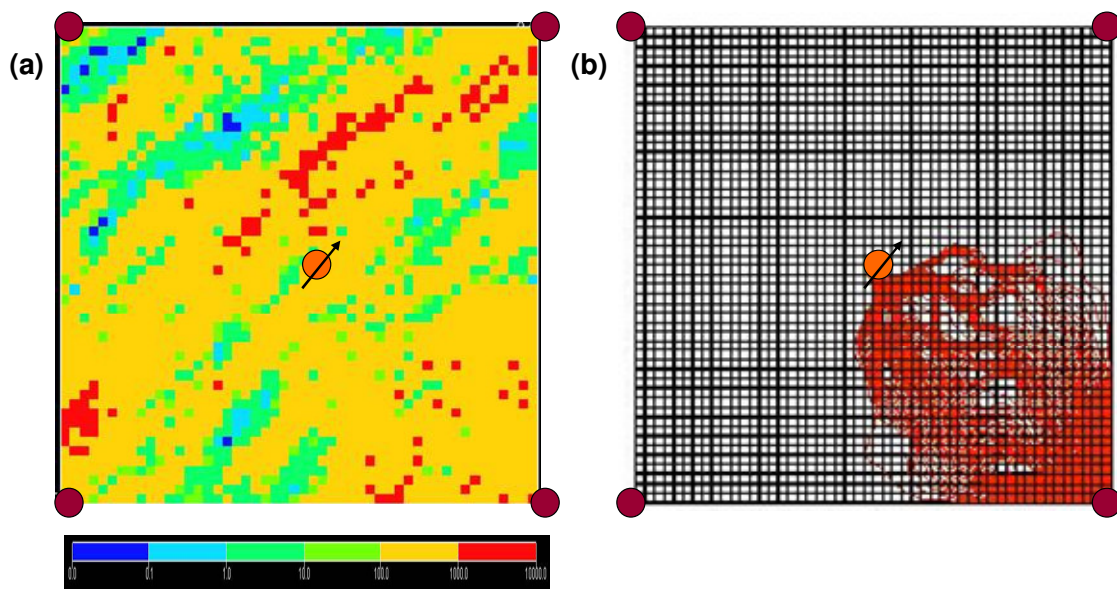


Figure 3.4: (a) True Permeability Field for 2D synthetic case, and (b) streamlines for one production well used for localization

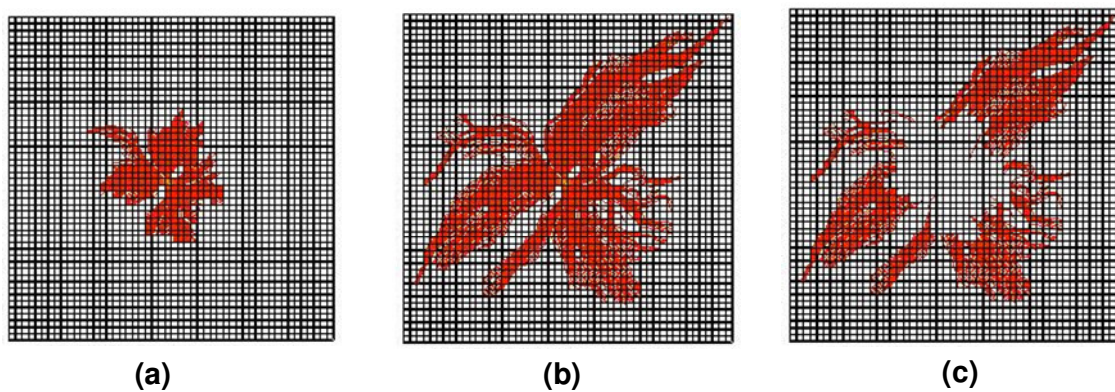


Figure 3.5: (a) Streamlines for time of flight=1000 days, (b) streamlines for time of flight=5000 days, and (c) extra volume swept between the two time of flight values

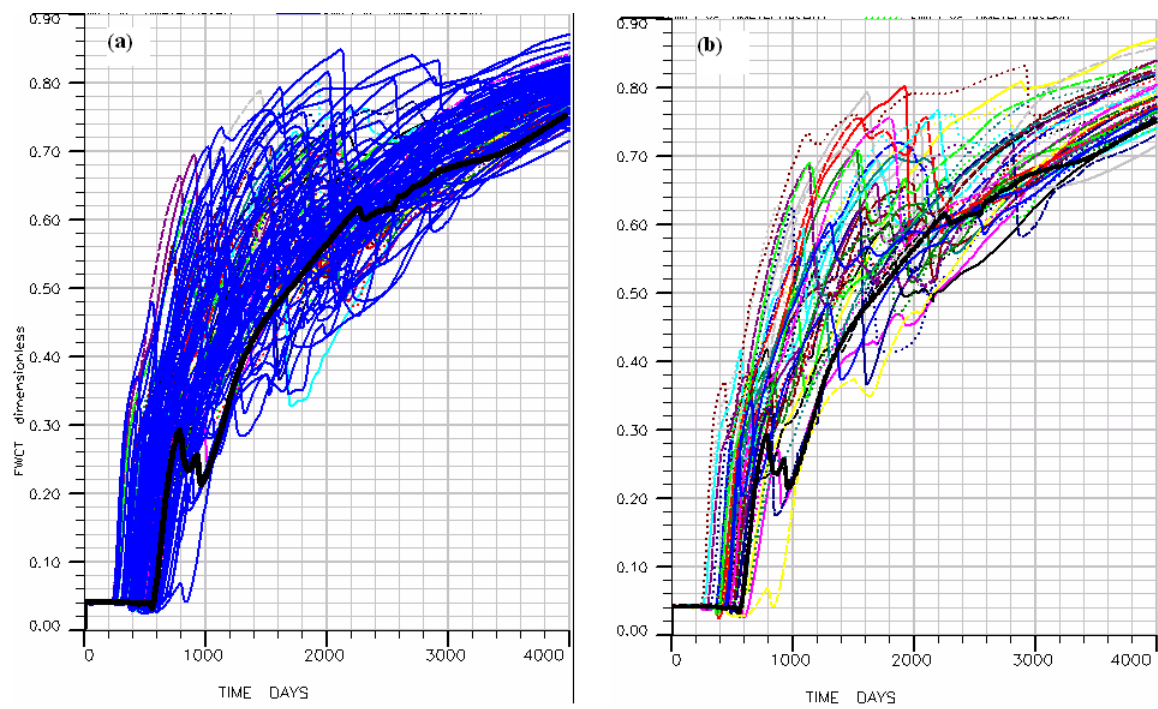


Figure 3.6: Field water cut before history-match for (a) all 100 members, (b) selected 40 members. Thick black curve shows the response for true model

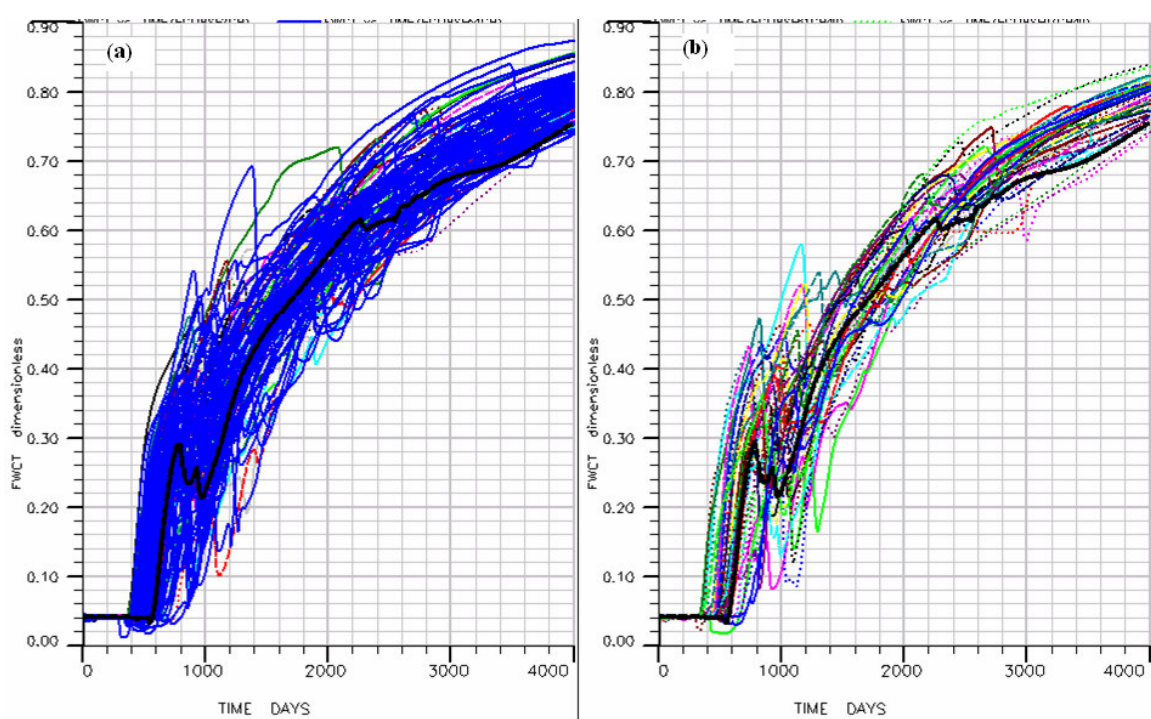


Figure 3.7: Field water cut after history-match for (a) all 100 members, (b) selected 40 members. Thick black curve shows the response for true model

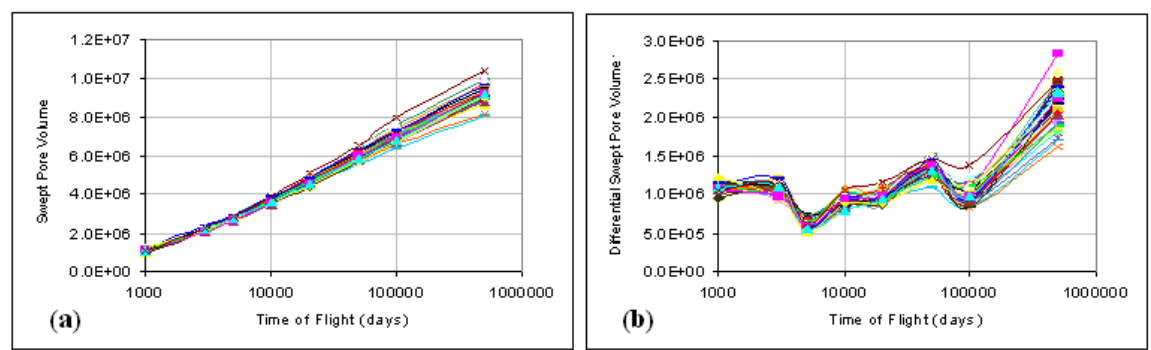


Figure 3.8: (a) Swept pore volume (in cu ft), and (b) differential swept pore volume (in cu ft) with time of flight increments for small section of Weyburn field

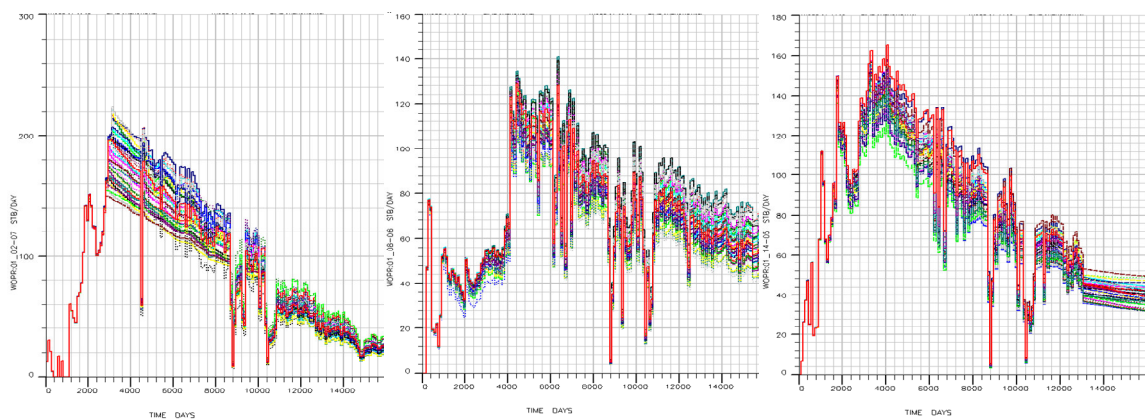


Figure 3.9: Spread in oil production rates for three wells using all 40 members

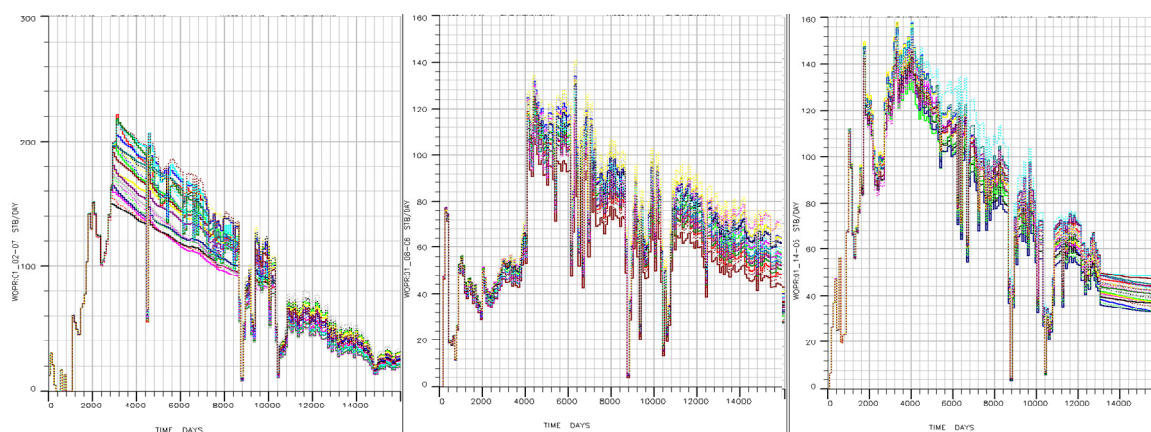


Figure 3.10: Spread in oil production rates for same three wells as in Figure 3.8, but for selected 20 members

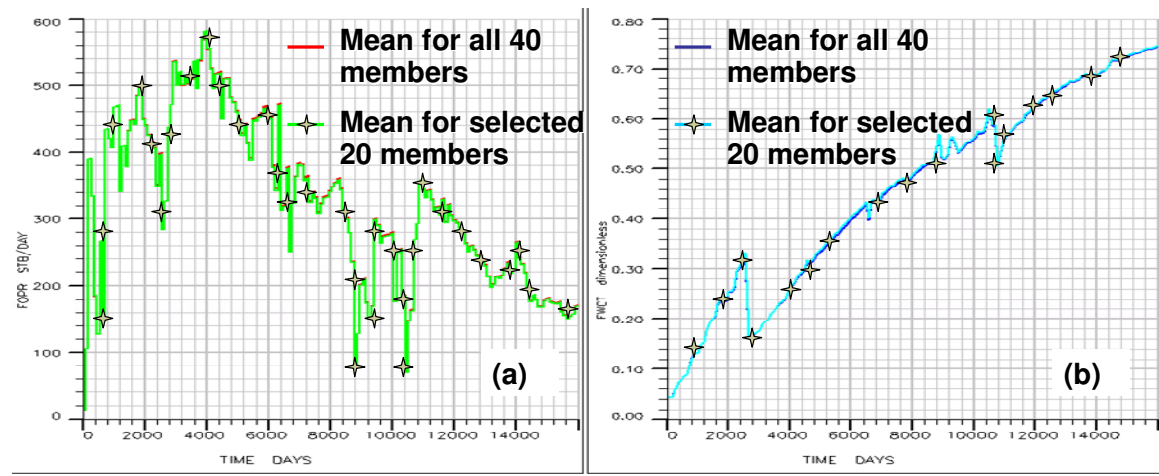


Figure 3.11: Comparison of responses for mean permeability fields for all 40 members and the selected 20 members, (a) field oil production rate, and (b) field water-cut

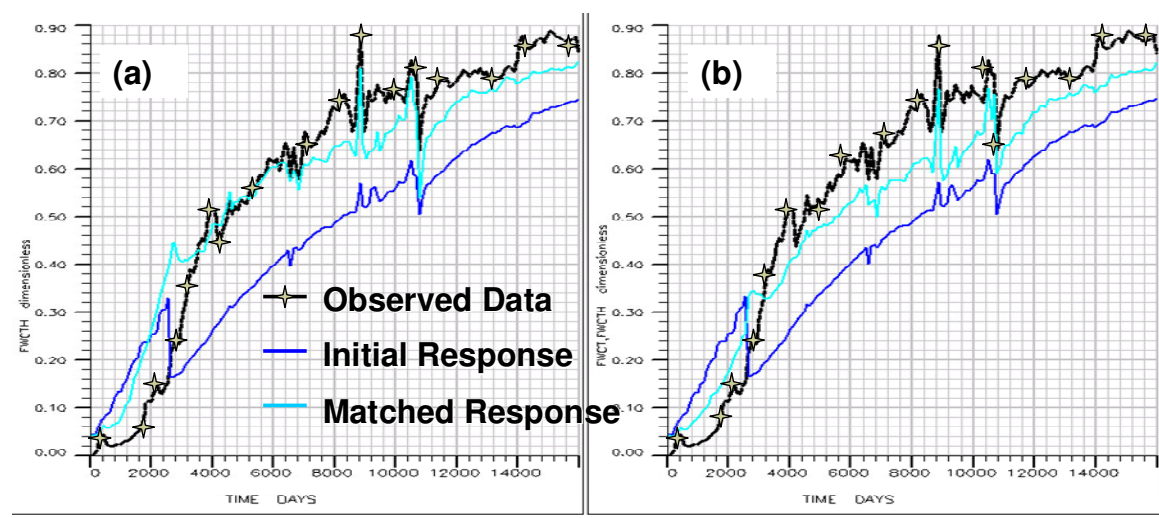


Figure 3.12: Comparison of field water-cut from mean permeability fields for (a) selected 20 members, and (b) all 40 members

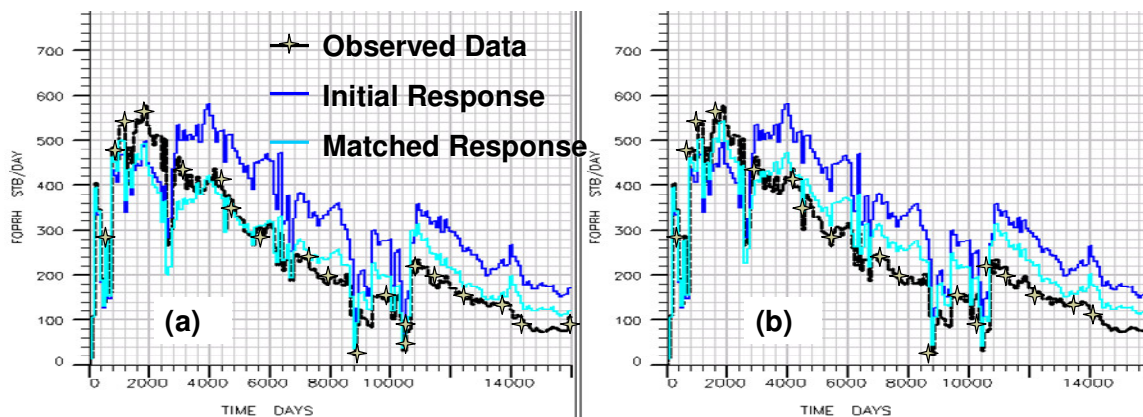


Figure 3.13: Comparison of field oil production rate from mean permeability fields for (a) selected 20 members, and (b) all 40 members

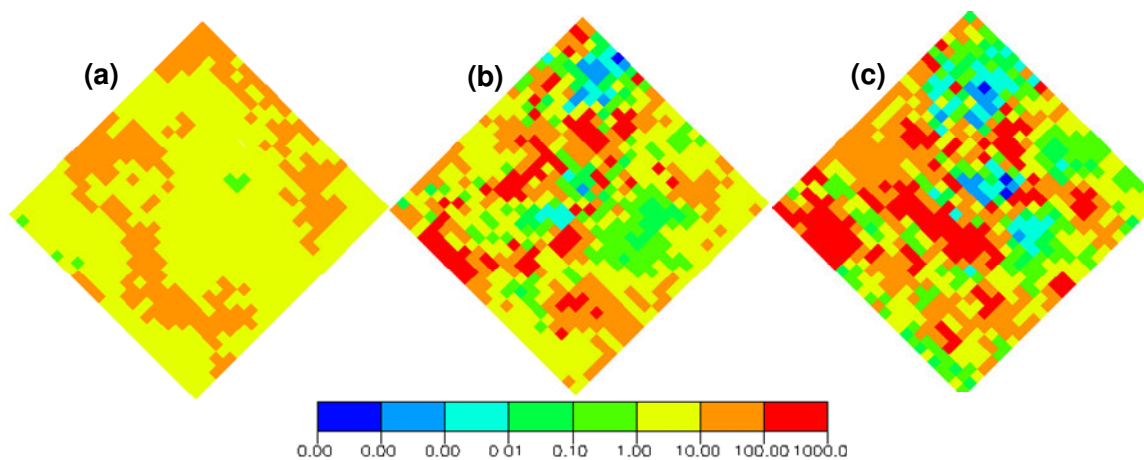


Figure 3.14: Mean permeability values (in md) for layer 6: (a) before history-matching, (b) after history-matching using all 40 members, and (c) after history-matching using selected 20 members

3.3.2 Large-Scale Data Assimilation Study

In this section, results from the full-field data assimilation study of Weyburn field are discussed. The main idea behind this section is to study the efficacy of the EnKF algorithm in handling a large reservoir study with significant production history. Figure 3.15 shows the three-dimensional view of the mean permeability of the initial geologic

models provided by Encana. Figure 3.16 shows the initial mean permeability profiles for layer 4 from marly, layer 10 from upper vuggy, and layer 24 from the lower vuggy zone. Each zone has its own matrix permeability range. Next, oil production rate data were assimilated using the EnKF algorithm that resulted in changes of large magnitude which made forward simulation unstable. Hence, different cut-offs were applied for each of the three geologic zones as suggested in Burrowes (2001). This in turn forced EnKF to make plausible changes. It should be noted that localization was not used at this stage. The updated mean permeability profiles for the same layers as in Figure 3.16 are shown in Figure 3.17. But still the changes were limited mainly by the cut-off values. Figure 3.18 shows the comparison of field oil production rates from the mean of initial permeabilities and that from the mean of history-matched permeabilities. Figure 3.19 shows the same comparison for field water-cur and water injection rate. The initial mean permeability model overestimates the oil production, and EnKF tries to bring it down. But EnKF makes too many changes and the mean of history-matched ensemble permeabilities underestimates the production. This behavior is due to the spurious covariances between a well production rate and far-off cell permeabilities as discussed previously. Hence, the next figure shows results from data assimilation using (streamline based) localized EnKF. Figure 3.20 shows the comparison of field oil production rates from the mean permeability fields of history-matched ensembles using EnKF with and without localization. The match is better for assimilation with localization as compared to that for assimilation without localization. Figure 3.21 shows the updated mean permeability field for the same layers as in Figure 3.17. Lesser

changes to the initial geologic fields were made, and yet a better match for field oil production rate was achieved with localized assimilation as compared to that from assimilation without localization. Thus, it can be concluded that localization is critical when assimilating data for a large field with significant production history. Figure 3.22 shows oil production rates for six wells simulated using initial geologic models. Dark black curves show the historical oil production rate. Figure 3.23 shows the oil production rates for the same six wells as in Figure 3.22, but when simulated using updated permeabilities. The production rate match improves for each of the six wells after updating initial geologic models. Figure 3.24 shows the histogram for lower vuggy reservoir before and after history matching. Stochastic diffusion flattens the histogram at each step of assimilation process. Also, EnKF makes relatively larger changes to permeability as compared with localized EnKF. Hence, histogram has lower frequency at cut-off values for localized EnKF. Covariance inflation was also tried for enhancing the EnKF algorithm, but it did not yield satisfactory result. Inflation made the forward simulation unstable and the assimilation process itself did not complete.

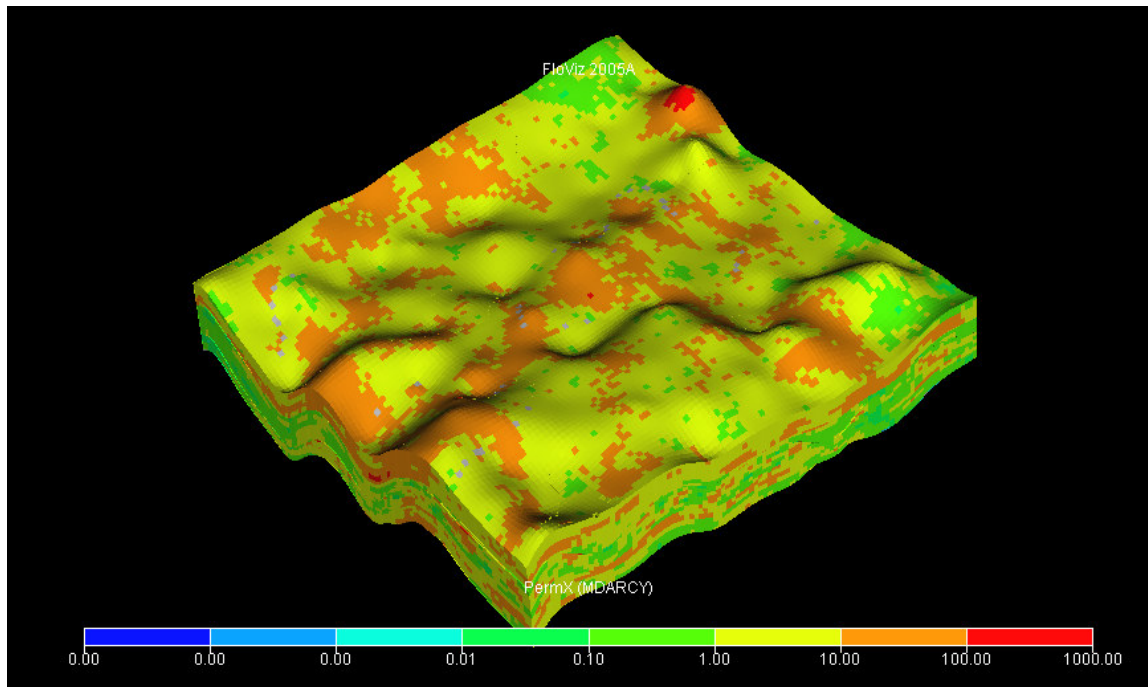


Figure 3.15: Three dimensional view of the Weyburn reservoir under study

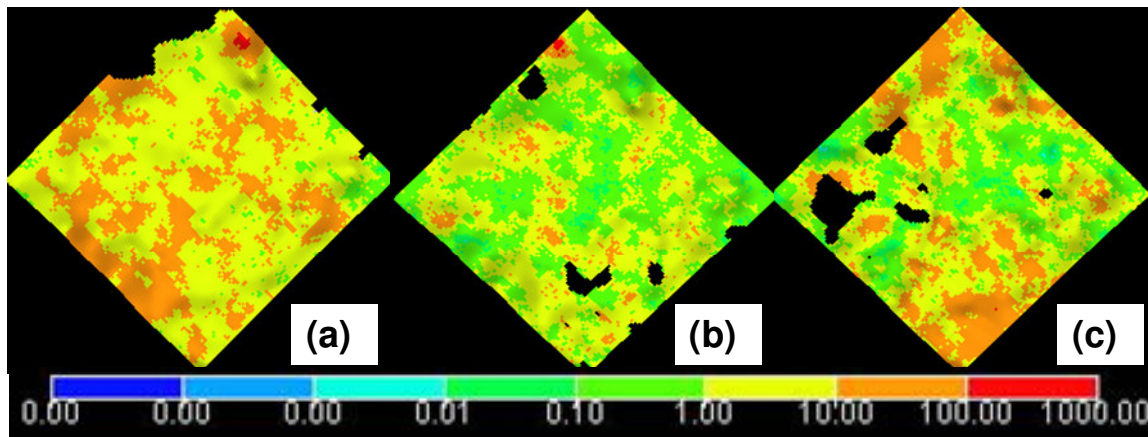


Figure 3.16: Initial permeability (in md) for (a) layer 4 - Marly, (b) layer 10 - Upper Vuggy, and (c) layer 24 - Lower Vuggy

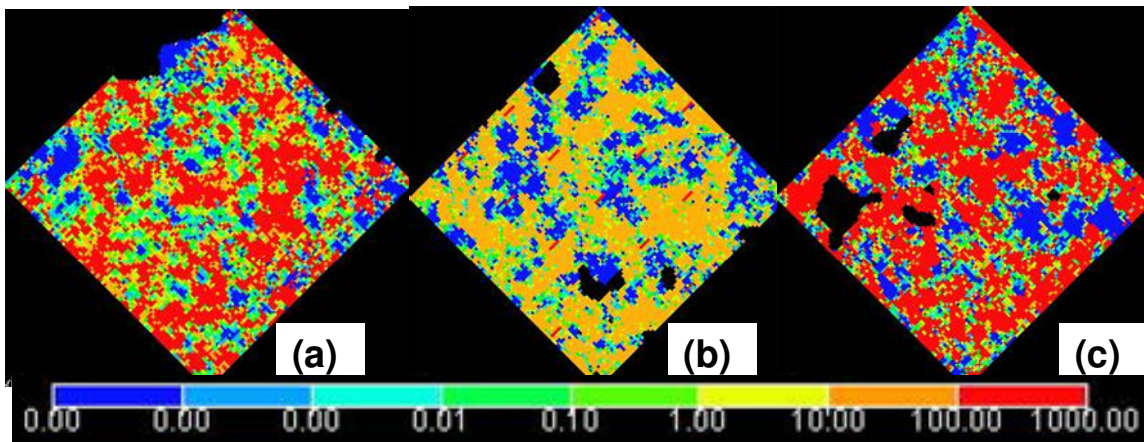


Figure 3.17: Final permeability (in md) after data assimilation using EnKF for (a) layer 4 - Marly, (b) layer 10 - Upper Vuggy, and (c) layer 24 - Lower Vuggy

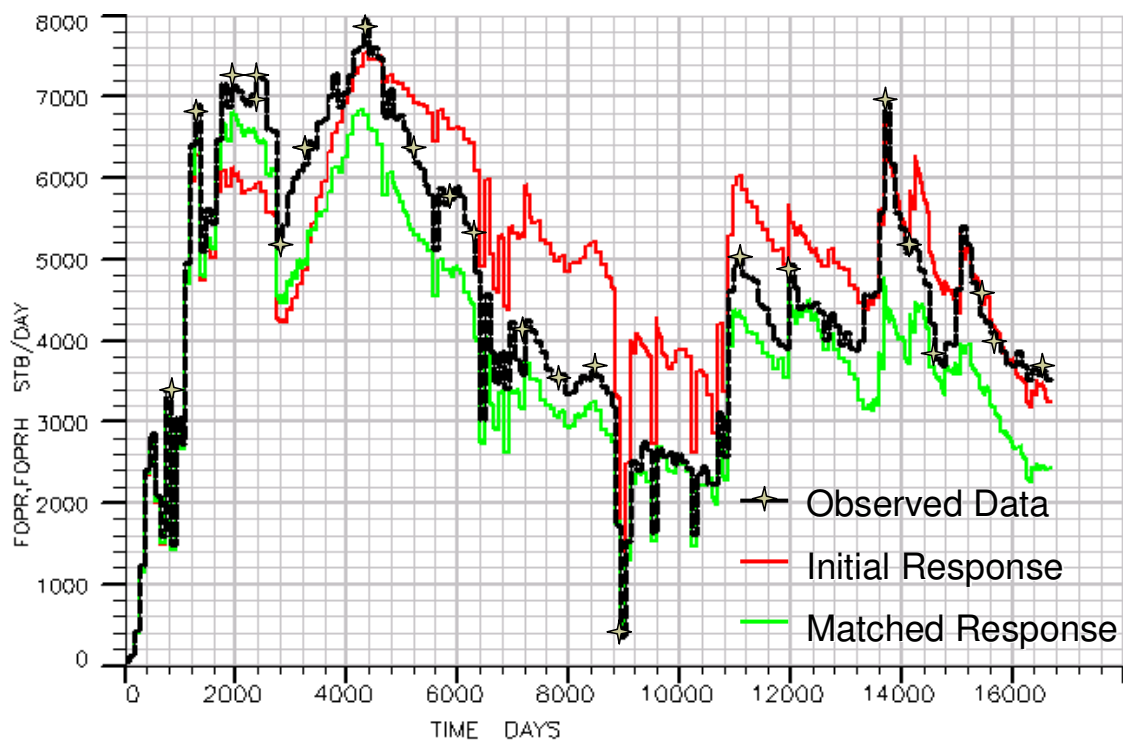


Figure 3.18: Comparison of field oil production rates for mean permeability fields of initial ensemble and history-matched ensemble

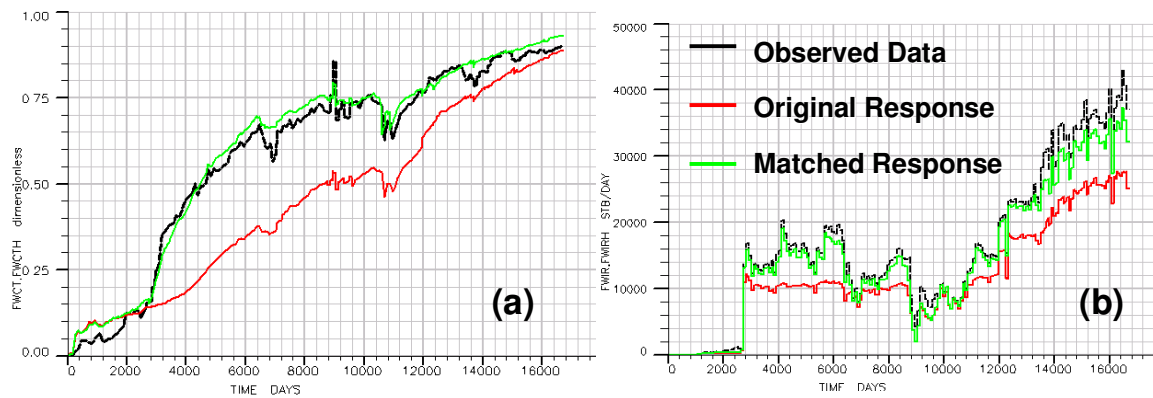


Figure 3.19: Comparison of field (a) water-cut and (b) water injection rate for mean permeability fields of initial ensemble and history-matched ensemble

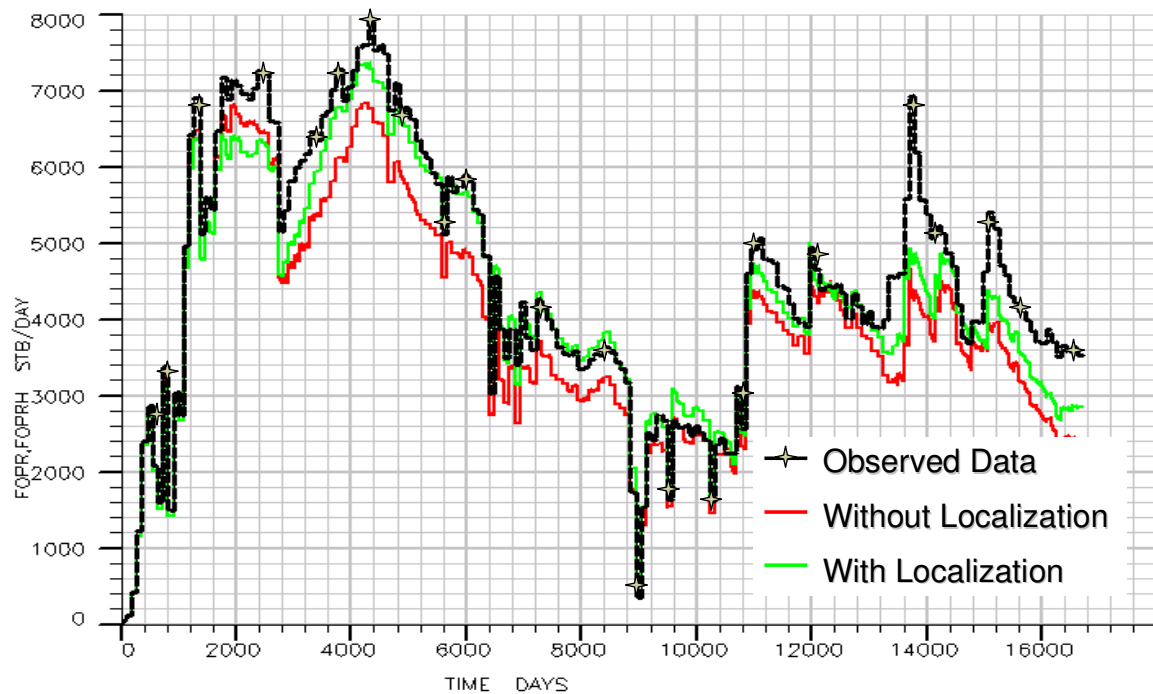


Figure 3.20: Comparison of field oil production rates for mean permeability fields of history-matched ensembles using EnKF with and without localization

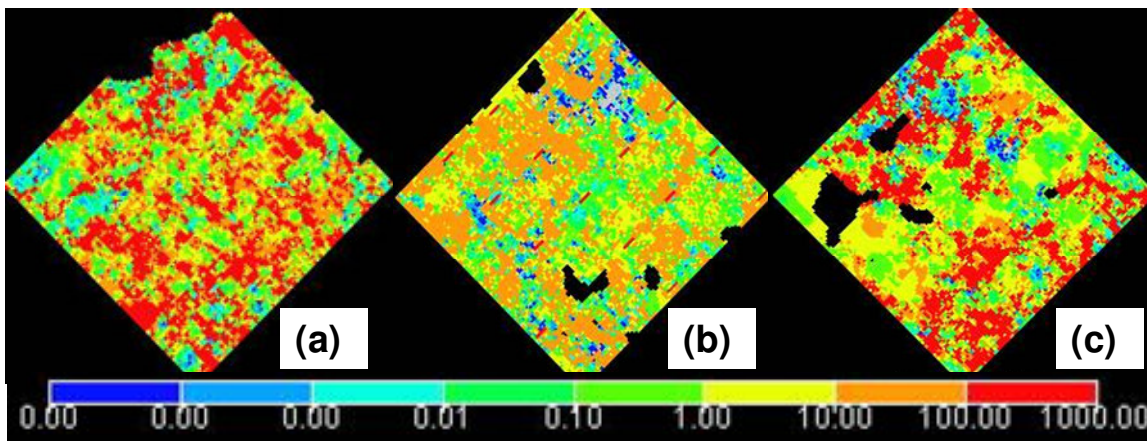


Figure 3.21: Final permeability (in md) after data assimilation using localized EnKF for (a) layer 4 - Marly, (b) layer 10 - Upper Vuggy, and (c) layer 24 - Lower Vuggy

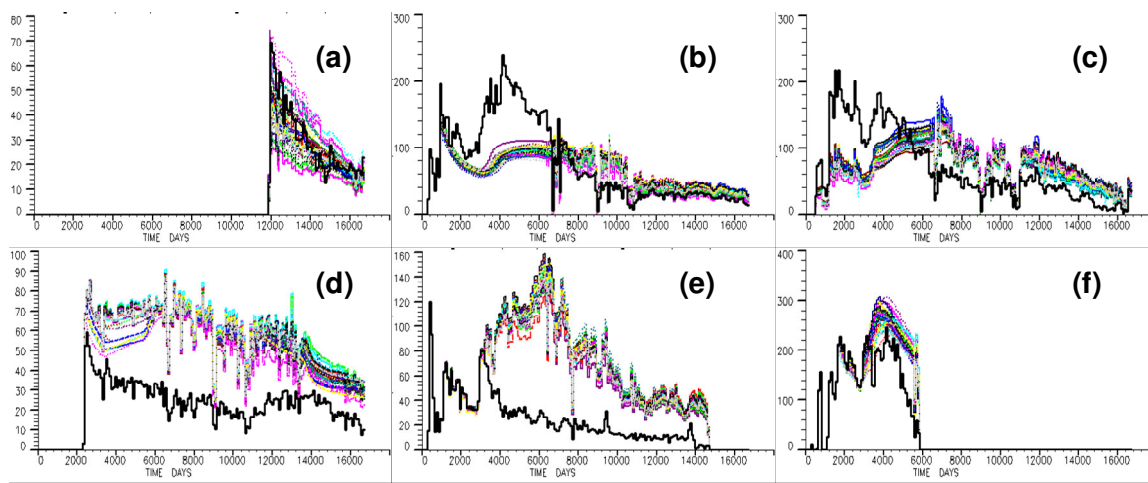


Figure 3.22: Oil production rates for well (a) 01_03-04, (b) 01_14-06, (c) 01_14-29, (d) 01_10-01, (e) 01_04-07, and (f) 01_10-32 using initial geologic models. Dark curves show the historical oil production rates for the same wells

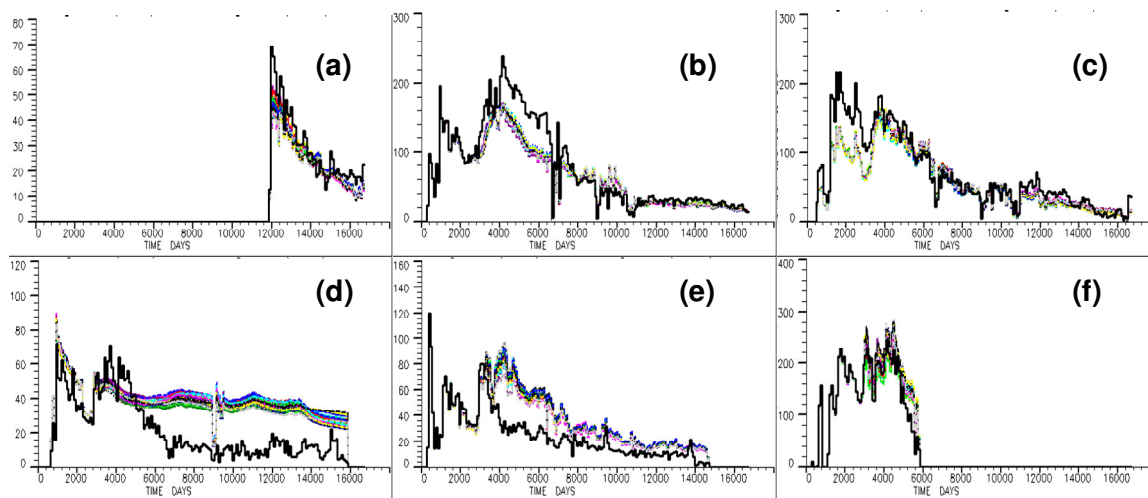


Figure 3.23: Oil production rates for well (a) 01_03-04, (b) 01_14-06, (c) 01_14-29, (d) 01_10-01, (e) 01_04-07, and (f) 01_10-32 using updated models. Dark curves show the historical oil production rates for the same wells

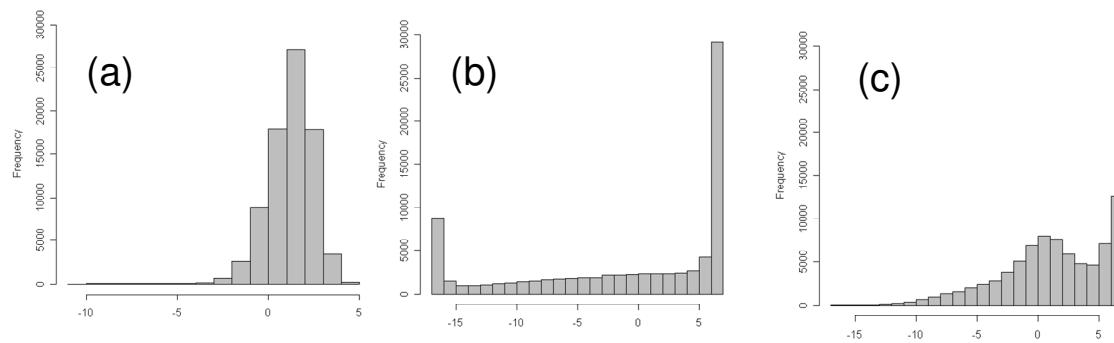


Figure 3.24: (a) Histogram of lower vuggy permeability values before history matching, and after history matching (b) without localization and (c) with localization

3.3.3 Compositional Data Assimilation

Since October 2002 carbon-dioxide has been injected in the Weyburn oilfield. The goal is twofold, to sequester carbon-dioxide produced from a nearby power-plant and to have enhanced oil recovery from miscible flow. During the first 45 years of production supported by water-injection, around 325 MMbbls of crude oil were produced. It is

expected that gas injection should facilitate 155 MMbbls of incremental crude oil production while sequestering 30 million tonnes of CO₂ during the next 30 years (Pan, 2006). Assimilating data for such a production scenario requires compositional simulation. Some key compositional simulation input data are shown in Table 3.3. Also, compositional streamlines are required for localizing the assimilation process. As mentioned in the previous section, compositional streamlines were generated using flux information from a finite difference simulator. Figure 3.25(a) shows a two-dimensional permeability field with five-spot well pattern, and Figure 3.25(b) shows the streamlines for the same. As can be seen, streamline density is higher along higher permeability streaks. Figure 3.26 shows the compositional streamlines for the Weyburn field at a particular time-step. Next, results from assimilation using a compositional model are compared with those from assimilation using a black-oil model for a small section of Weyburn field. Figure 3.27(a) shows the field oil production rate responses using the two simulation method and the mean permeability of initial geologic models. Because of the differences in simulation initialization and PVT models for the two cases, there are differences in responses using the same initial mean permeability field. Next, we update the models using black-oil and compositional methods separately and compare the responses from the mean of the two sets of updated permeability models in Figure 3.27(b). Again both show similar improvements in the match after assimilation. Thus we may conclude that our approach can be effective for both black-oil and more complex compositional modeling.

Table 3.3: Component information for the compositional simulation

Name of component	CO ₂	C1N ₂	C2C ₃	C ₃	C ₇₊	C ₂₅₊
Molecular weight	44.01	18.19	37.78	70.35	182.17	498.89
Parachor	78.00	70.54	131.25	225.76	491.80	1257.25
Critical pressure	1071.34	637.16	649.29	487.85	287.64	97.95
Critical temperature	548.46	321.36	612.75	829.10	1213.42	1728.17
Critical volume	1.51	1.55	2.83	4.84	11.37	30.54
Volume shift parameter	-0.04	-3.75E-06	-0.09	-0.04	0.08	0.32
Initial overall mole fraction	0.01	0.13	0.10	0.11	0.48	0.17

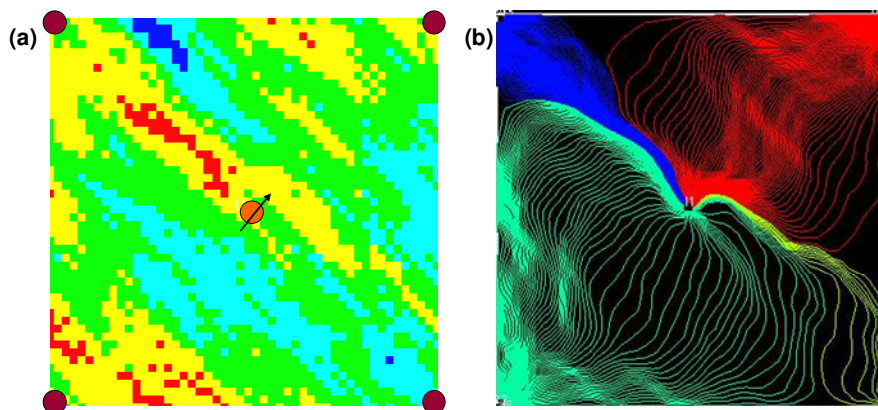


Figure 3.25: (a) A two-dimensional synthetic permeability field with five-spot well pattern, and (b) compositional streamlines for the same

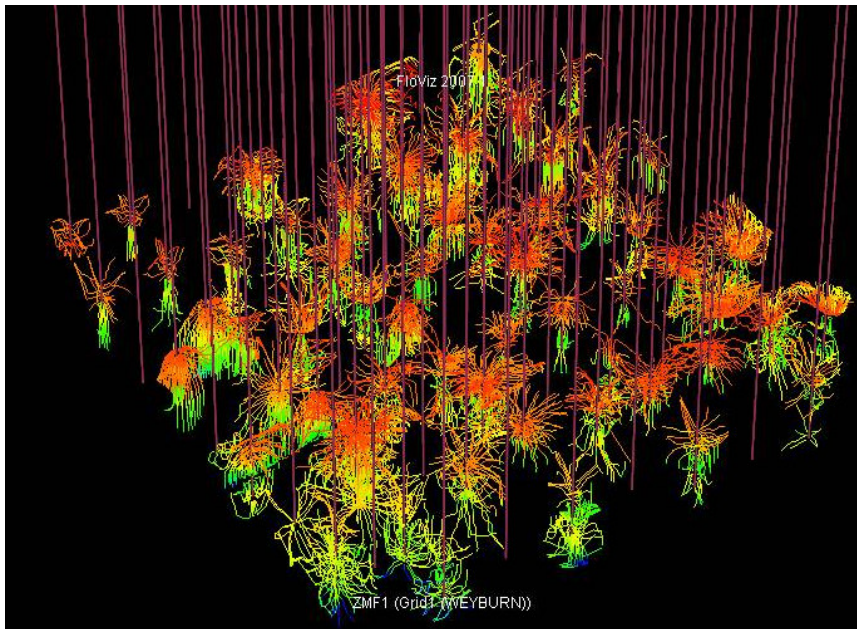


Figure 3.26: Compositional Streamlines for the Weyburn oilfield

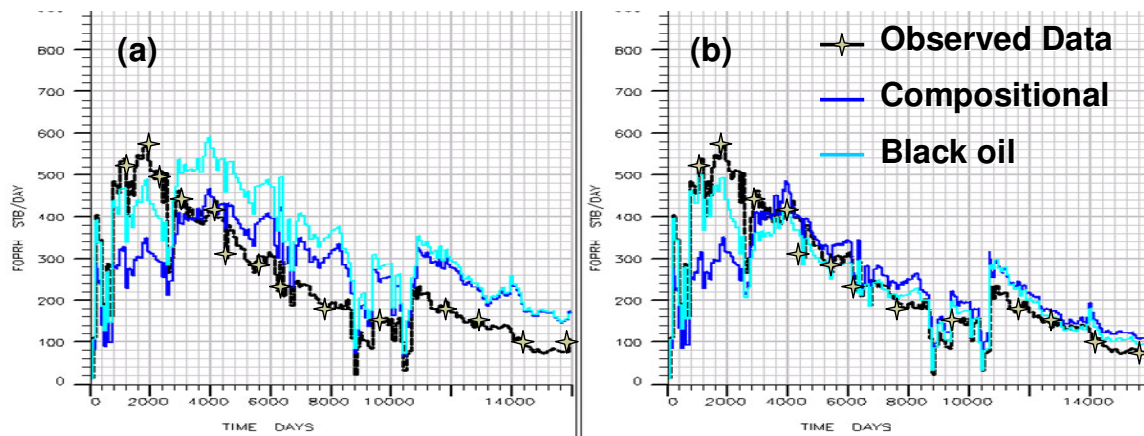


Figure 3.27: Comparison of data assimilation results using black-oil and that using compositional model for small section of Weyburn field. (a) Field oil production rate using the means of initial geologic ensemble, and (b) using the means from final updated ensembles. Dark curves show the historical field oil production rate

CHAPTER IV

TIME-LAPSE SEISMIC STUDY OF THE WEYBURN FIELD

4.1.Introduction

Seismic data contain information regarding lithology, pore-pressure, and saturation heterogeneity. Various studies in the past have used actual seismic data attributes like amplitude and phase, as well as derived seismic parameters like P- and S-wave impedances, for heterogeneity characterization. Data may be collected at one particular time for the estimation of static parameters such as permeability and porosity. It may also be collected at various times for the estimation of dynamic behavior such as pressure and saturation changes, which may then be used for static parameter estimation. In this chapter, time-lapse seismic attributes of P- and S- wave propagation are examined for the Weyburn field. The goal is to understand the pore-pressure and pore-fluid variations in the reservoir. As mentioned in section 3.3.3, CO₂ injection has been carried out in Weyburn field since October 2002 for enhanced oil recovery and carbon sequestration. One of the key requirements for designing such a process is to have a good understanding of the formation pressure and saturation variation with time.

Many similar studies using time-lapse seismic data have been performed in the past for various oilfields, including the Weyburn oilfield. Yamamoto (2003) carried out such a study using P-wave impedance data for a better understanding of permeability

heterogeneity within the producing formations of the Weyburn oilfield. Hiro used a simplistic Gassman law based rock-physics model to numerically simulate the impedance values, and then compared them with those derived from the true seismic data. He concluded that the large impedance changes for P-wave in the top Marly formation assisted in understanding the preferred direction of CO₂ movement in the reservoir. This in turn helped in better understanding the vertical permeability for the reservoir.

4.2.Pore-pressure and Pore-fluid Discrimination for the Weyburn Field

Seismic data for the Weyburn field were available at two times, December 2004 and November 2005. Production was supported by both water and CO₂ injection during this period. The main goal of this study was to correctly identify what parameters affect the time-lapse response of the reservoir. Permeability and porosity were the key static parameters, while gas saturation, pore-pressure, and CO₂ mole fraction were the key dynamic parameters studied. The time-lapse response as simulated numerically was compared with that from observed data.

4.2.1 Rock-Physics Model

The Operating company, Encana, provided empirical equations for P- and S- wave impedance calculations. These equations were derived using numerous experiments

performed under varying pressure, saturations, and temperature conditions (Syhlonyk,1998). 5 core samples from Midale Marly Porous, Midale Vuggy Porous, and Midale Vuggy Tight formations of the Weyburn field were used for the acoustic velocity measurements. Stock tank oil and simulated formation brine from the same reservoir were used for compressional velocity measurements at ambient conditions. Results from compositional reservoir simulation were used as input for P-impedance calculation. The calculation steps for various rock-physics parameters are discussed next.

The seismic attribute values are calculated for different geologic layers, which in turn are comprised of several layers in the reservoir simulation model. Table 4.1 shows the geologic sections considered for time-lapse study and the corresponding reservoir simulation layers. Pore pressure ($pore_pres$), water (S_w), oil (S_o), and gas (S_g) saturation, water (ρ_w), oil (ρ_o), and gas (ρ_g) density, and total fluid compressibility (c_{tot}) values at any time are derived from the compositional reservoir simulator.

Porosity (ϕ) is assumed to remain constant. Other inputs used in this study are σ_{vert} , σ_{horz_min} , and compression axis pressure ($comp_axis_pres$).

The following equations show the steps considered in the calculation of seismic attributes of marly section.

$$\text{Net overburden pressure, } nob_pres = comp_axis_pres - pore_pres$$

Total fluid density, $\rho_{tot} = \rho_w \times S_w + \rho_o \times S_o + \rho_g \times S_g$

Overall density, $\rho = \rho_m + \rho_{dp} + \rho_{df}$,

where

Matrix density, $\rho_m = 2819.2 \times (1 - \phi)$

Pore density, $\rho_{dp} = 0$.

Pore-fluid density, $\rho_{df} = \rho_{tot} \times \phi$

Overall shear modulus, $\mu = \mu_m + \mu_{dp} + \mu_{df}$, where

Matrix shear modulus, $\mu_m = -43.827 \times (\phi) + 21.319$

Pore shear modulus, $\mu_{dp} = 1.34 \times \log(nob_pres) - 3.84$

Pore-fluid shear modulus, $\mu_{df} = 0$.

$kf_{\log s} = 0.9$

$k_{\log s} = -55.927 \times \phi + 28.38 + (4.07 \times \log(nob_pres) - 11.04)$
 $+ (2/3) \times (-43.827 \times \phi + 21.319 + (1.34 \times \log(nob_pres) - 3.84))$

$k_s = 28.38 + 4.07 \times \log(nob_pres) - 11.04$
 $+ (2/3) \times (21.319 + 1.34 \times \log(nob_pres) - 3.84)$
 $k_* = (k_{\log s} \times ((\phi \times k_s / kf_{\log s}) + 1 - \phi) - k_s) / ((\phi \times k_s / kf_{\log s}) + k_{\log s} / k_s - 1 - \phi)$

Bulk compressibility (using Gassman's approach),

$$c_{bulk} = (\phi \times c_* \times (c_s - c_{tot}) + c_s \times (c_s - c_*)) / (\phi \times (c_s - c_{tot}) + (c_s - c_*))$$

Where

$$c_s = 1/k_s$$

$$c_* = 1/k_*$$

Bulk moduli, $k_{bulk} = 1/c_{bulk}$

$$\lambda = k_{bulk} - (2/3) \times \mu$$

$$\text{P-wave velocity, } V_p = \left(\frac{\lambda + 2\mu}{\rho} \times 10^9 \right)^{0.5}$$

$$\text{S-wave velocity, } V_s = \left(\frac{\mu}{\rho} \times 10^9 \right)^{0.5}$$

$$\text{P-wave impedance, } I_p = \rho \times V_p$$

$$\text{S-wave impedance, } I_s = \rho \times V_s$$

Appendix II shows the similar equations for both upper and lower vuggy sections. The sensitivities of the calculated values to various input parameters are examined in the following plots. Figure 4.1 through Figure 4.3 show the affect of porosity value on the calculated wave velocities and impedances for the four geologic sections. Increase in

porosity across grids leads to decrease in both P- and S- velocities. This is mainly due to decrease of solid present per unit volume. This in turn leads to a decrease in impedances as well. Upper vuggy (V1) layer shows the maximum change in seismic attributes with change in porosity. Figure 4.4 through Figure 4.6 show the affect of net overburden pressure on the calculated wave velocities and impedances for different geological layers. A constant compression axis pressure of 32.5 Mpa was assumed in these calculations. The increase in wave-velocities with increasing net overburden pressure is more dramatic for lower pressure values. For higher pore-pressure values the velocities remain nearly constant. Though an increase is also observed in wave-velocity values of vuggy sections with increasing pore-pressure, the overall increase is less dramatic than that for the marly section. Hence, seismic data should be able to assist in quantifying pressure distribution within the marly section. Figure 4.7 through Figure 4.9 show the affect of supercritical CO₂ saturation on the calculated wave velocities and impedances for the different geological sections. This is seen due to the fact that the density of supercritical CO₂ is in the same order of magnitude as density of in-situ oil or water.

Table 4.1: Correspondence between time-lapse sections and simulation model layers

Time-lapse section	Corresponding simulation model layers
Marly	4-9
Upper vuggy, V1	10-15
Lower Vuggy	16-29
V2	16-21
V4+	22-29

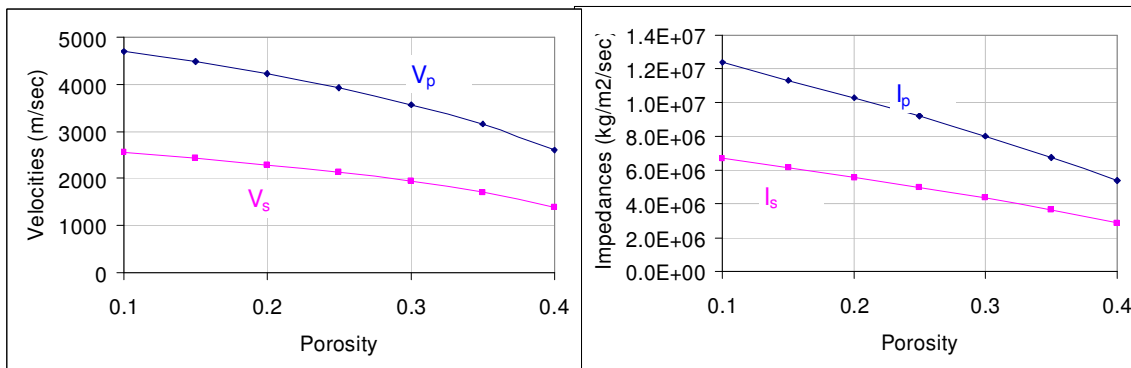


Figure 4.1: Effect of porosity on P- and S-wave velocities (V_p and V_s) and impedances (I_p and I_s) for the marly section

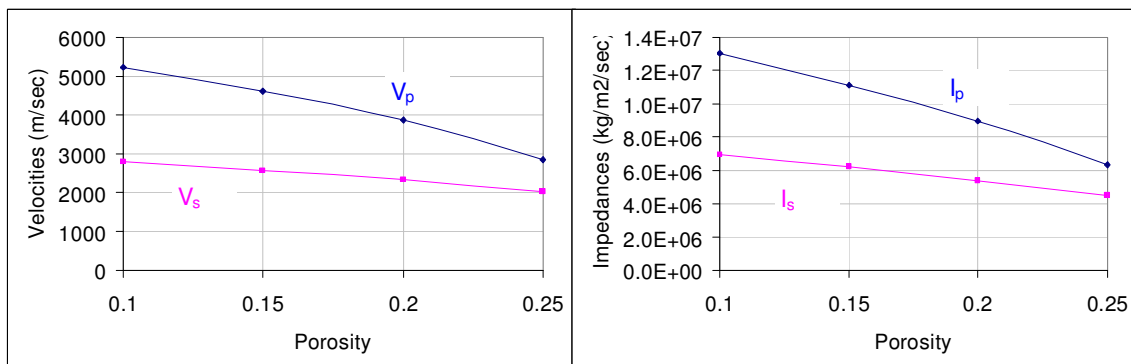


Figure 4.2: Effect of porosity on P- and S-wave velocities (V_p and V_s) and impedances (I_p and I_s) for the upper vuggy section

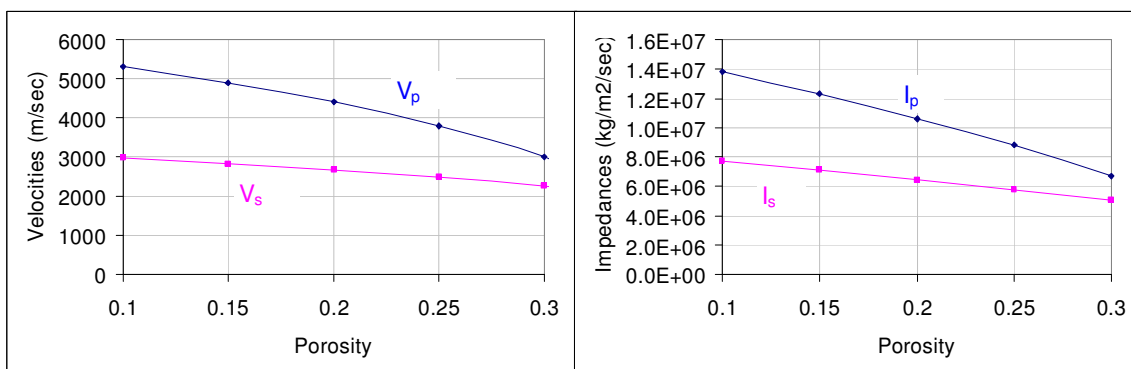


Figure 4.3: Effect of porosity on P- and S-wave velocities (V_p and V_s) and impedances (I_p and I_s) for the lower vuggy section

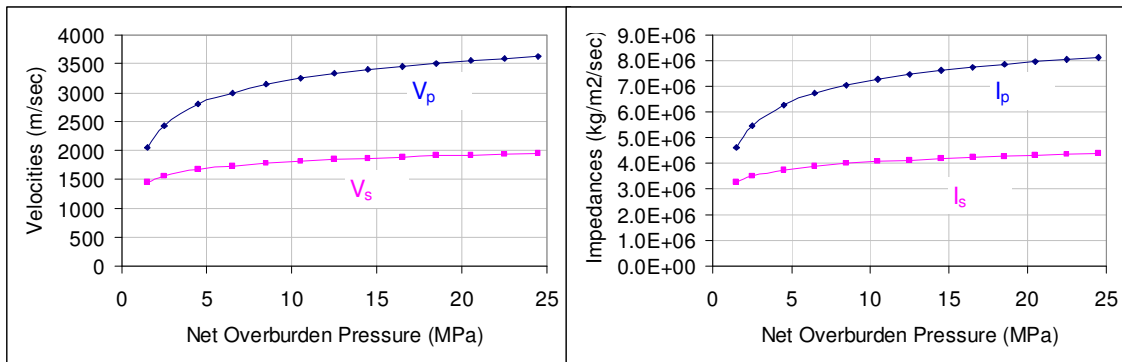


Figure 4.4: Effect of net overburden pressure on P- and S-wave velocities (V_p and V_s) and impedances (I_p and I_s) for the marly section

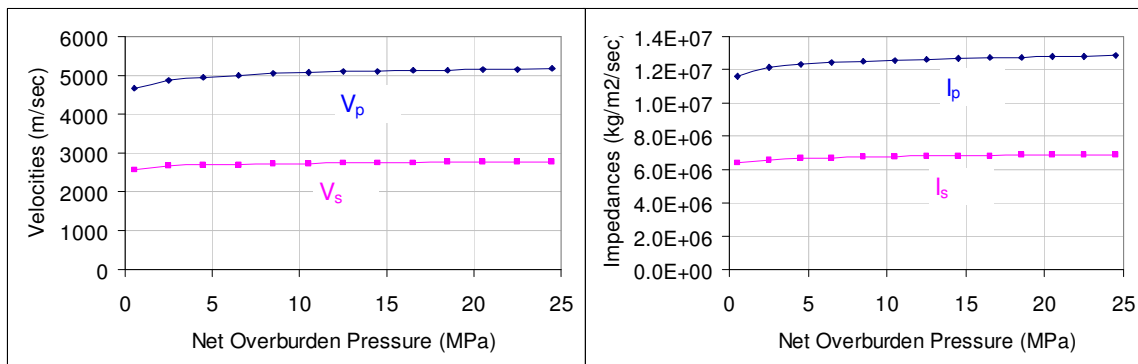


Figure 4.5: Effect of net overburden pressure on P- and S-wave velocities (V_p and V_s) and impedances (I_p and I_s) for the upper vuggy section

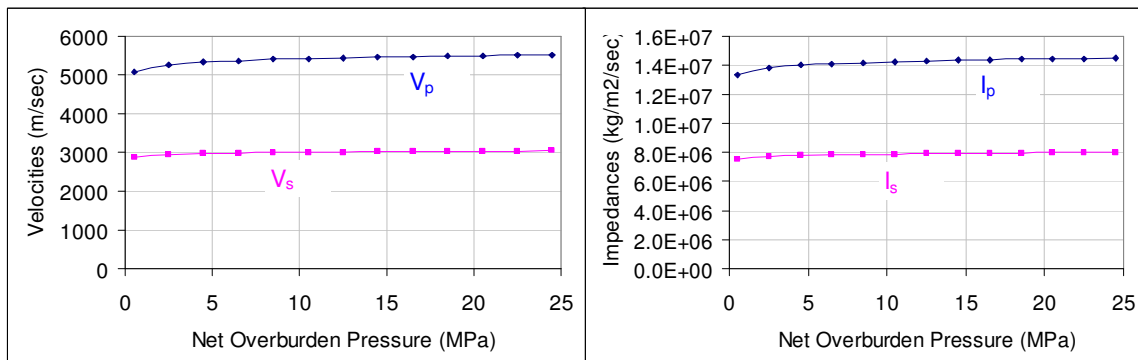


Figure 4.6: Effect of net overburden pressure on P- and S-wave velocities (V_p and V_s) and impedances (I_p and I_s) for the lower vuggy section

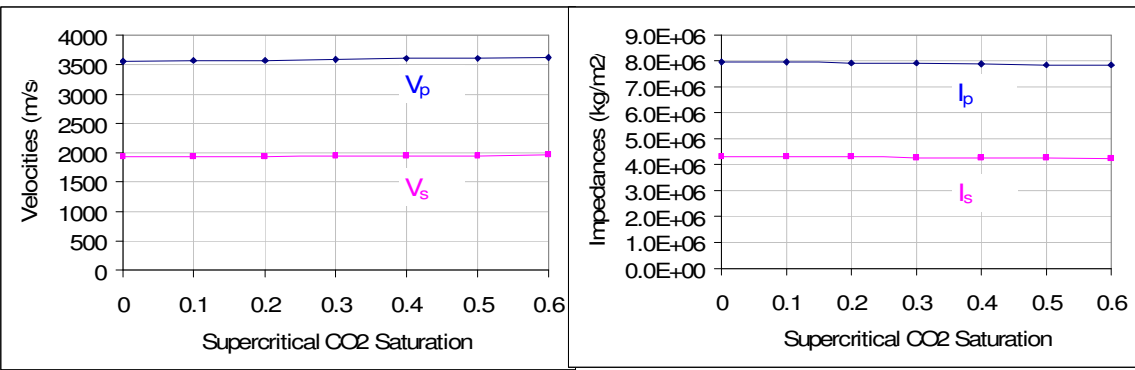


Figure 4.7: Effect of supercritical CO2 saturation on P- and S-wave velocities (V_p and V_s) and impedances (I_p and I_s) for the marly section

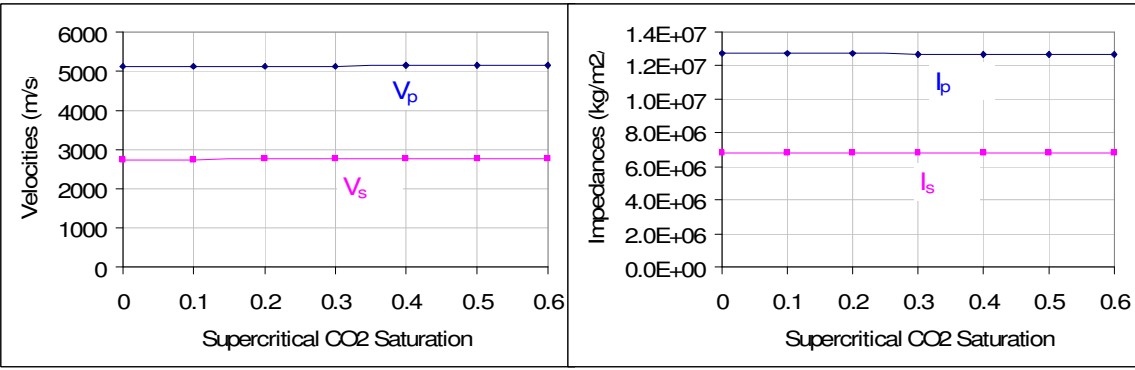


Figure 4.8: Effect of supercritical CO2 saturation on P- and S-wave velocities (V_p and V_s) and impedances (I_p and I_s) for the upper vuggy section

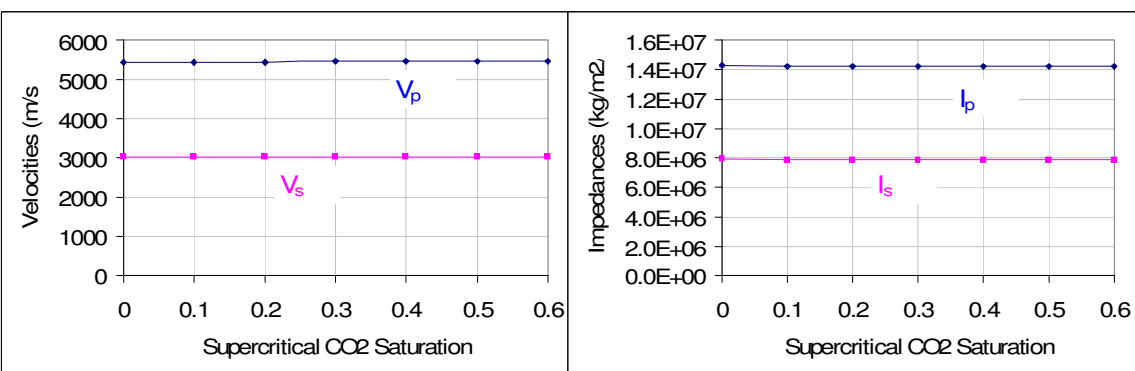


Figure 4.9: Effect of supercritical CO2 saturation on P- and S-wave velocities (V_p and V_s) and impedances (I_p and I_s) for the lower vuggy section

4.2.2 Simulated Velocities and Impedances for Weyburn

The values for various input parameters required for seismic velocity and impedance calculations were extracted from reservoir simulator and fed into the rock-physics model discussed in the previous section. Calculations were performed at two different times, December 2004 and November 2005. Various profiles from the reservoir simulator, such as pressure, saturation, and CO₂ mole fraction, were studied for understanding the simulated dynamics of the reservoir. Profiles for various geologic layers are plotted after averaging parameters across the reservoir model layer using the following equation:

$$X_{av} = \frac{\sum_{i=1}^n h_i \times X_i}{\sum_{i=1}^n h_i}$$

where n is the number of simulation layers in the given geologic layer, h_i is the thickness of simulation layer i , X_i is the parameter value for simulation layer i , and X_{av} is the thickness-averaged value for the parameter. In this study, time-lapse seismic data are not being assimilated for updating reservoir models. Hence, a simple averaging function shown above, instead of quadratic measures, is used.

Thickness-averaged porosity maps for the four geologic sections are shown in Figure 4.10. Permeability and logarithm of permeability for the four geologic sections are

shown in Figure 4.11 and Figure 4.12 respectively. These maps indicate that the porosity and permeability values are correlated for the sections. Figure 4.13 through Figure 4.16 show the pressure profiles at two times slices, November 2005 and December 2004, for the four geologic sections. Dark red zones for upper vuggy (V1) and lower vuggy (V2) sections denote the inactive zones. In these figures, high pressure zones are mostly CO₂ injection points which are confirmed by referencing Figure 4.17 through Figure 4.20. These figures show the CO₂ mole fraction profiles at the two times slices for the four geologic sections. Also, Figure 4.21 through Figure 4.24 show the gas saturation profiles for the four geologic sections. These are the key input parameters which are fed into the seismic velocity and impedance calculations. Next, profiles (or maps) for the calculated seismic parameters for the same two time slices are shown. Figure 4.25 through Figure 4.28 show the P-wave velocity profiles for the four geologic sections, while Figure 4.29 through Figure 4.32 show the P-wave impedance profiles for the same. Compared with the porosity profiles shown in Figure 4.10, it may be concluded that porosity values have maximum impact on the P-wave seismic parameters at any time. Figure 4.33 through Figure 4.36 show the S-wave velocity profiles for the four geologic sections, while Figure 4.37 through Figure 4.40 show the S-wave impedance profiles for the same. Again, porosity has a large impact on the S-wave seismic parameters at any time. Hence, it is concluded that seismic parameters like velocity and impedance are a good indicators of porosity. Figure 4.41 shows the pairwise-scatterplot for the different geologic layers of Weyburn. Porosity and calculated impedance values are strongly correlated, whereas permeability values are

loosely correlated with porosity and calculated impedance values. Figure 4.42 shows the same relationships but for the calculated velocities.

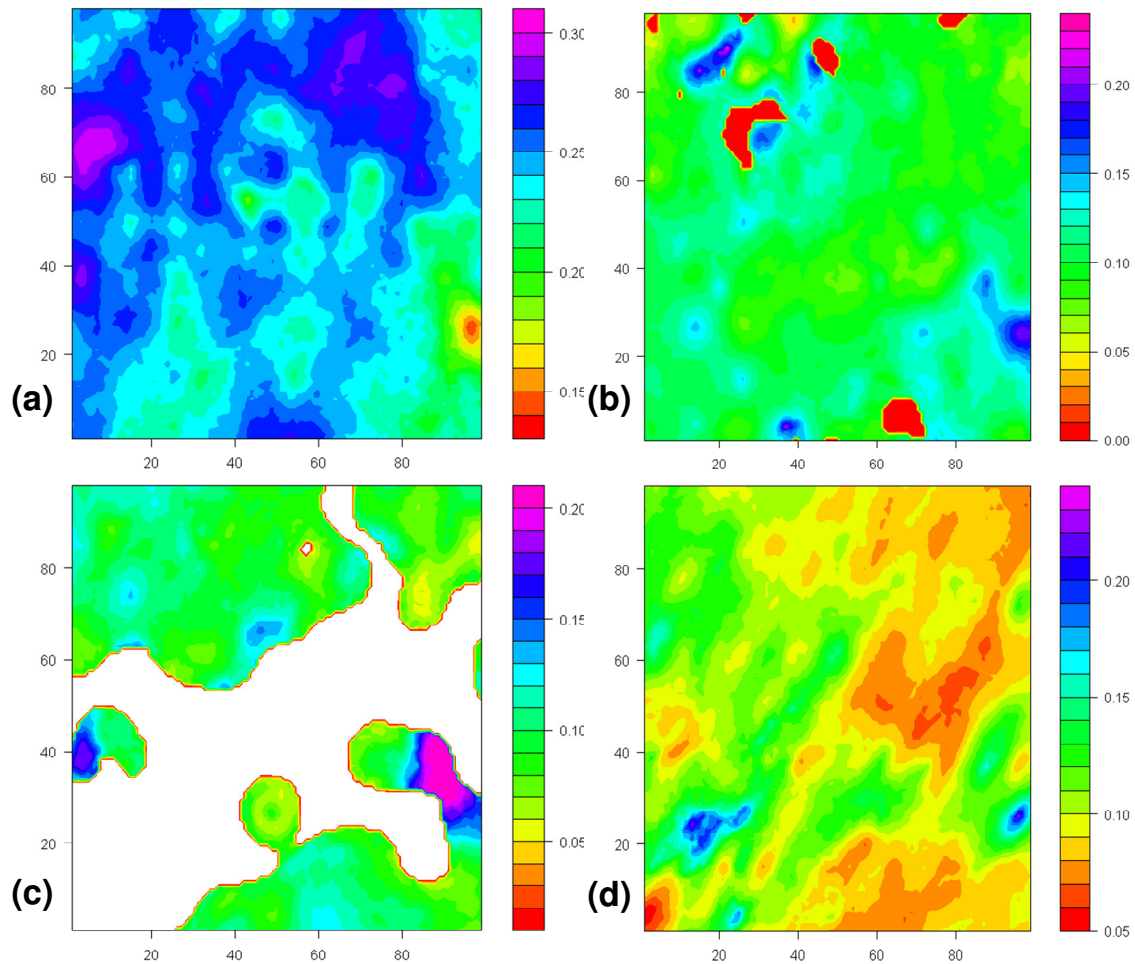


Figure 4.10: Thickness averaged porosity maps for (a) marly, (b) upper vuggy(V1), (c) lower vuggy(V2), and (d) lower vuggy(V4+) sections

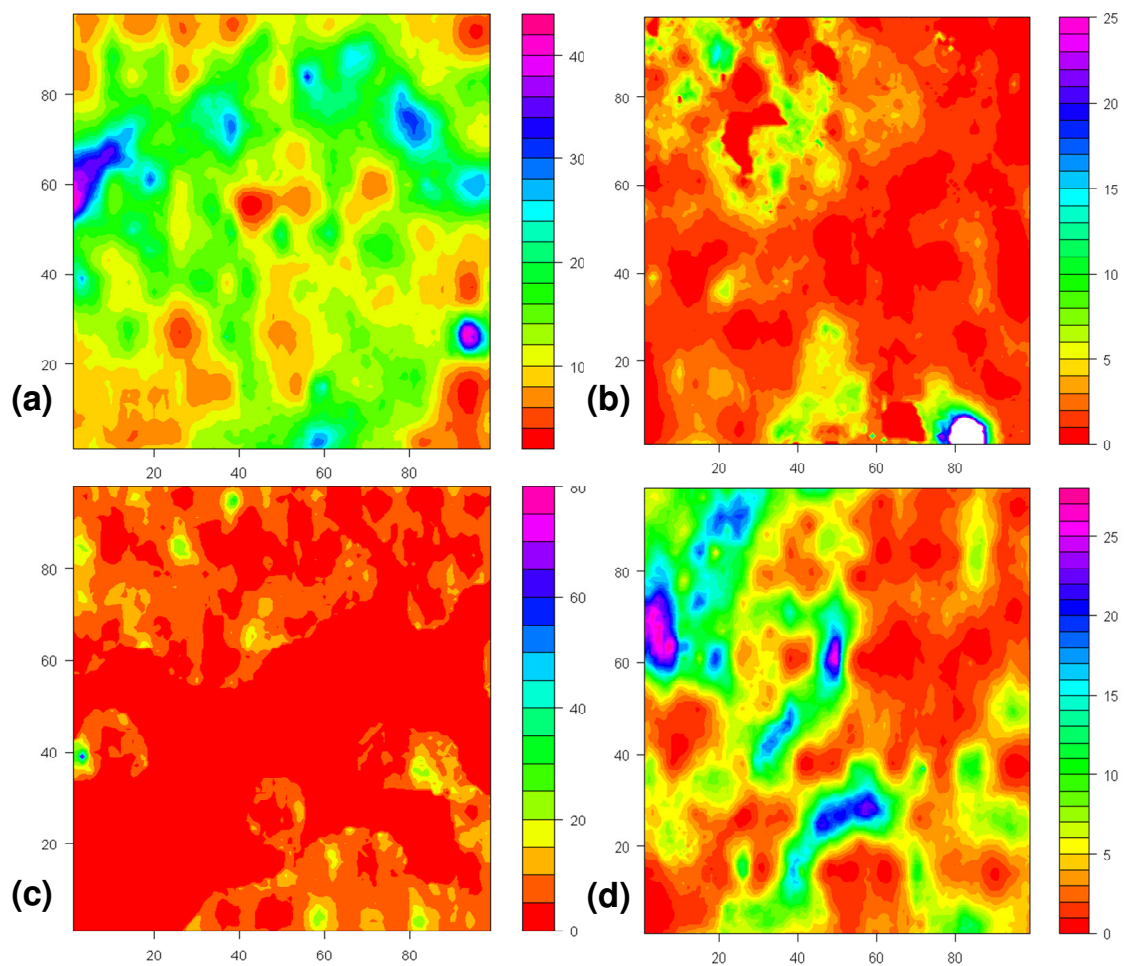


Figure 4.11: Thickness averaged permeability maps for (a) marly, (b) upper vuggy(V1), (c) lower vuggy(V2), and (d) lower vuggy(V4+) sections

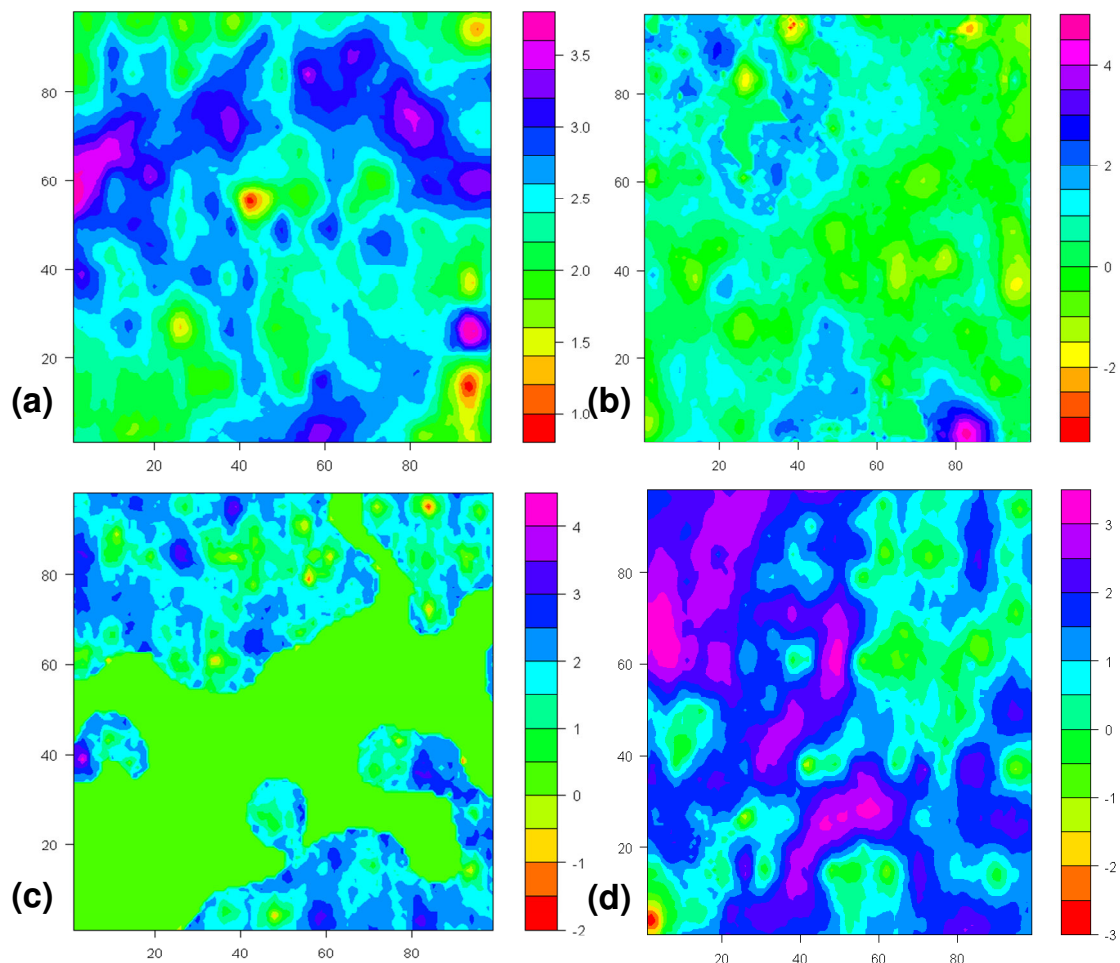


Figure 4.12: Thickness averaged log permeability maps for (a) marly, (b) upper vuggy(V1), (c) lower vuggy(V2), and (d) lower vuggy(V4+) sections

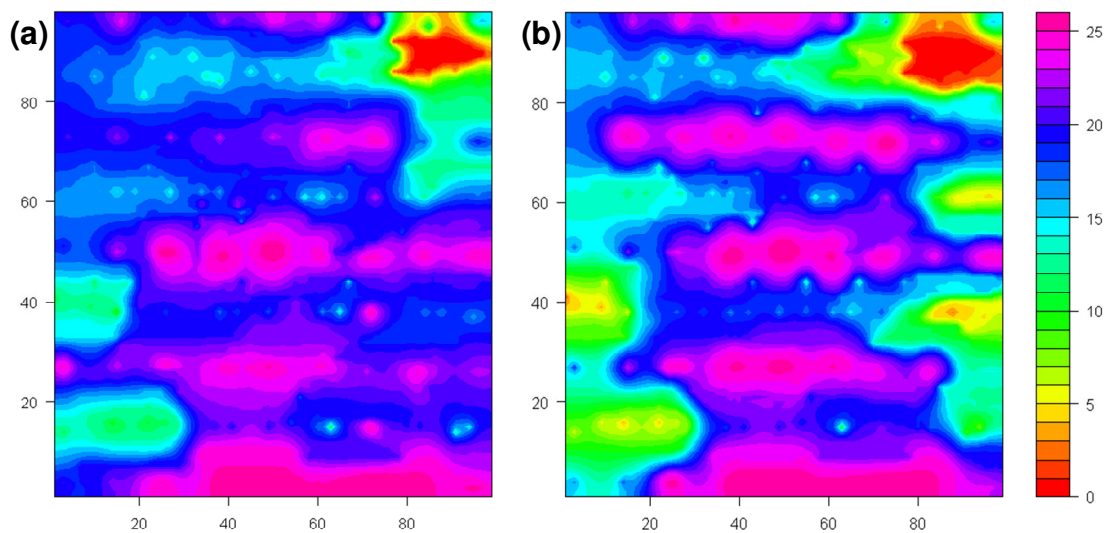


Figure 4.13: Thickness averaged pressure profiles (in MPa) for marly section at times (a) November 2005, and (b) December 2004

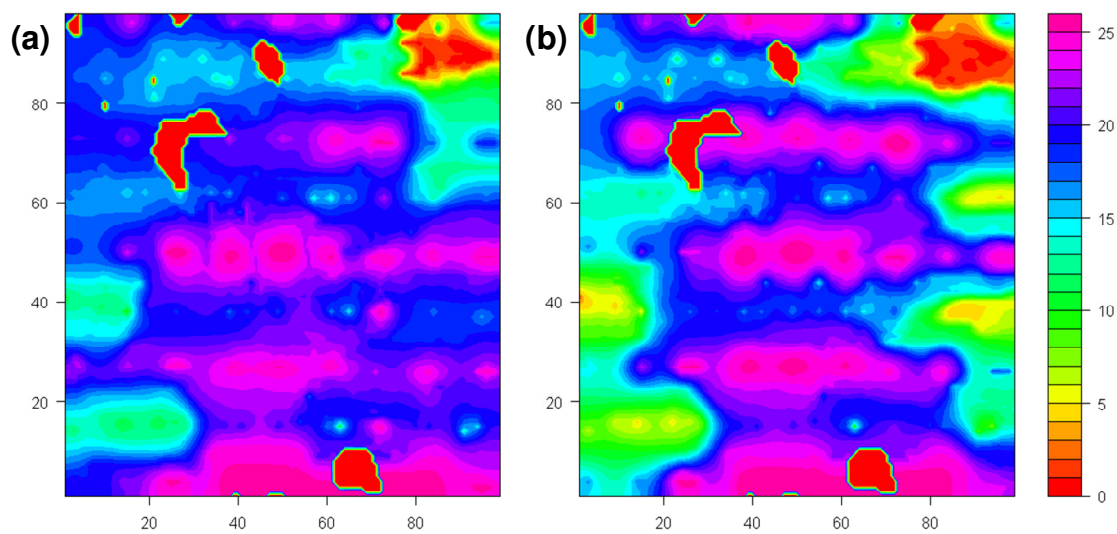


Figure 4.14: Thickness averaged pressure profiles (in MPa) for upper vuggy(V1) section at times (a) November 2005, and (b) December 2004

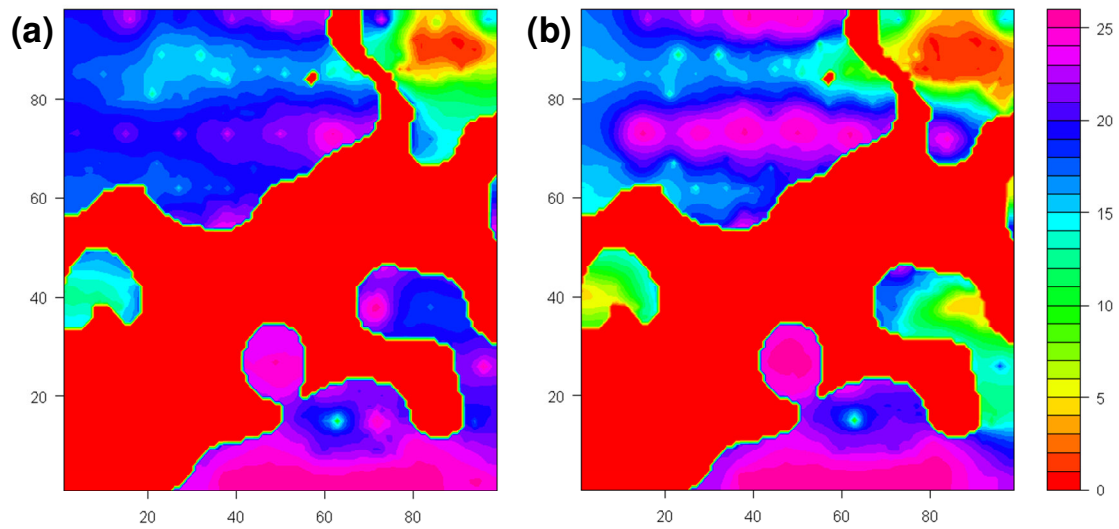


Figure 4.15: Thickness averaged pressure profiles (in MPa) for lower vuggy(V2) section at times (a) November 2005, and (b) December 2004

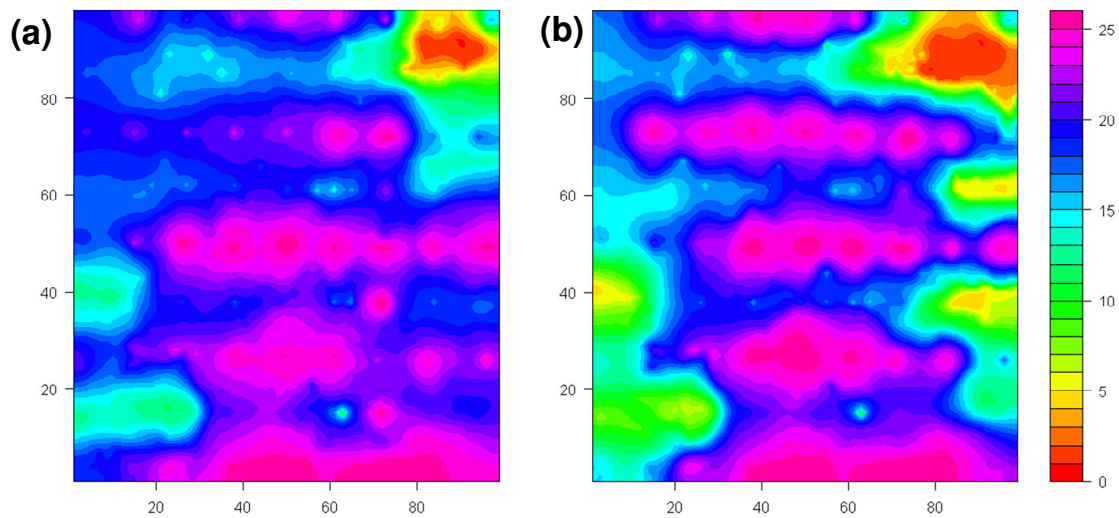


Figure 4.16: Thickness averaged pressure profiles (in MPa) for lower vuggy(V4+) section at times (a) November 2005, and (b) December 2004

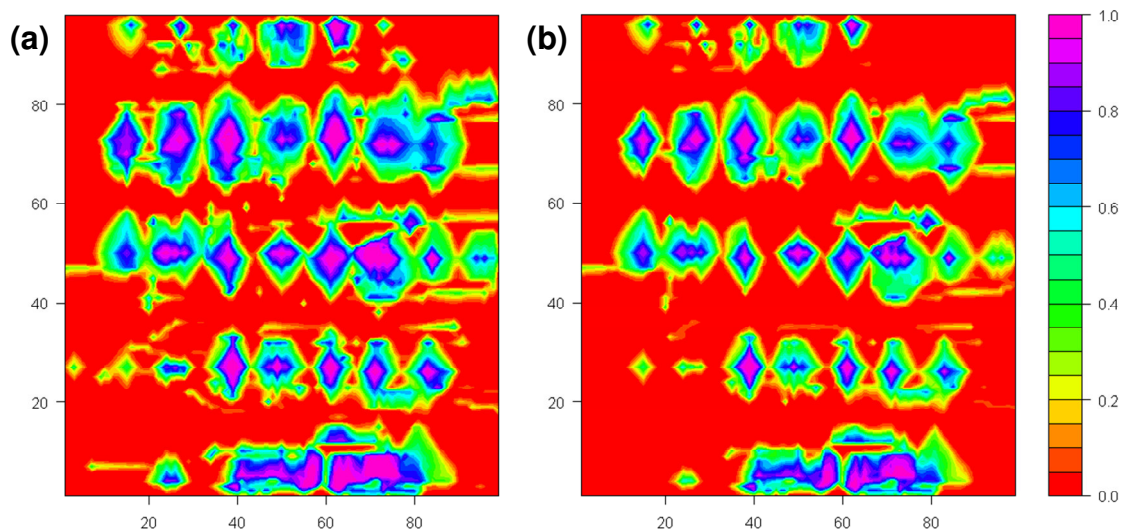


Figure 4.17: Thickness averaged CO₂ mole fraction profiles for marly section at times (a) November 2005, and (b) December 2004

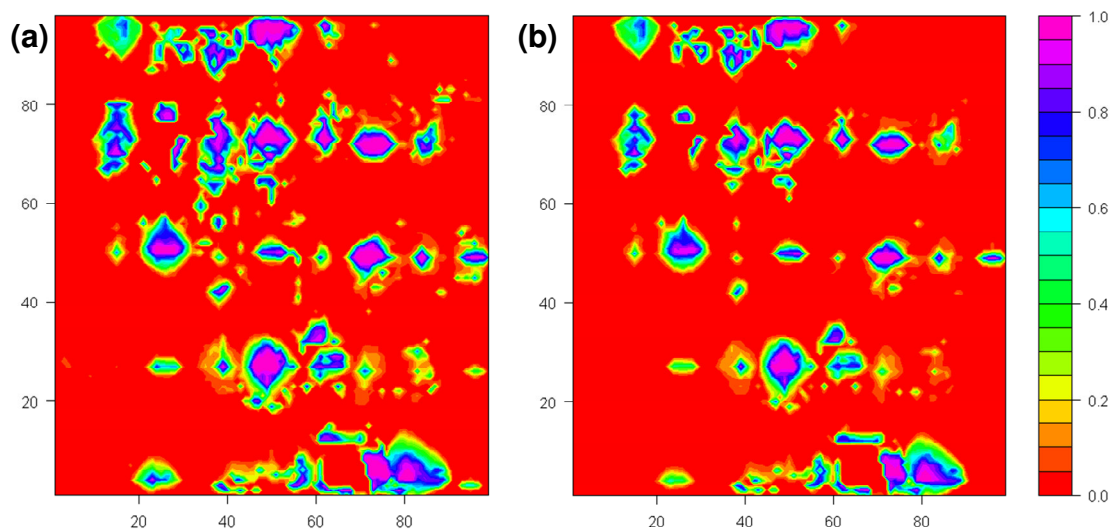


Figure 4.18: Thickness averaged CO₂ mole fraction profiles for upper vuggy (V1) section at times (a) November 2005, and (b) December 2004

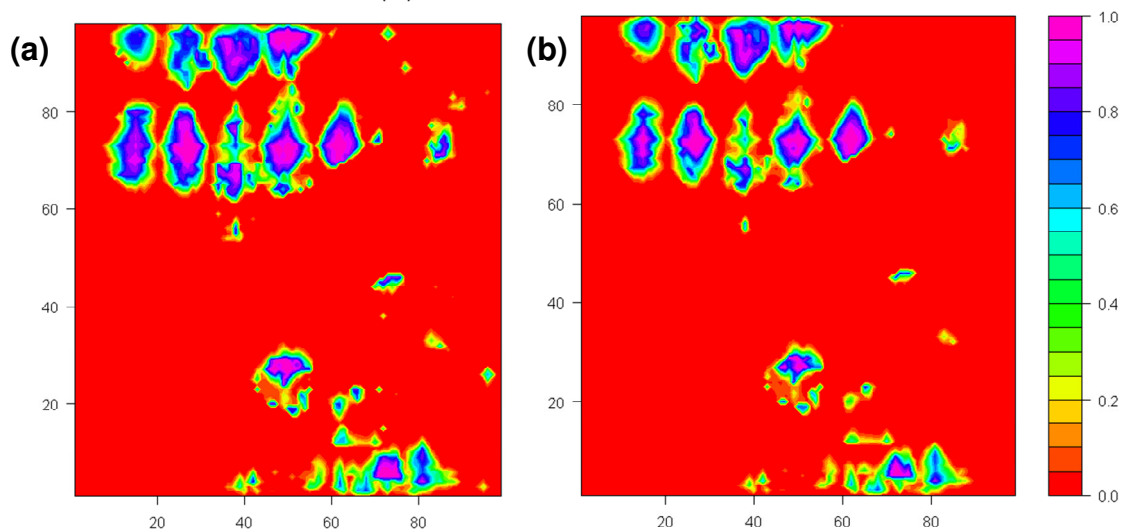


Figure 4.19: Thickness averaged CO₂ mole fraction profiles for lower vuggy(V2) section at times (a) November 2005, and (b) December 2004

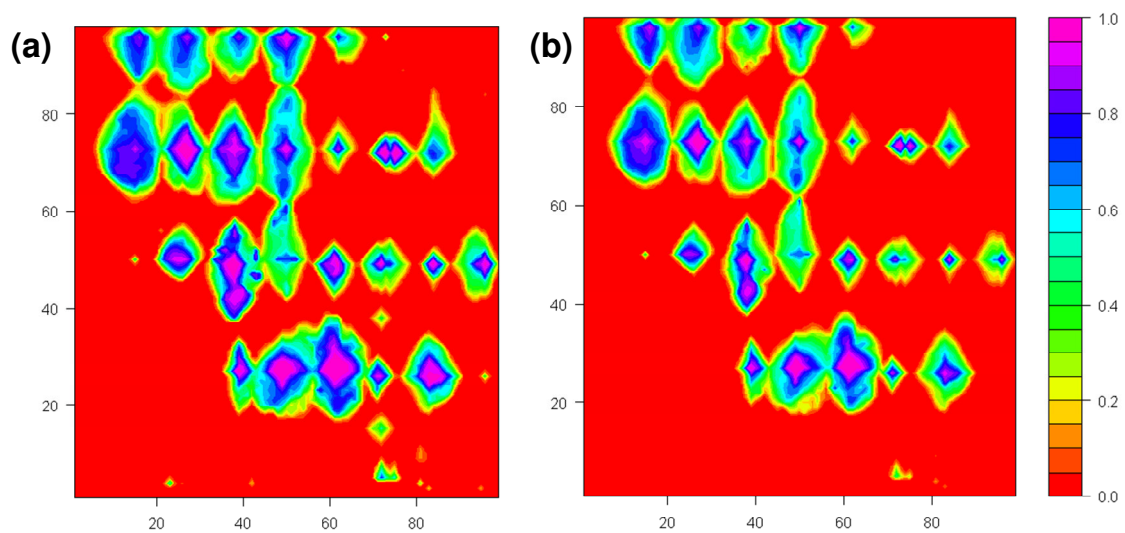


Figure 4.20: Thickness averaged CO₂ mole fraction profiles for lower vuggy(V4+) section at times (a) November 2005, and (b) December 2004

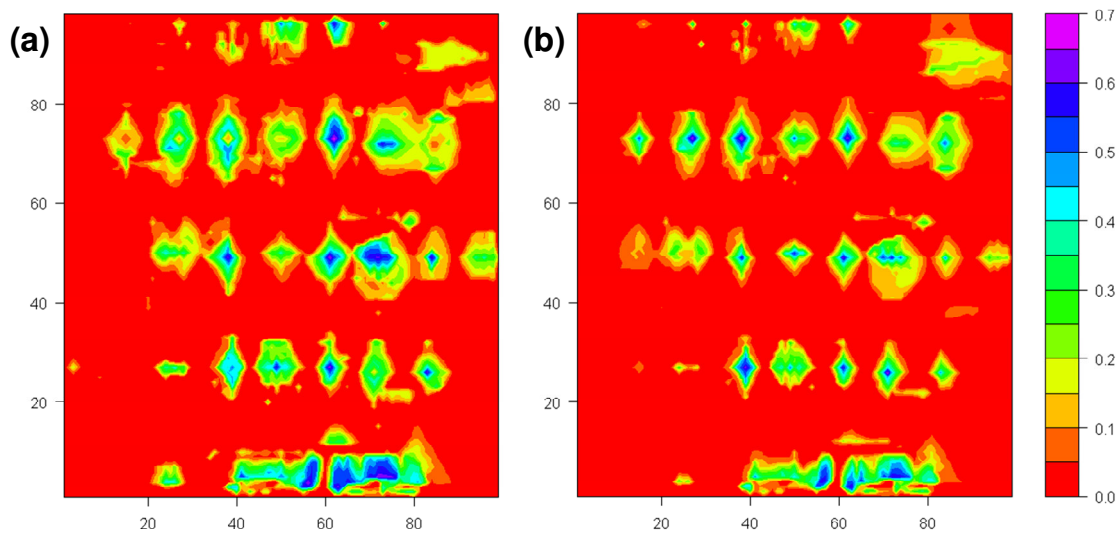


Figure 4.21: Thickness averaged gas saturation profiles for marly section at times (a) November 2005, and (b) December 2004

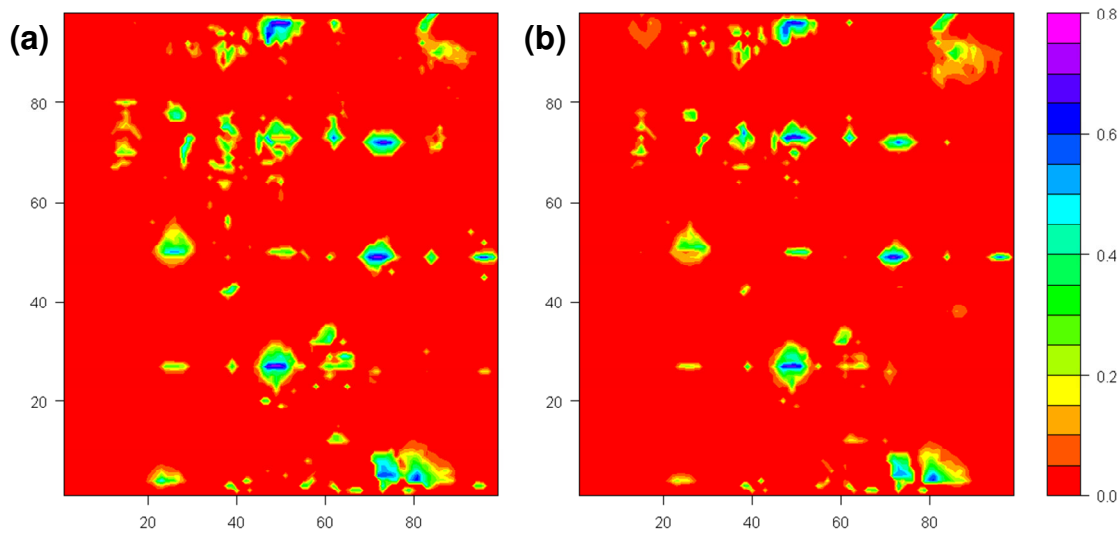


Figure 4.22: Thickness averaged gas saturation profiles for upper vuggy(V1) section at times (a) November 2005, and (b) December 2004

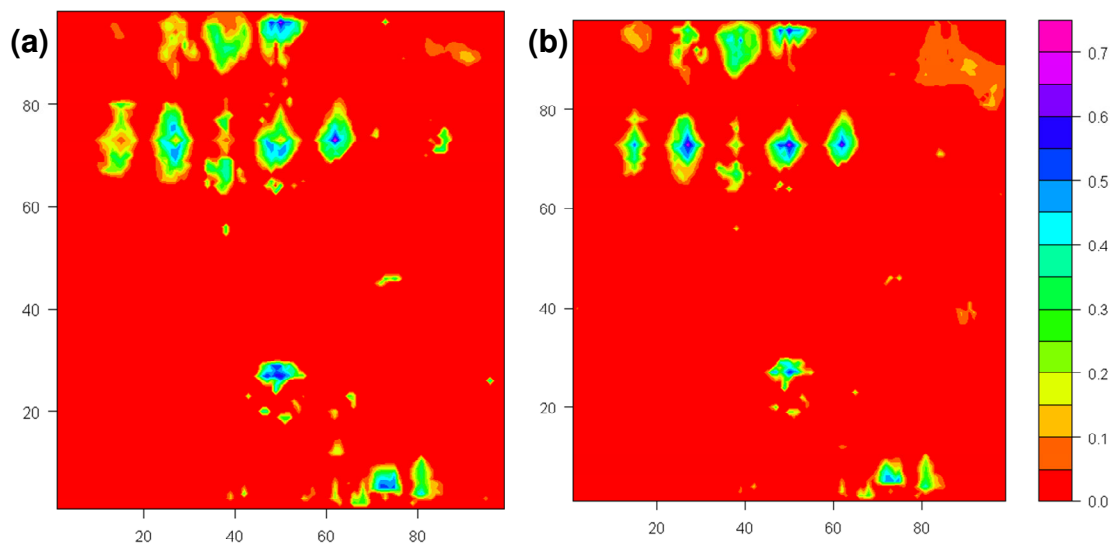


Figure 4.23: Thickness averaged gas saturation profiles for lower vuggy(V2) section at times (a) November 2005, and (b) December 2004

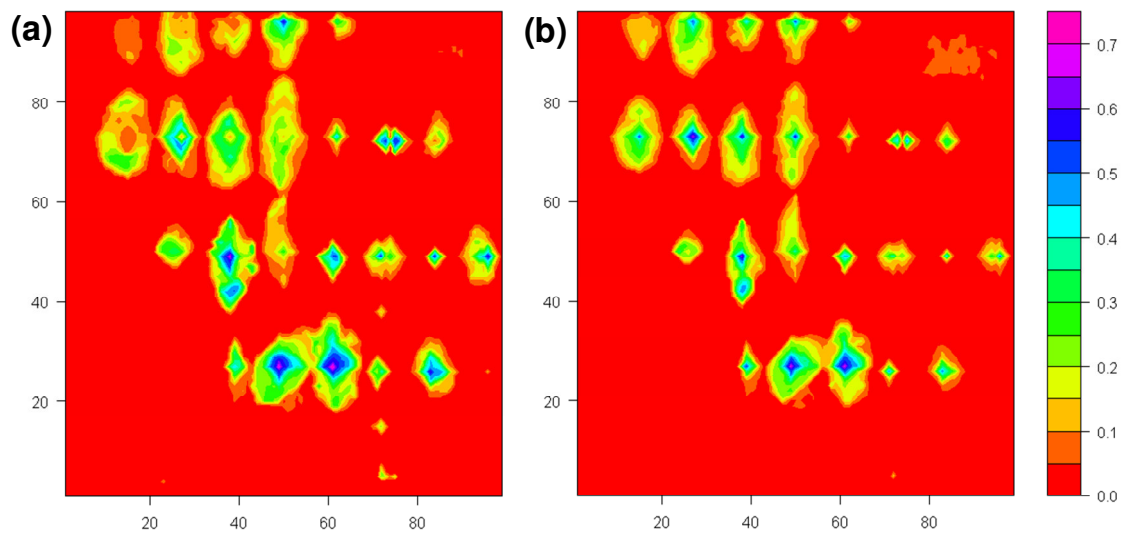


Figure 4.24: Thickness averaged gas saturation profiles for lower vuggy(V4+) section at times (a) November 2005, and (b) December 2004

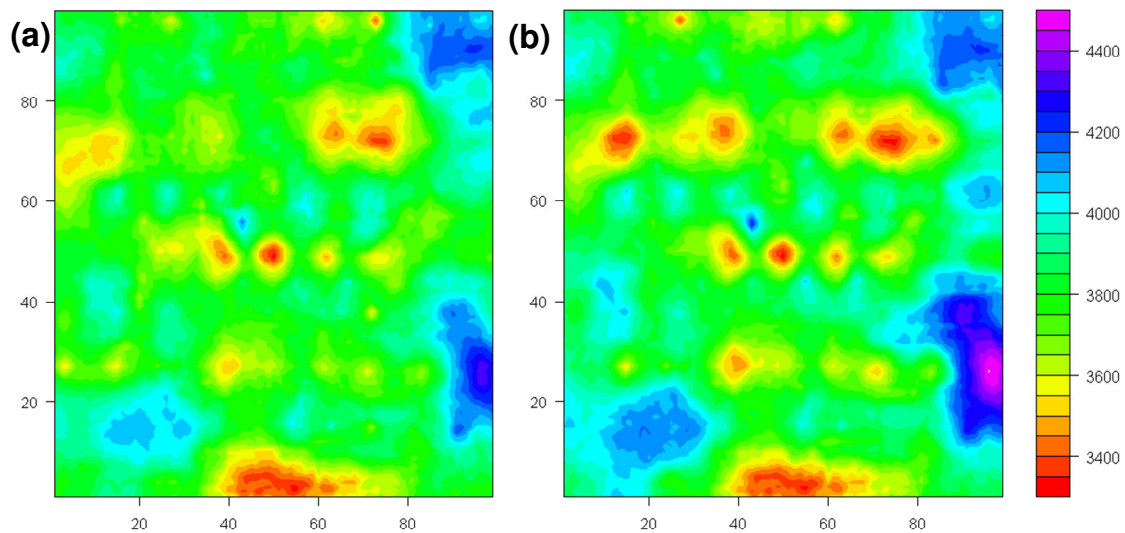


Figure 4.25: Thickness averaged P-wave velocity profiles (in m/sec) for marly section at times (a) November 2005, and (b) December 2004

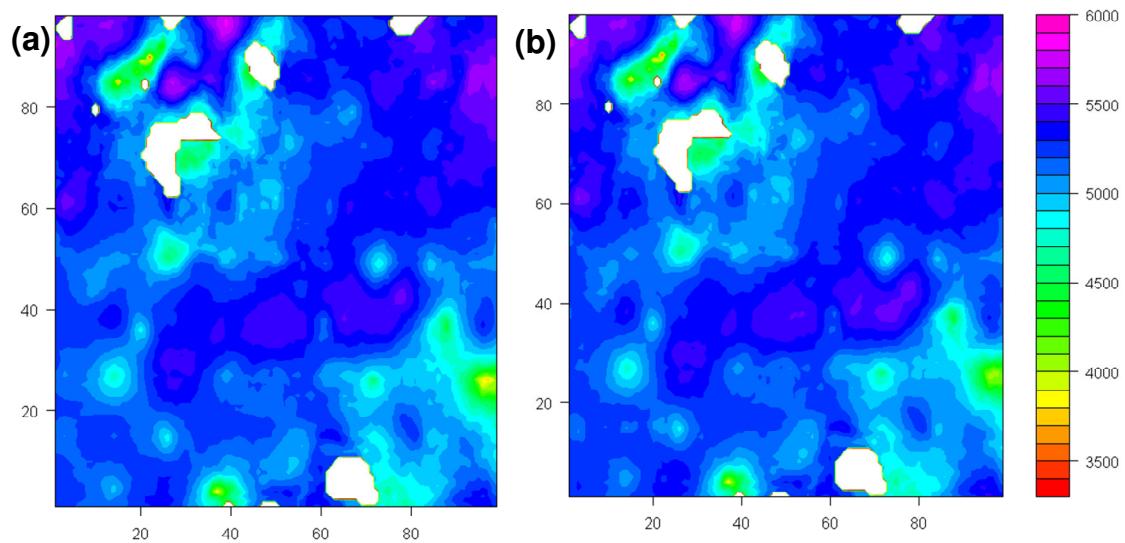


Figure 4.26: Thickness averaged P-wave velocity profiles (in m/sec) for upper vuggy (V1) section at times (a) November 2005, and (b) December 2004

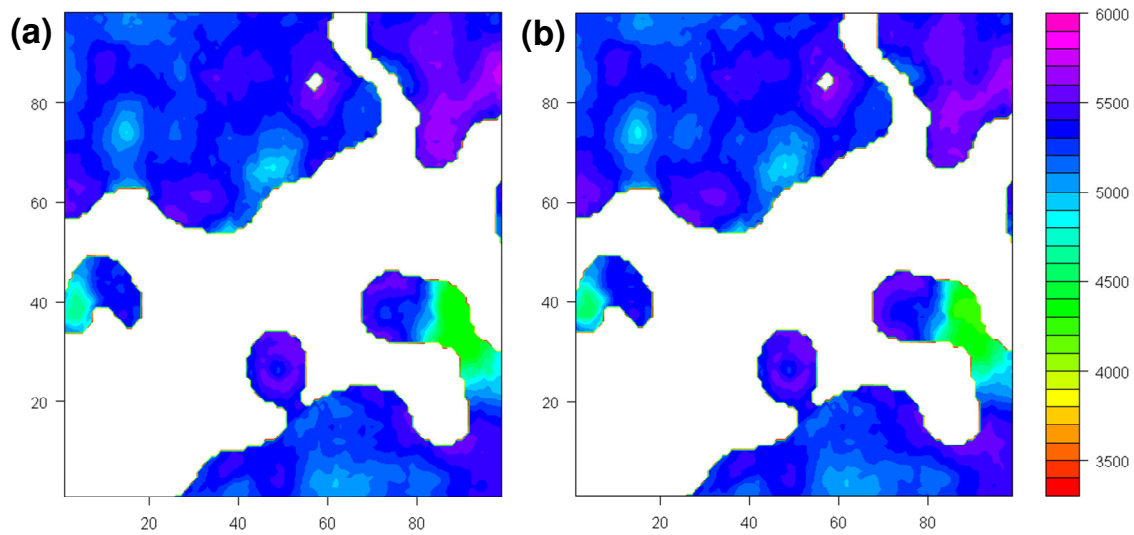


Figure 4.27: Thickness averaged P-wave velocity profiles (in m/sec) for lower vuggy (V2) section at times (a) November 2005, and (b) December 2004

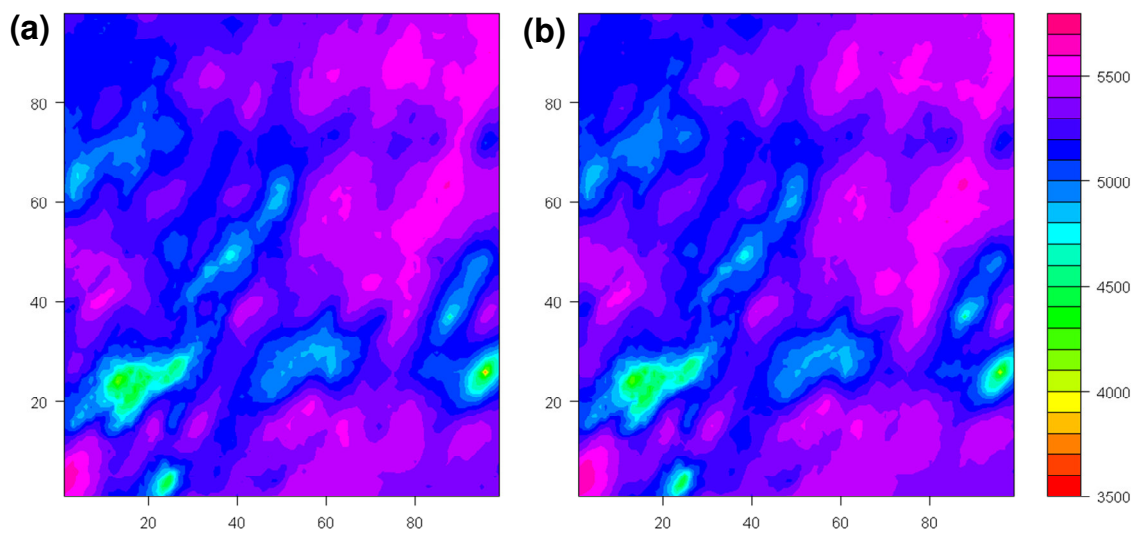


Figure 4.28: Thickness averaged P-wave velocity profiles (in m/sec) for lower vuggy (V4+) section at times (a) November 2005, and (b) December 2004

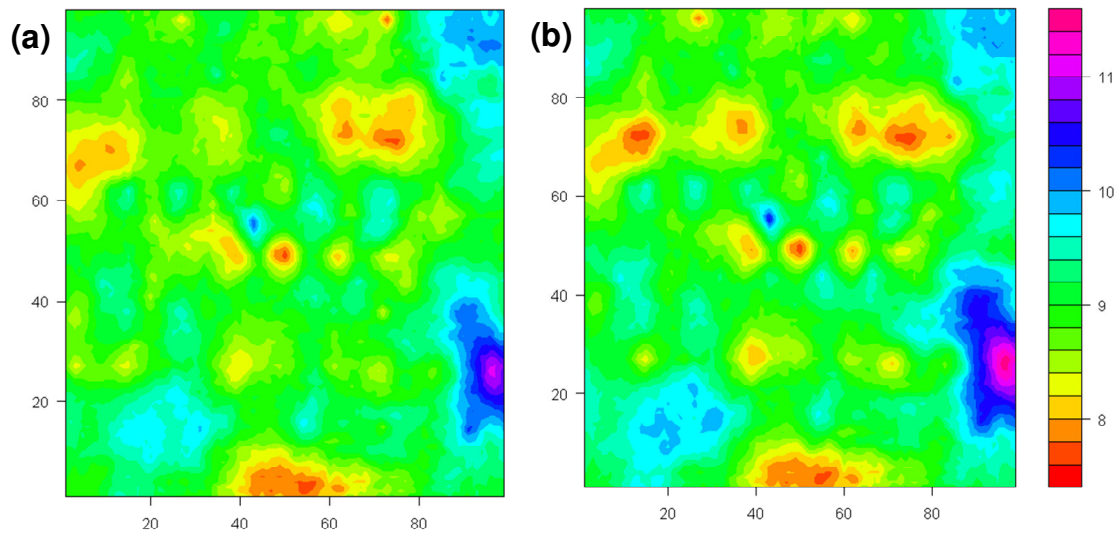


Figure 4.29: Thickness averaged P-wave impedance profiles (in $10^6 \text{ kg/m}^2/\text{sec}$) for marly section at times (a) November 2005, and (b) December 2004

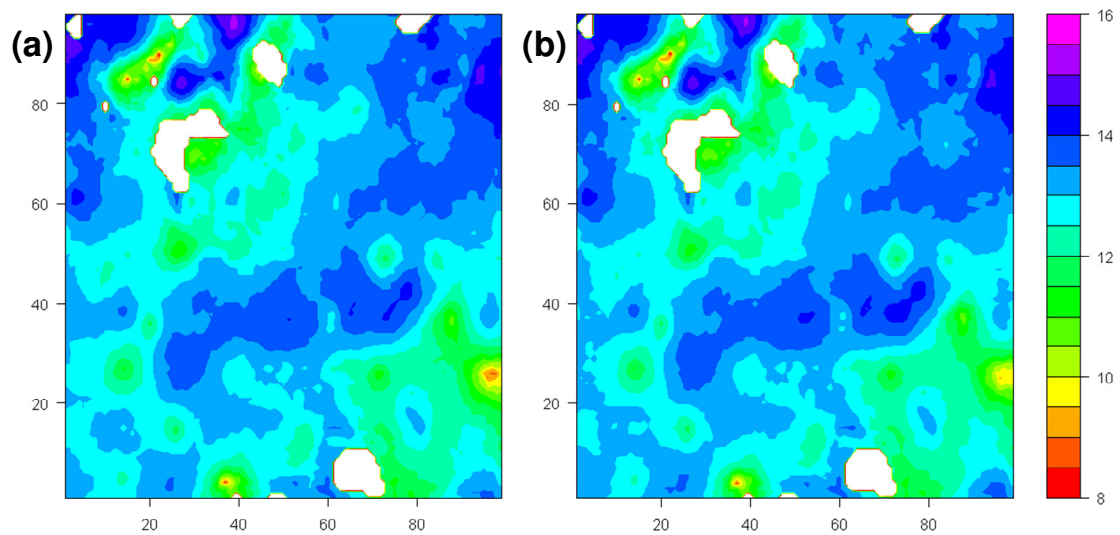


Figure 4.30: Thickness averaged P-wave impedance profiles (in $10^6 \text{ kg/m}^2/\text{sec}$) for upper vuggy (V1) section at times (a) November 2005, and (b) December 2004

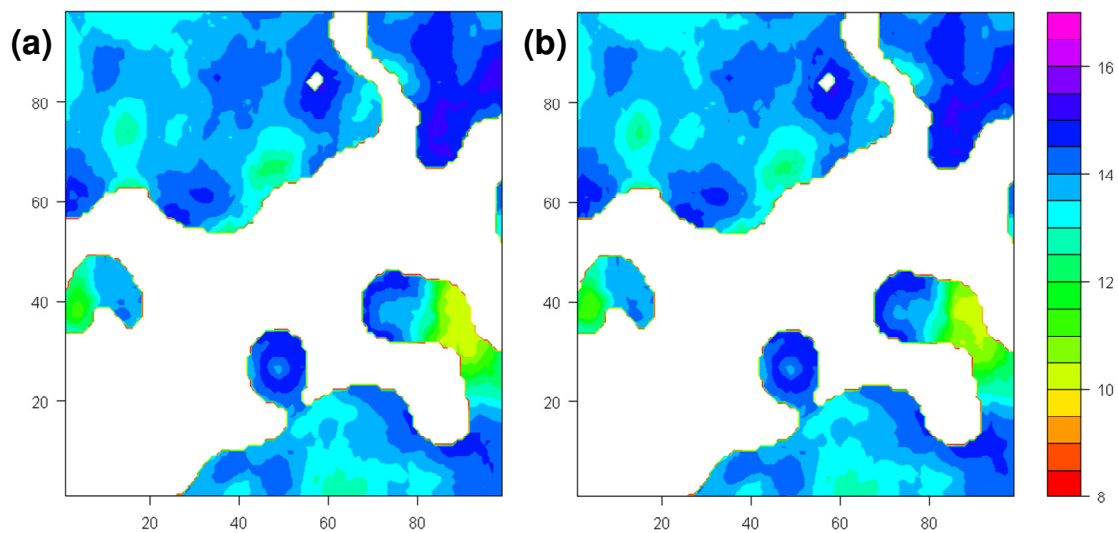


Figure 4.31: Thickness averaged P-wave impedance profiles (in $10^6 \text{ kg/m}^2/\text{sec}$) for lower vuggy(V2) section at times (a) November 2005, and (b) December 2004

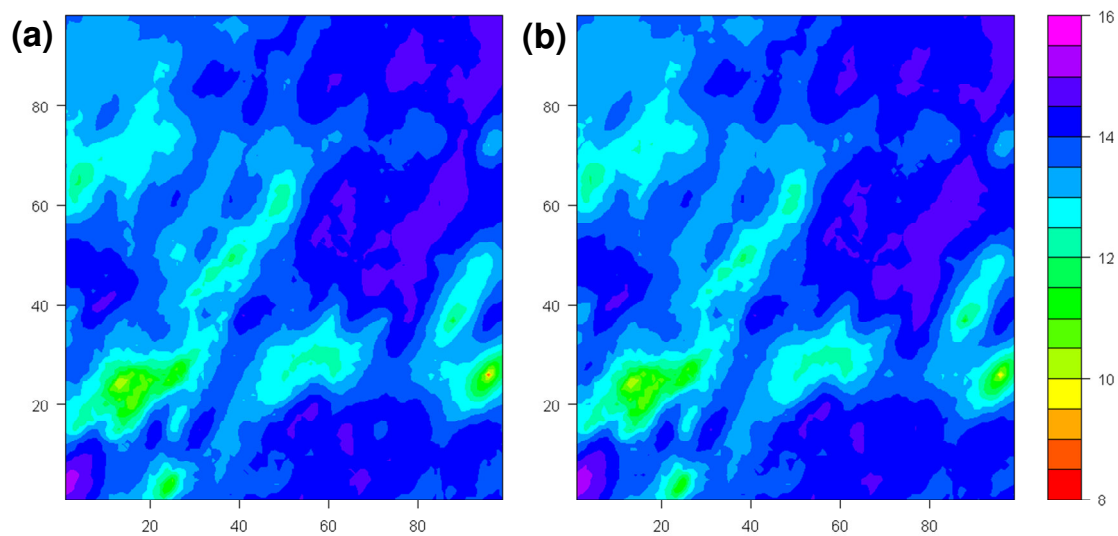


Figure 4.32: Thickness averaged P-wave impedance profiles (in $10^6 \text{ kg/m}^2/\text{sec}$) for lower vuggy(V4+) section at times (a) November 2005, and (b) December 2004

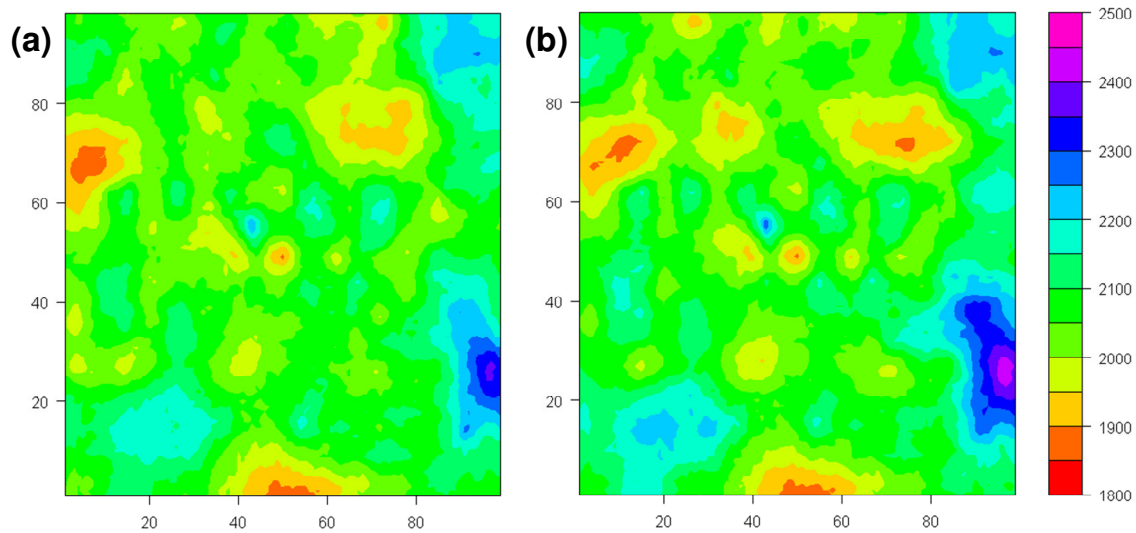


Figure 4.33: Thickness averaged S-wave velocity profiles (in m/sec) for marly section at times (a) November 2005, and (b) December 2004

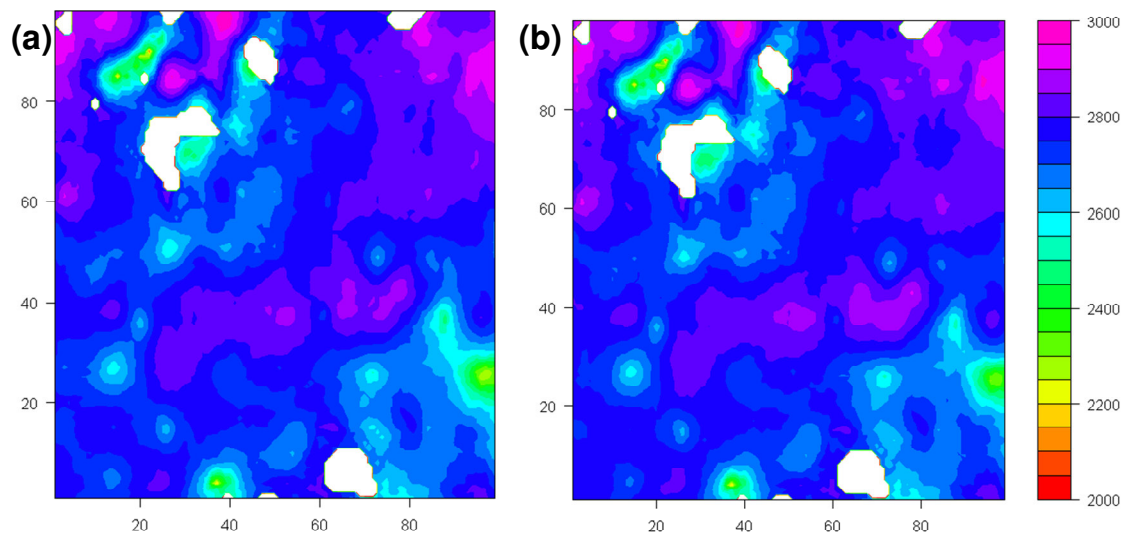


Figure 4.34: Thickness averaged S-wave velocity profiles (in m/sec) for upper vuggy (V1) section at times (a) November 2005, and (b) December 2004

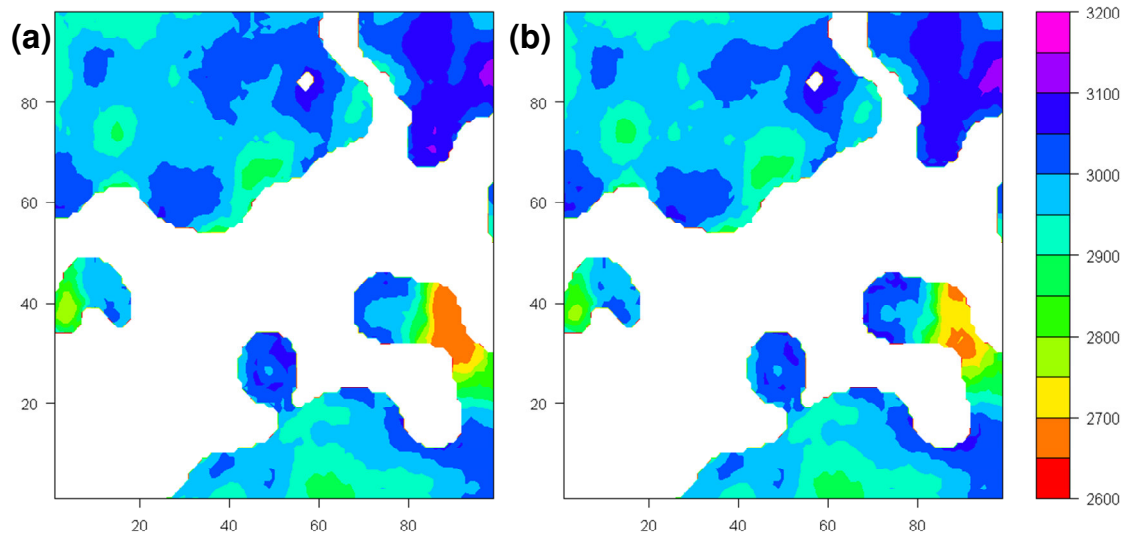


Figure 4.35: Thickness averaged S-wave velocity profiles (in m/sec) for lower vuggy (V2) section at times (a) November 2005, and (b) December 2004

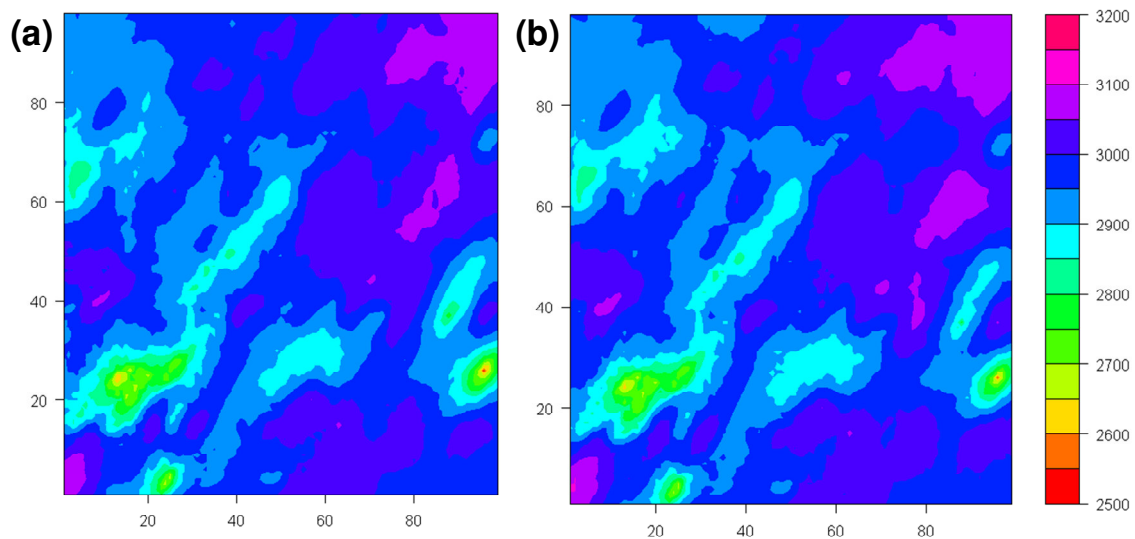


Figure 4.36: Thickness averaged S-wave velocity profiles (in m/sec) for lower vuggy (V4+) section at times (a) November 2005, and (b) December 2004

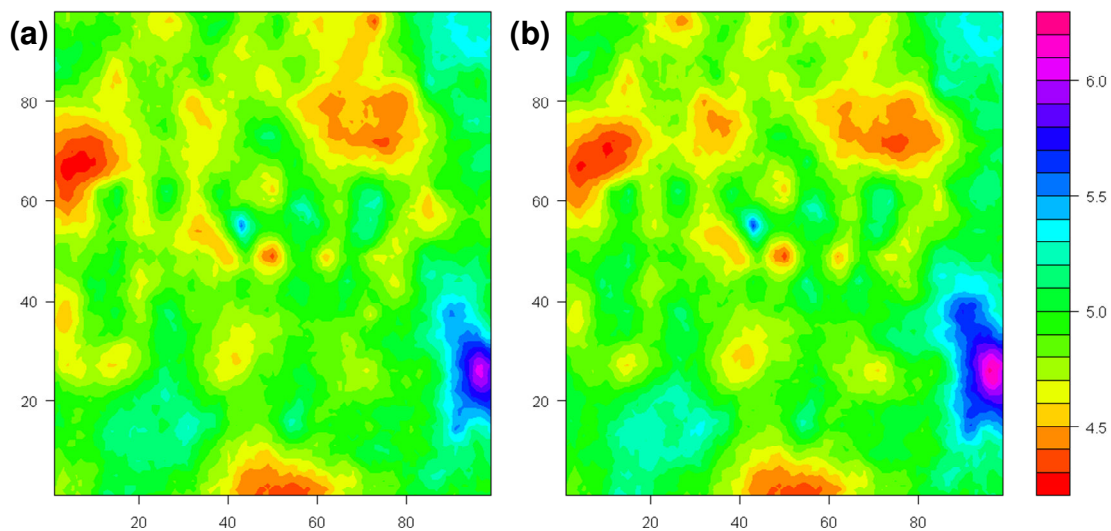


Figure 4.37: Thickness averaged S-wave impedance profiles (in $10^6 \text{ kg/m}^2/\text{sec}$) for marly section at times (a) November 2005, and (b) December 2004

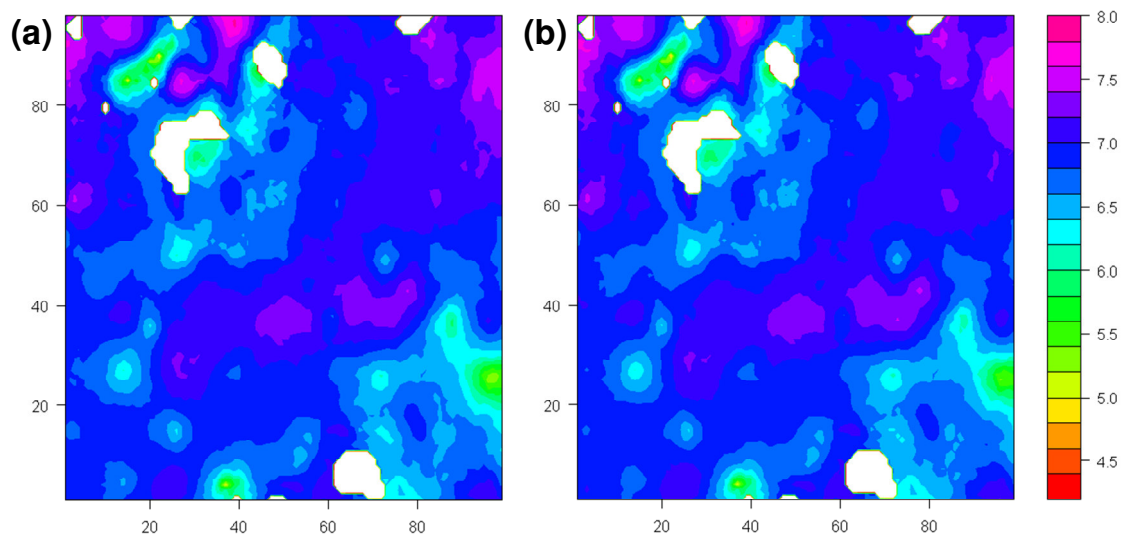


Figure 4.38: Thickness averaged S-wave impedance profiles (in $10^6 \text{ kg/m}^2/\text{sec}$) for upper vuggy (V1) section at times (a) November 2005, and (b) December 2004

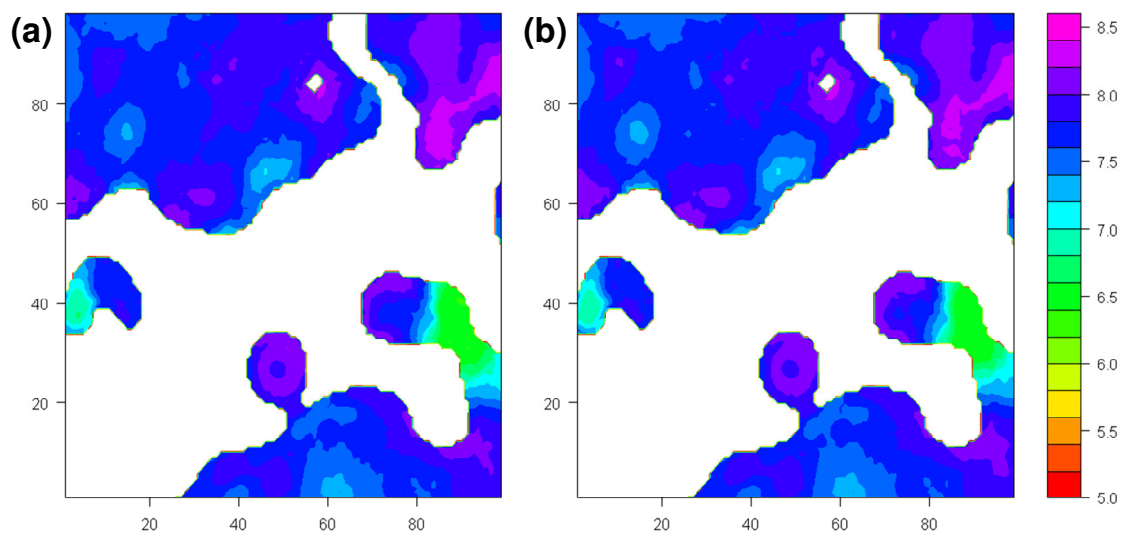


Figure 4.39: Thickness averaged S-wave impedance profiles (in $10^6 \text{ kg/m}^2/\text{sec}$) for lower vuggy (V2) section at times (a) November 2005, and (b) December 2004

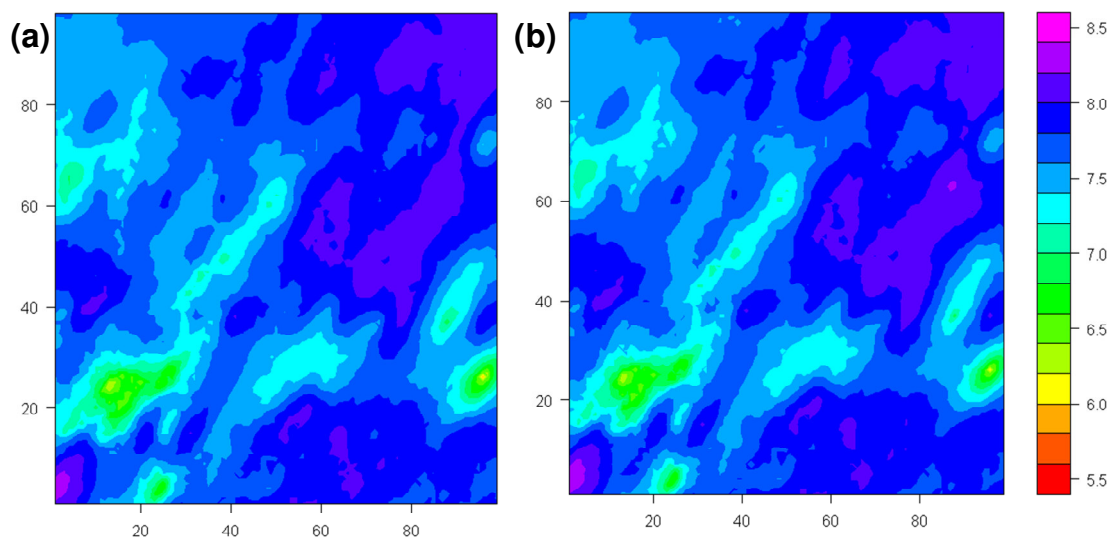


Figure 4.40: Thickness averaged S-wave impedance profiles (in $10^6 \text{ kg/m}^2/\text{sec}$) for lower vuggy (V4+) section at times (a) November 2005, and (b) December 2004

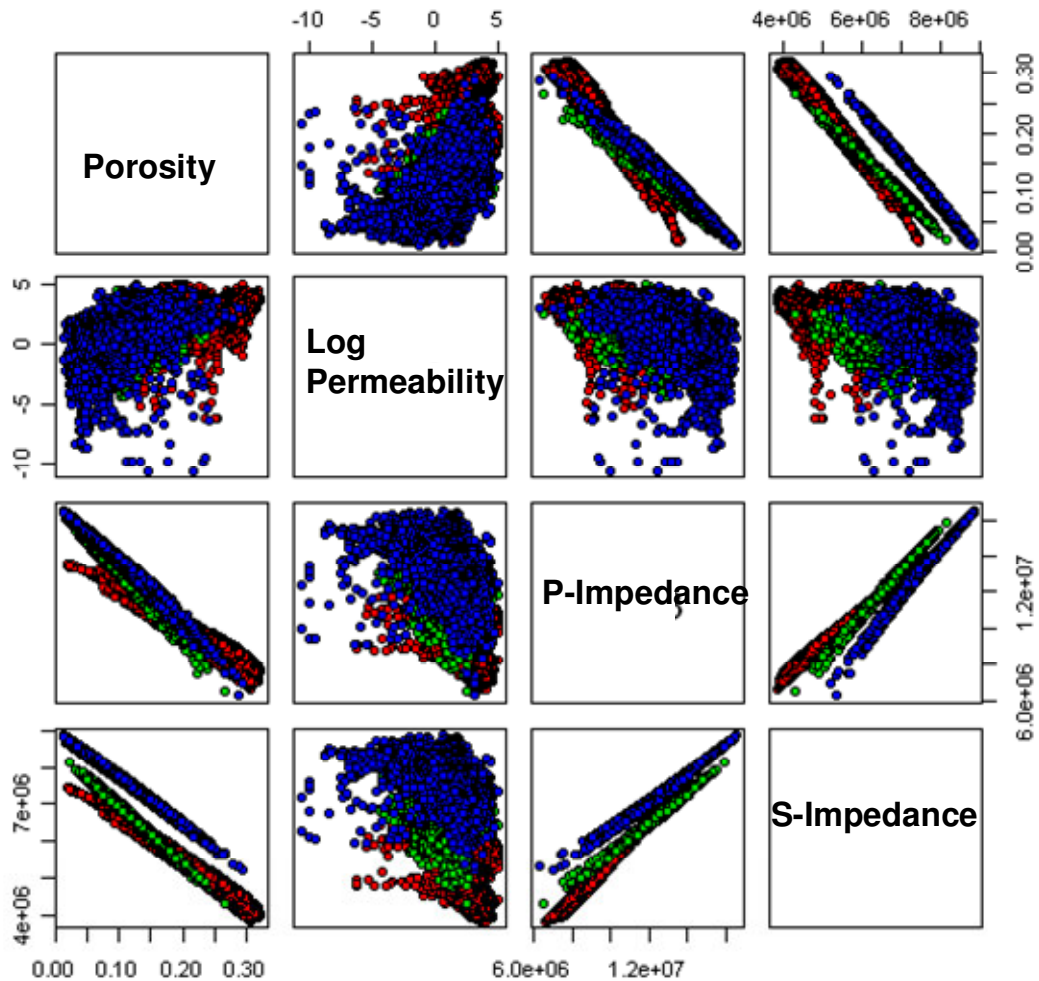


Figure 4.41: Scatterplot showing relationship between simulated impedance values and flow parameters for Weyburn field. (marly in red, upper vuggy in green, and lower vuggy in blue)

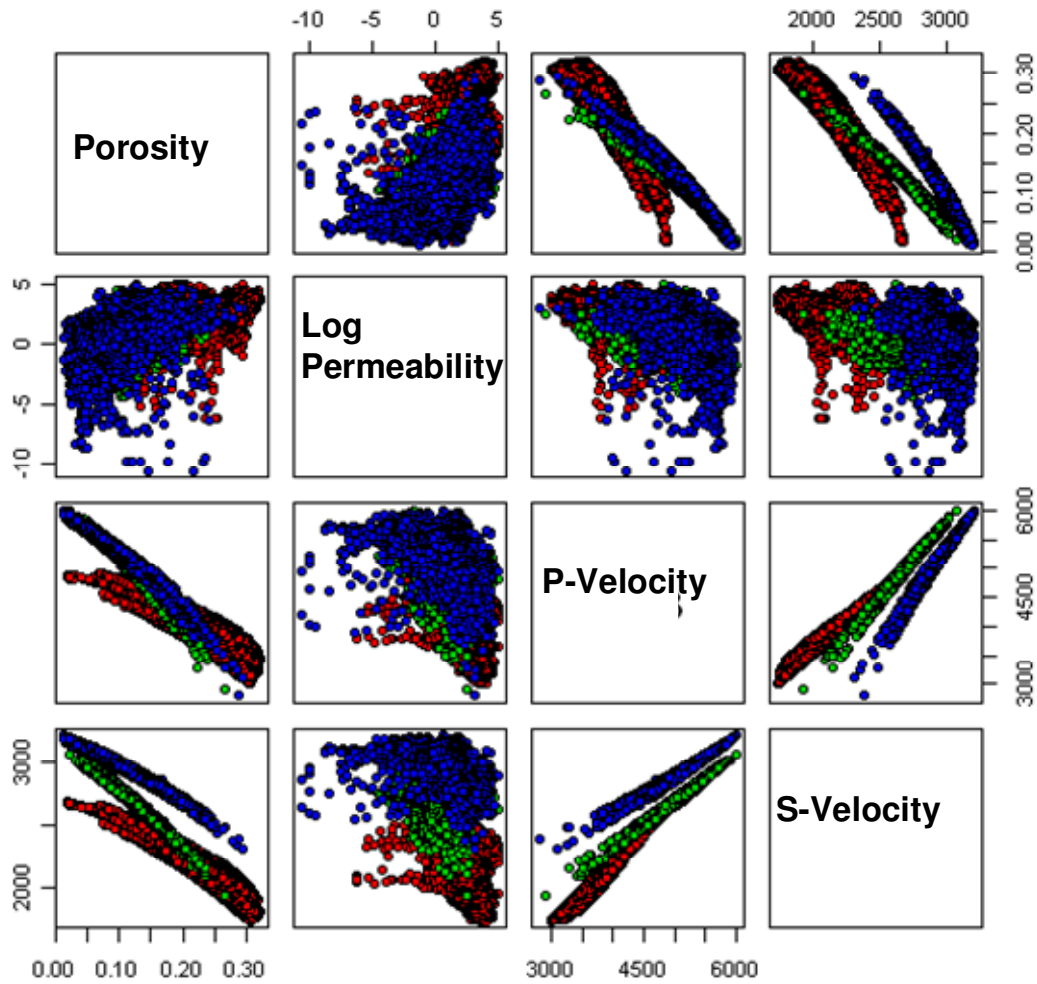


Figure 4.42: Scatterplot showing relationship between simulated velocity values and flow parameters for Weyburn field. (marly in red, upper vuggy in green, and lower vuggy in blue)

4.2.3 Time-lapse Velocities and Impedances for Weyburn

In this section, differences in the calculated seismic velocities and impedances for the two time slices are studied to understand the impact of changes in dynamic parameters on seismic response. Figure 4.43 shows the thickness-averaged changes in pore-pressure values for the four geologic sections. Also, Figure 4.44 and Figure 4.45 show

the thickness-averaged changes in CO₂ mole fractions and gas saturations, respectively, upon CO₂ injection. For all the three parameters i.e., pore-pressure, CO₂ mole fraction, and gas saturation, maps show changes near the CO₂ injection wells. As most of the CO₂ injection occurs in top marly and bottom vuggy (V4+) layers, more changes are seen for these two layers. Figure 4.46 and Figure 4.47 show the thickness-averaged changes in P-wave velocities and impedances, respectively, for the four geologic sections. Maps show larger changes in seismic attributes for top marly and bottom vuggy (V4+) layers. This is in accordance with the changes seen for dynamic parameters. Figure 4.48 and Figure 4.49 show the thickness averaged changes in S-wave velocities and impedances, respectively, for the four geologic sections. Again, maps show larger changes in seismic attributes for top marly and bottom vuggy (V4+) layers. Figure 4.50 and Figure 4.51 show the pairwise-scatterplot for the simulated time-lapse flow parameters and the simulated time-lapse P- and S-wave parameters respectively. Time-lapse pressure changes show larger correlation with time-lapse impedance and velocity changes as compared with that for supercritical CO₂.

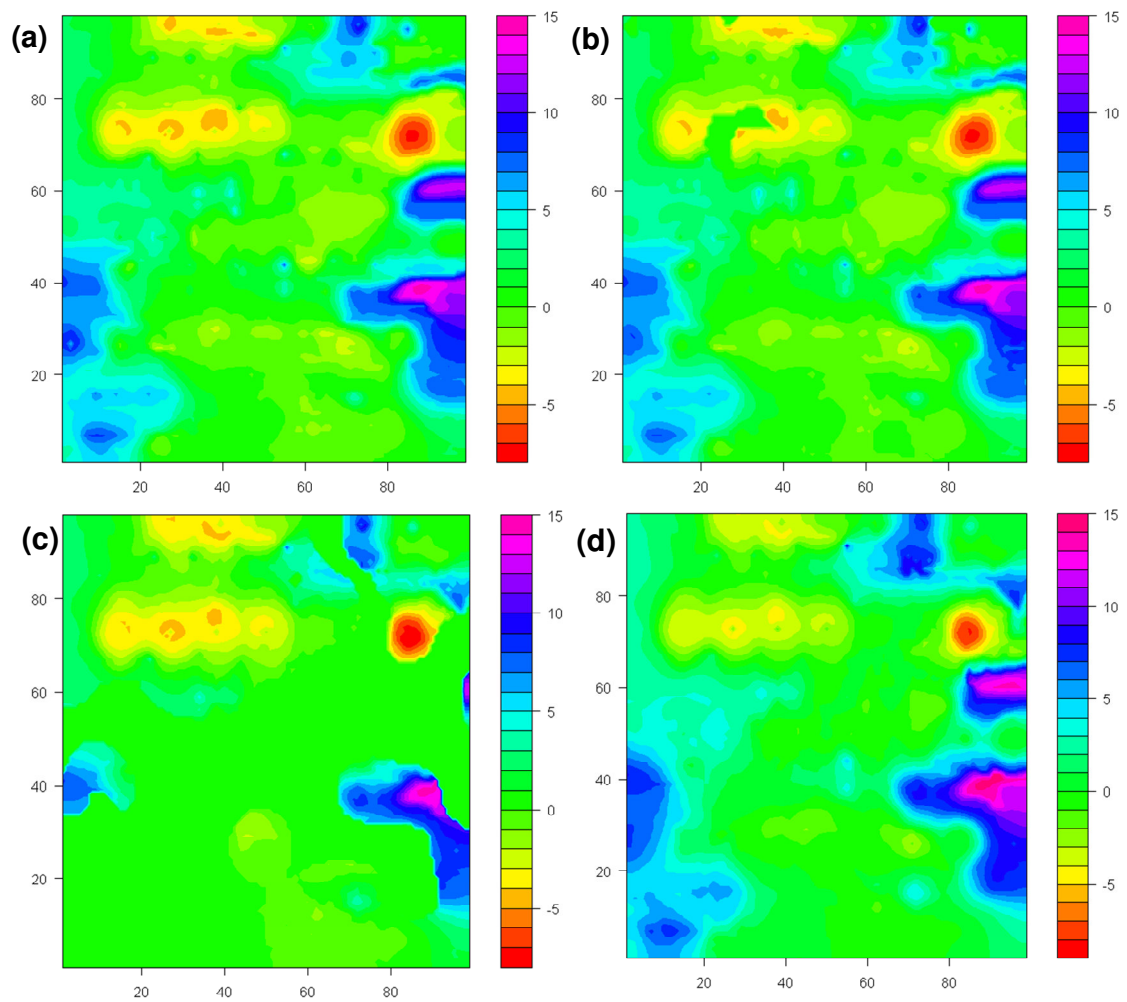


Figure 4.43: Thickness averaged pressure difference maps in MPa for (a) marly, (b) upper vuggy(V1), (c) lower vuggy(V2), and (d) lower vuggy(V4+) sections

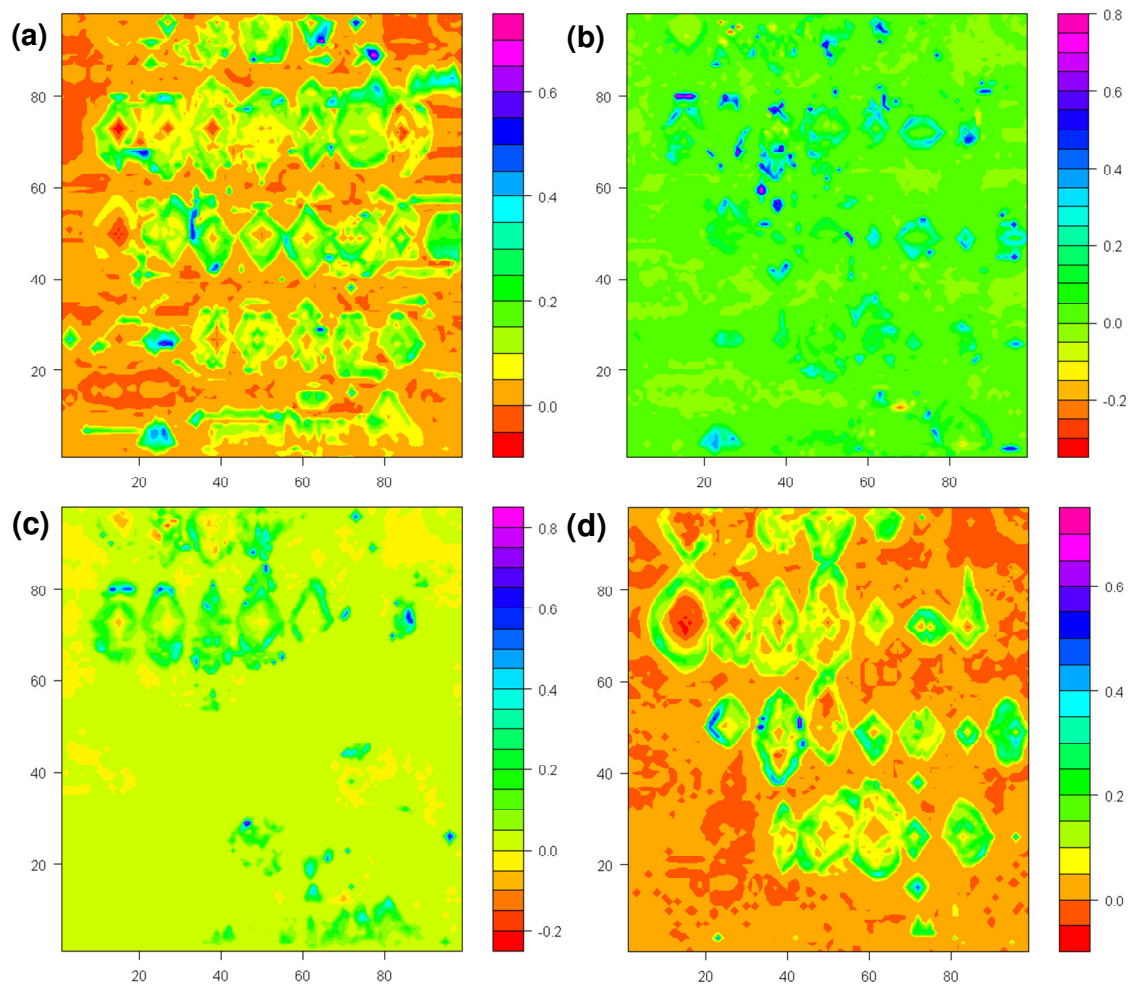


Figure 4.44: Thickness averaged CO₂ mole fraction difference maps for (a) marly, (b) upper vuggy(V1), (c) lower vuggy(V2), and (d) lower vuggy(V4+) sections

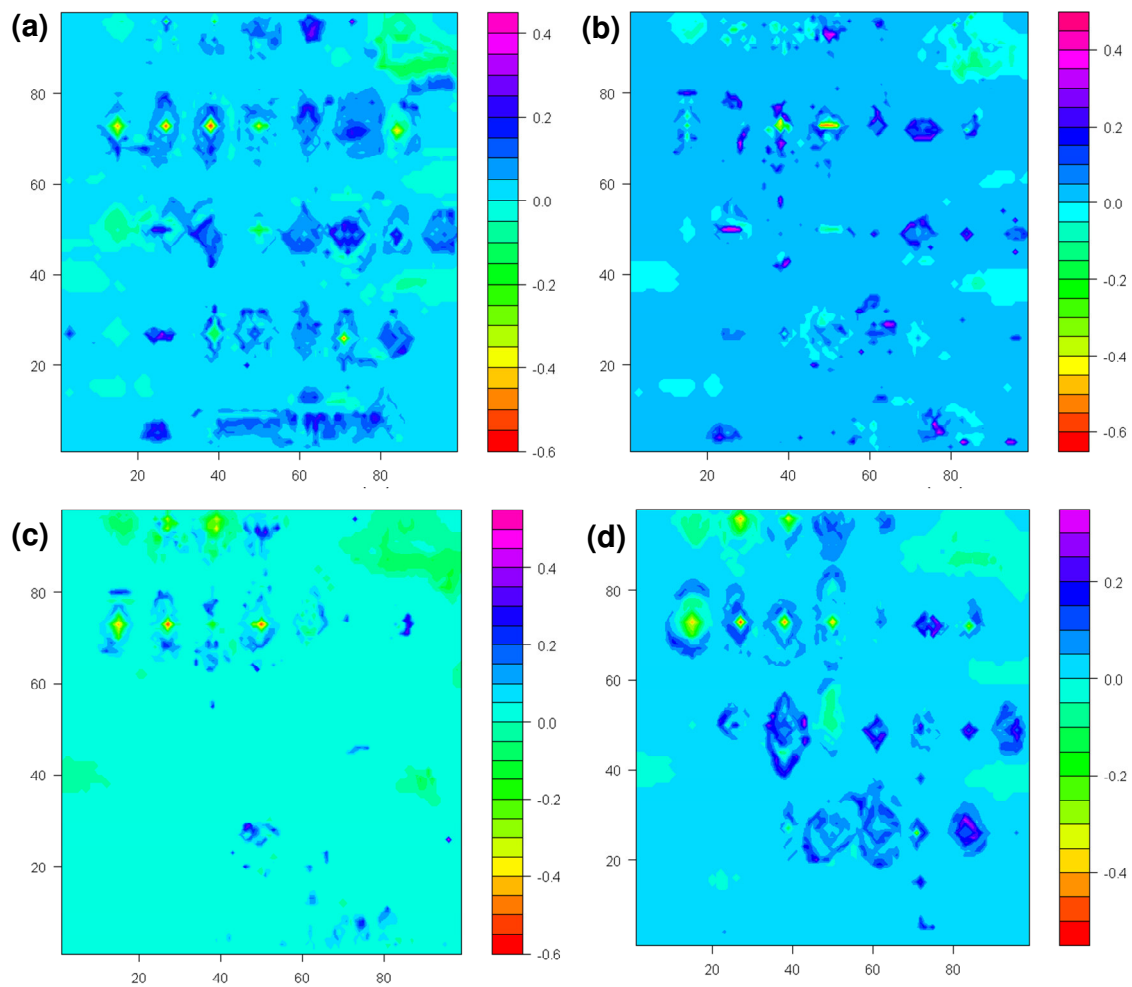


Figure 4.45: Thickness averaged gas saturation difference maps for (a) marly, (b) upper vuggy(V1), (c) lower vuggy(V2), and (d) lower vuggy(V4+) sections

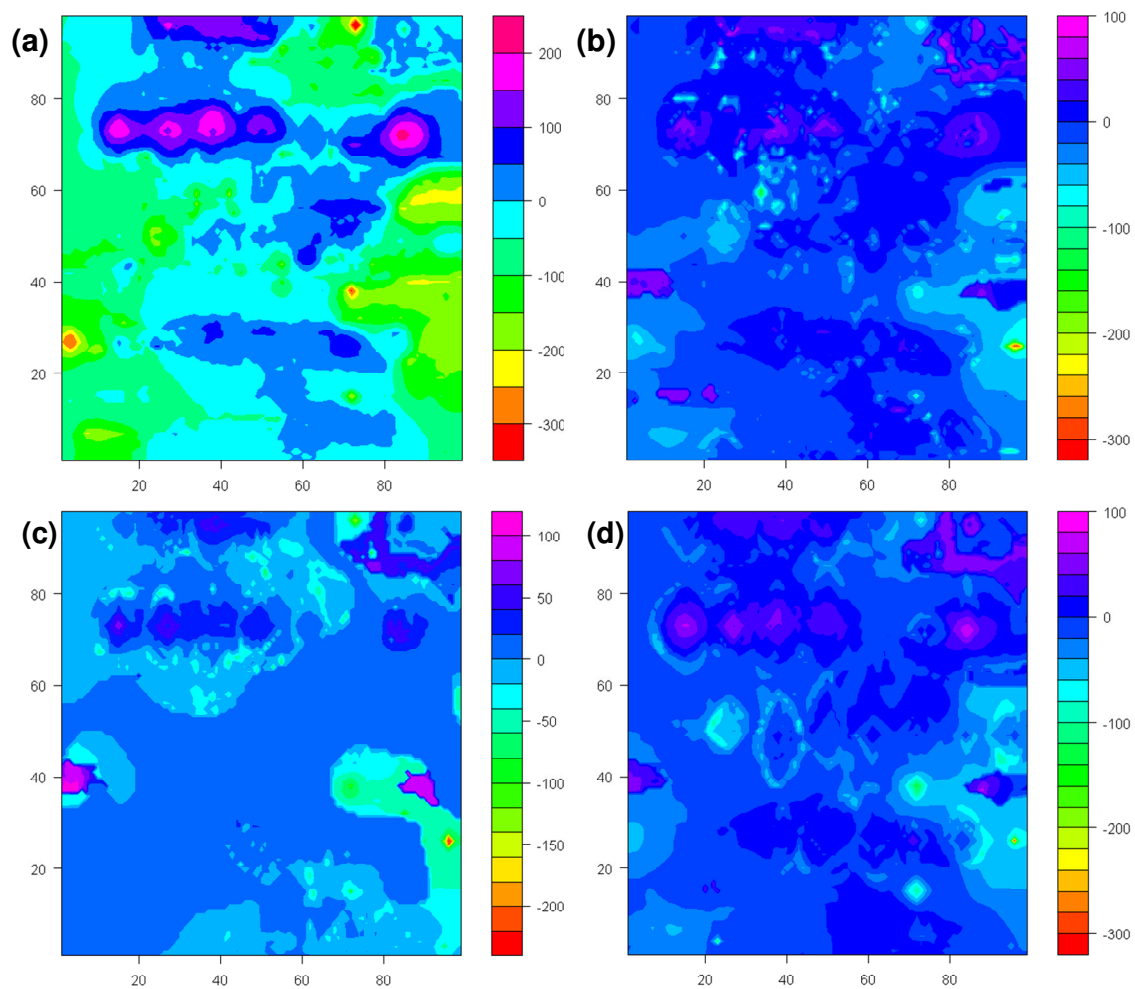


Figure 4.46: Thickness averaged P-wave velocity difference maps (in m/sec) for (a) marly, (b) upper vuggy (V1), (c) lower vuggy (V2), and (d) lower vuggy (V4+) sections

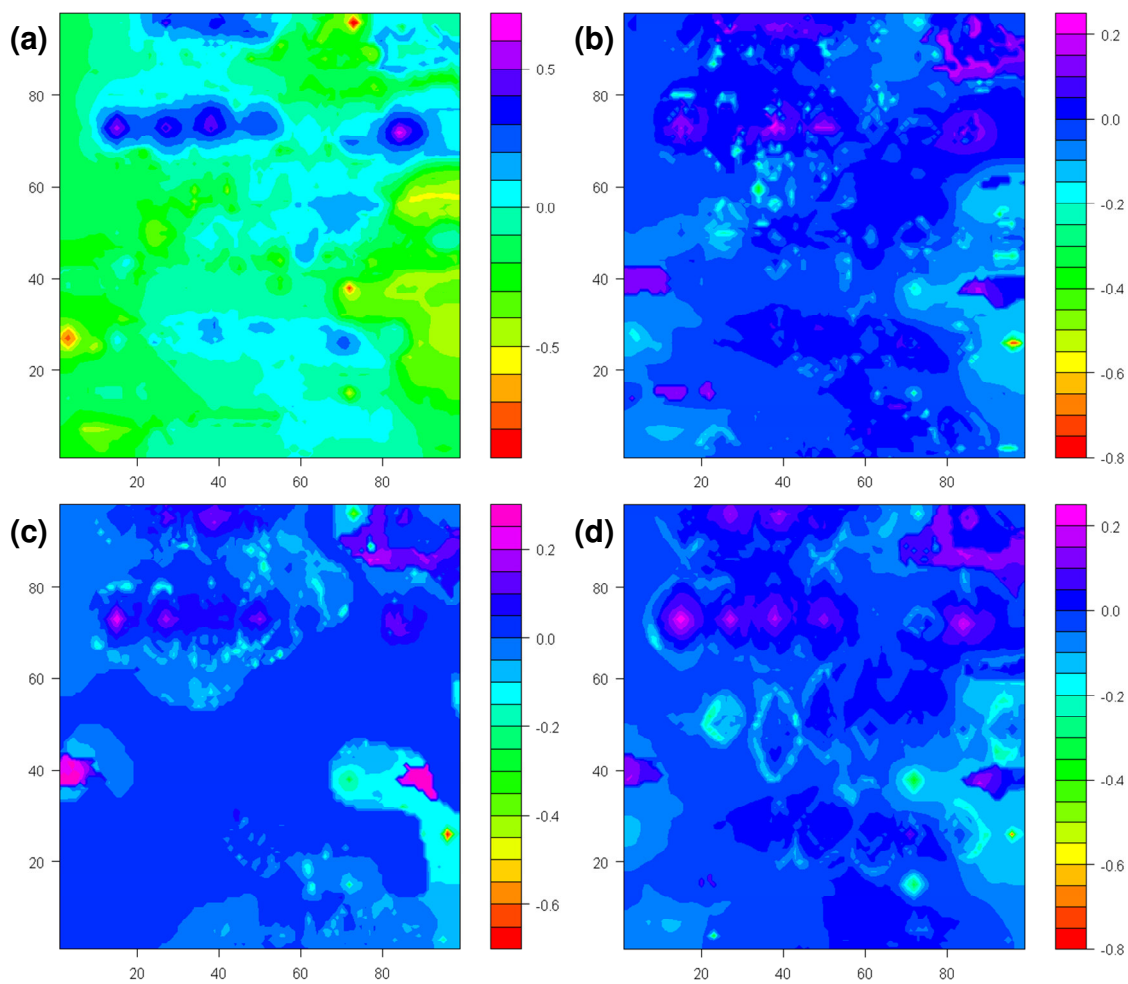


Figure 4.47: Thickness averaged P-wave impedance difference maps (in $10^6 \text{ kg/m}^2/\text{sec}$) for (a) marly, (b) upper vuggy(V1), (c) lower vuggy(V2), and (d) lower vuggy(V4+) sections

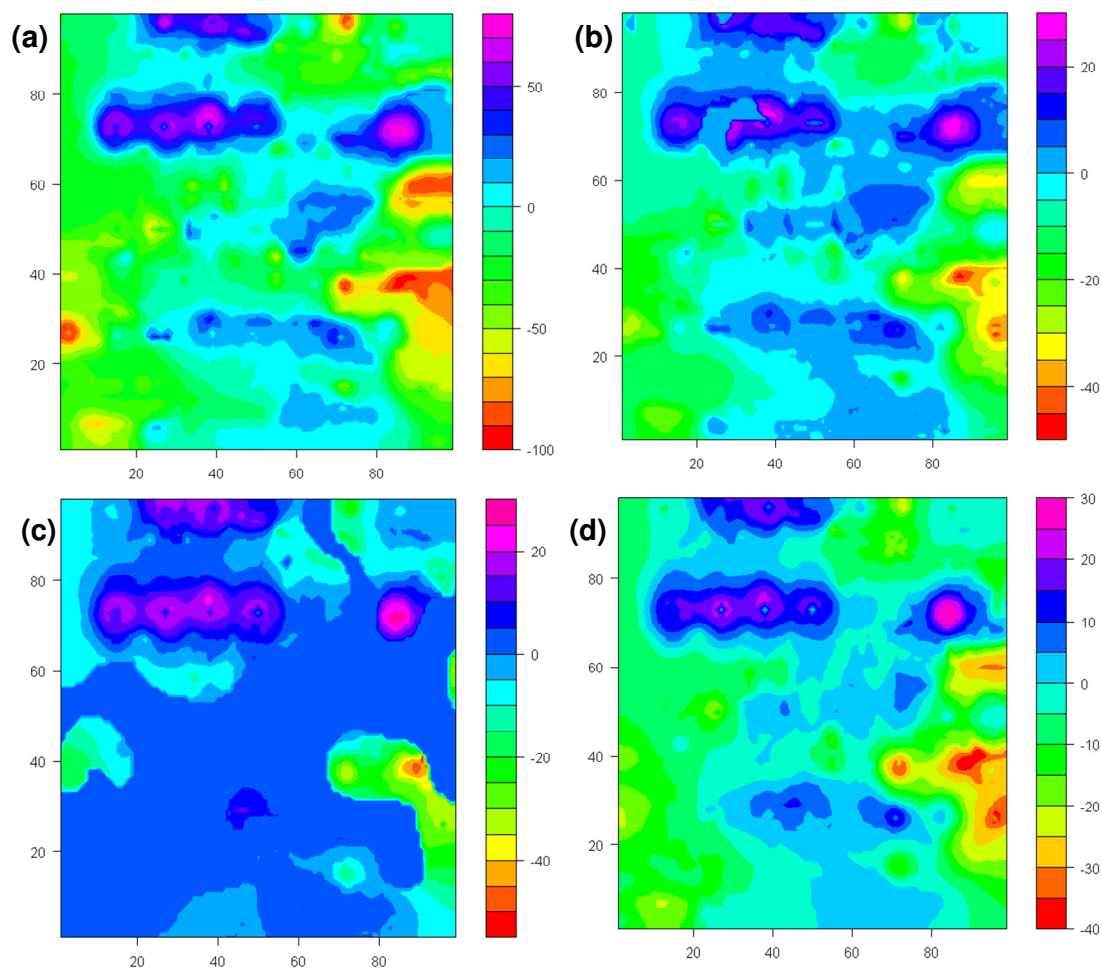


Figure 4.48: Thickness averaged S-wave velocity difference maps (in m/sec) for (a) marly, (b) upper vuggy(V1), (c) lower vuggy(V2), and (d) lower vuggy(V4+) sections

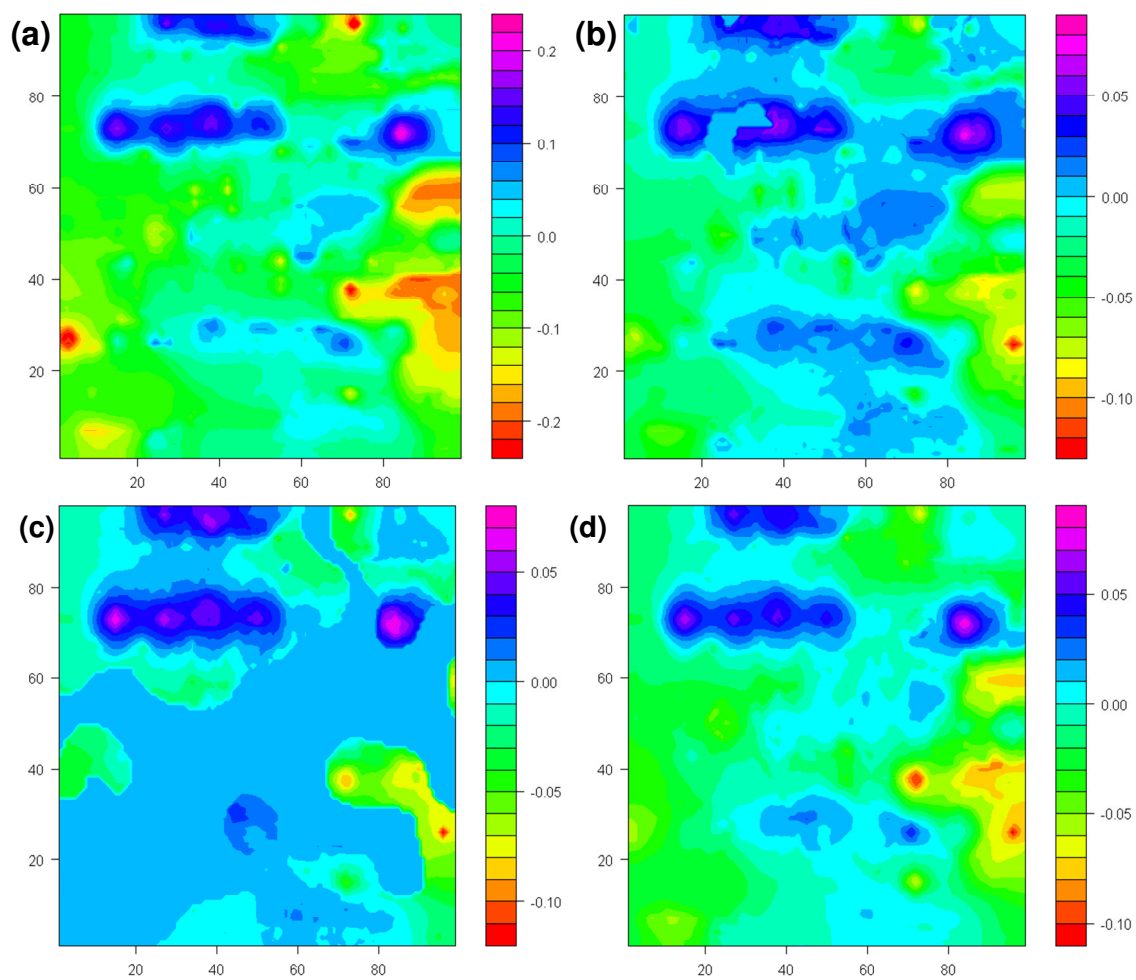


Figure 4.49: Thickness averaged S-wave impedance difference maps (in $10^6 \text{ kg/m}^2/\text{sec}$) for (a) marly, (b) upper vuggy(V1), (c) lower vuggy(V2), and (d) lower vuggy(V4+) sections

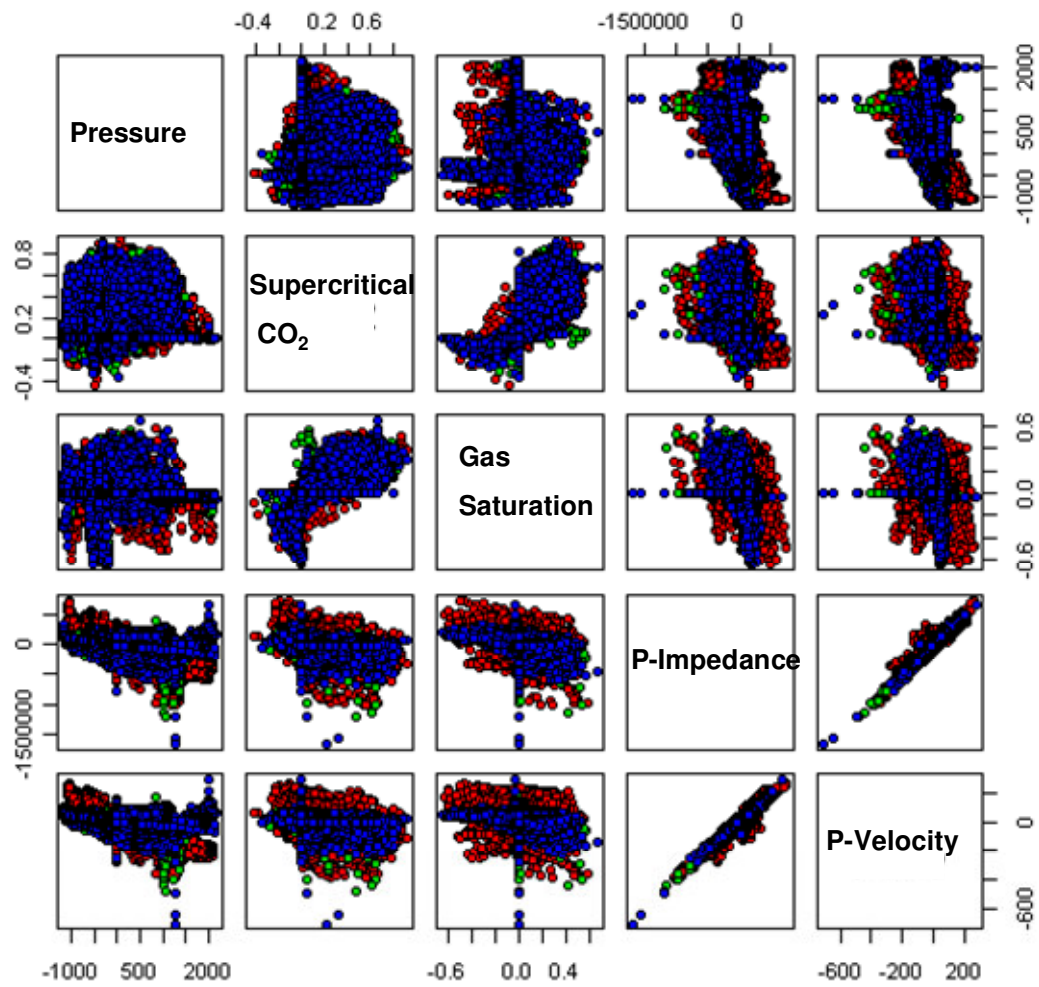


Figure 4.50: Scatterplot showing relationship between simulated time-lapse P-wave properties and time-lapse flow parameters for Weyburn field. (marly in red, upper vuggy in green, and lower vuggy in blue)

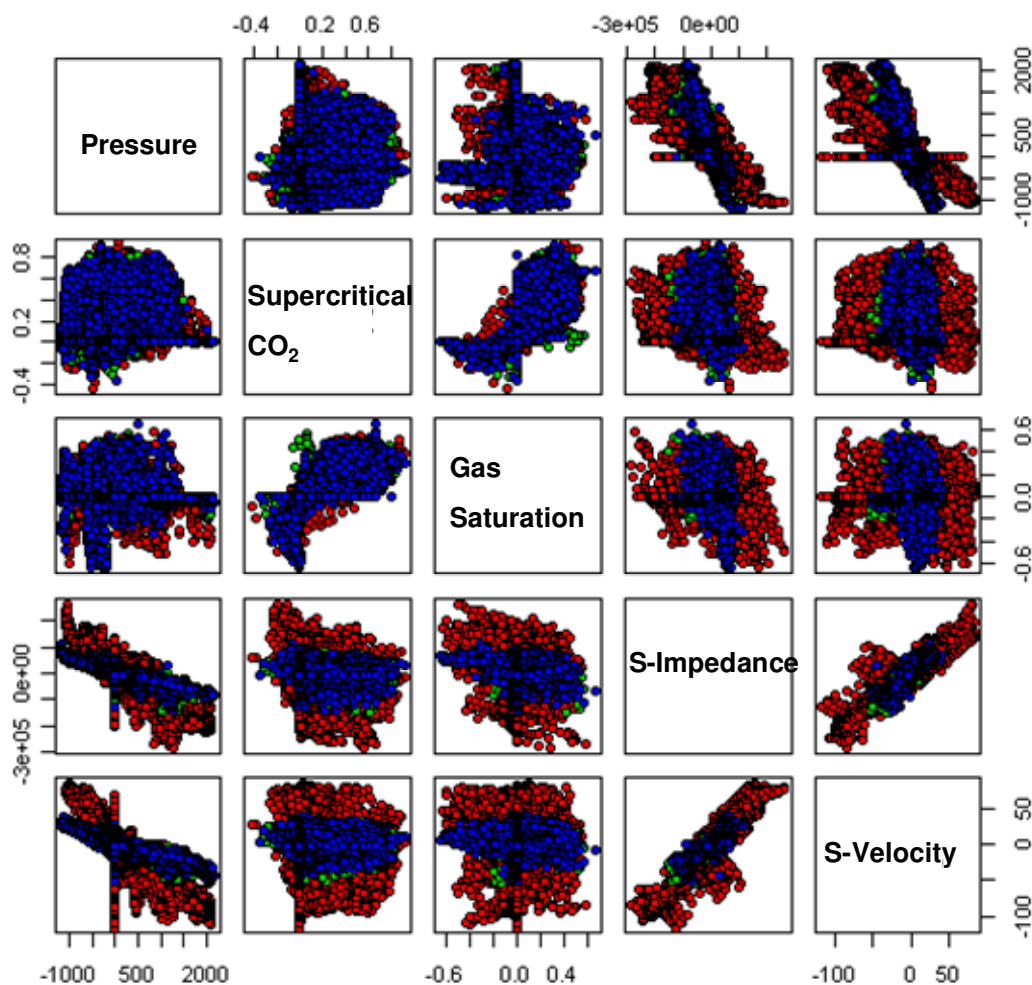


Figure 4.51: Scatterplot showing relationship between simulated time-lapse S-wave properties and time-lapse flow parameters for Weyburn field. (marly in red, upper vuggy in green, and lower vuggy in blue)

4.2.4 Comparison with Field Data

Encana provided the squared differences for P-wave impedance values between the two times, December 2004 and November 2005. These values were averaged using two-way travel time values for the geologic layers. In this study thickness values were used for averaging, as two-way travel time values for each layers were not available for this

study. Figure 4.52 shows the travel-time-averaged differences in squared P-wave impedance values for the four geologic sections. Values are inappropriate near the edges because a lesser number of CDPs (common depth points) are available in that region. The data show a noisy character compared with simulated values. Also, top marly and lower vuggy (V4+) layers show larger changes when compared with the other two layers. This is consistent with the observation for the simulated values.

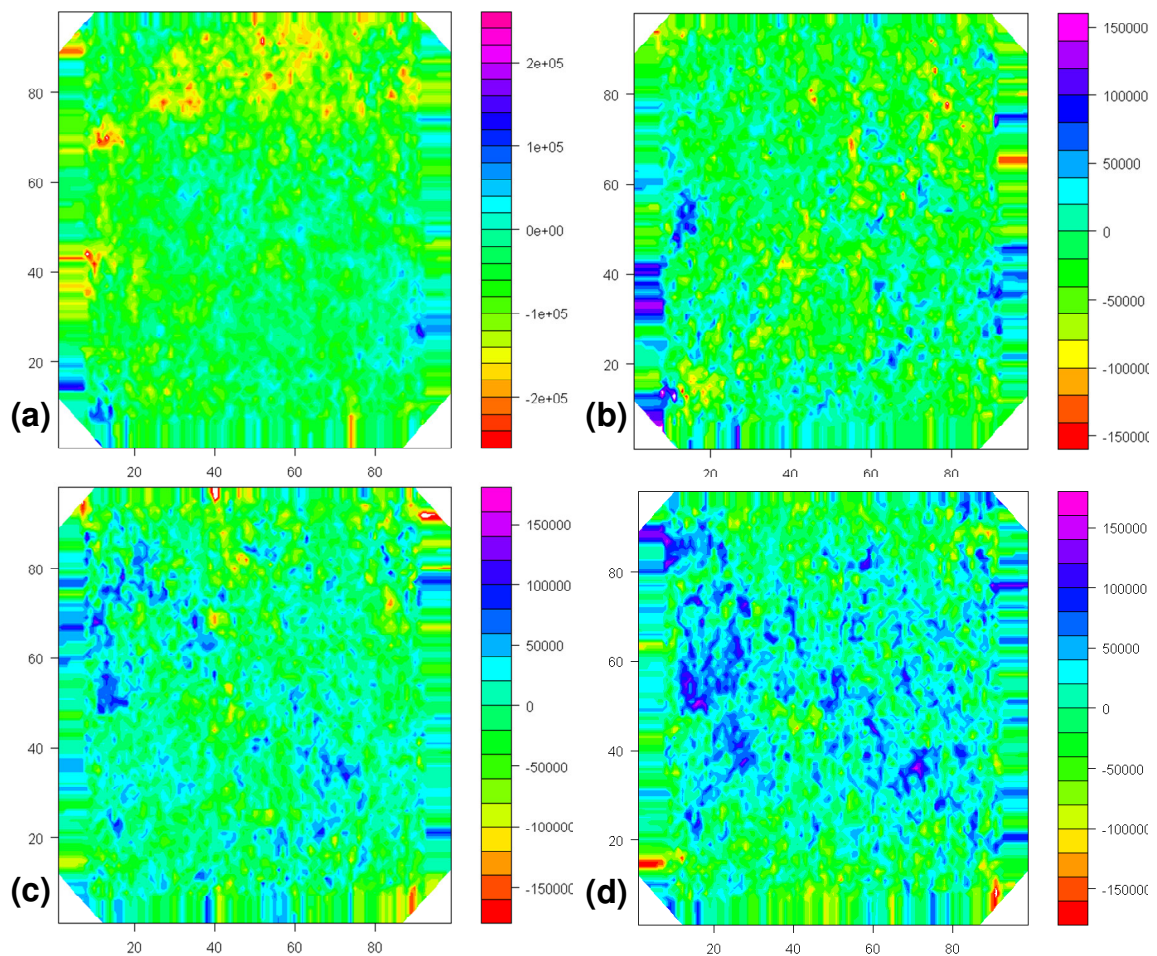


Figure 4.52: Two-way time averaged, squared P-wave impedance difference maps for (a) marly, (b) upper vuggy(V1), (c) lower vuggy(V2), and (d) lower vuggy(V4+) sections

CHAPTER V

CONCLUSIONS AND RECOMMENDATIONS

Conclusions and recommendations for the various studies performed in this research work are listed below:

5.1. Large-Scale Hydrocarbon Reservoir Data Assimilation

The efficacy of the EnKF algorithm for large-scale hydrocarbon data assimilation is verified. Various critical issues related to history matching a large field with substantial production history have been explored. These include optimal initial member selection while preserving the covariance subspace, covariance localization and inflation to avoid filter divergence, and preserving geologic realism during history matching. EnKF was also used to history match CO₂-injection-supported hydrocarbon production. Carbon-dioxide injection requires the use of a more complex compositional simulation. Some key conclusions from this study are as follows:

- An efficient approach based on spectral clustering to select ‘optimal’ initial ensemble members using their dynamic response in terms of swept pore volume computed from the streamline time-of-flight is proposed. Unlike the current approach in the literature that focuses on the dissimilarity of the ensemble members themselves, the focus is on the dissimilarity of their dynamic response

which is more efficient as well as relevant for history matching. Member selection worked well both for a small synthetic case and a large field case.

- Filter divergence is a problem encountered when studying large models with substantial production history. Covariance localization helps in avoiding filter divergence at any assimilation step by removing spurious covariances between an observation location and far-off grids. Thus, it localizes analyses in space. Covariance inflation helps in avoiding filter divergence by discounting the influence of past observation on the current analysis. Thus, it localizes the analysis in time. While localization clearly helped in improving assimilation results, inflation did not. A more robust approach may be required for using inflation in assimilation studies.
- A hydrocarbon reservoir system is highly non-linear, but EnKF assumes linear correlations. Hence, it makes large changes to permeabilities even though smaller changes would be sufficient if non-linearity were taken into account. For this reason, it becomes important to apply permeability cut-offs to preserve geologic realism. Without these cut-offs, the EnKF algorithm makes large changes to permeability and the forward model becomes unstable after few assimilation steps.
- Carbon-dioxide injection in the reservoir requires use of a compositional simulator for numerical studies. Moreover, the localized EnKF algorithm requires compositional streamlines for localization. Compositional streamline tracing using molar flux information from a finite-difference simulator is

shown. Finally, results from black-oil and compositional cases are compared, and it is shown that both result in a similar degree of improvement upon history-matching.

5.2. Time-Lapse Seismic Monitoring of CO₂ Sequestration

The viability of time-lapse monitoring of CO₂ injection in hydrocarbon reservoirs, specifically in carbonate reservoirs, is examined. The unique aspect of this study is the use of a comprehensive flow simulator to model the CO₂ injection with all of the accompanying phase behavior and geochemical effects. The simulation results used in conjunction with seismic modeling clearly indicate the potential for time-lapse monitoring of CO₂ front movement during sequestration process. Our results also show that for accurate time-lapse response, it is important to model the precipitation and dissolution reactions that occur during CO₂ injection. Specifically, the CO₂ dissolution and the acidification of the brine trigger a variety of geochemical reactions that can significantly alter the rock-fluid properties. The gas-liquid dissolution and the intra-aqueous phase reactions are relatively fast and their effects on time-lapse seismic response can be seen at the end of CO₂ injection. The mineral reactions are typically very slow and their effects are detectable only after hundreds of years. Salinity change, which is on the order of 10% in this study, changes the brine phase properties significantly. The combination of physical and chemical changes in the sequestration reservoir lead to changes in AVO attributes on the order of 15%, suggesting that these

parameters can be very useful tools for monitoring changes in reservoir conditions in a sequestration site.

A time-lapse seismic study was also performed for the Weyburn field. The study shows that CO₂ injection monitoring is possible using the time-lapse seismic data. Seismic attributes at any time are primarily correlated with the porosity values, while differences in seismic attributes between any two times are due to the CO₂ injection and pressure changes within the reservoir. Simulated values as well as observed data for the P-impedances show maximum changes in the top marly and lower vuggy (V4+) layer. This is because most of the CO₂ was injected in these two layers. Observed data is very noisy in comparison with simulated values. Further study is required to properly correlate simulated values and observed data. Time-lapse seismic data may also be used in conjunction with production data for improved history-matching.

5.3.Recommendations

EnKF has limited ability to handle non-gaussian and/or non-linear systems. Various approaches have been suggested in literature for tackling this problem. Kernel methods may be used to model non-linearity, while martingales may be used to model non-gaussianity. Covariance inflation seems to work for smaller size problems, but not for large scale problem with significant production history. Inflation measure should be tuned so as to avoid instability caused by it. Time-lapse seismic data for Weyburn field

is noisy; therefore further study is required to find ways to utilize it in integrated assimilation study.

REFERENCES

- Anderson, J.L., and Anderson, S.L. (1999). A Monte Carlo Implementation of the Nonlinear Filtering Problem to Produce Ensemble Assimilation and Forecasts. *Monthly Weather Review*. 127:2741-2758.
- Arroyo-Negrete, E., Devagowda, D., and Datta-Gupta, A. (2006). Streamline Assisted Ensemble Kalman Filter for Rapid and Continuous Reservoir Model Updating. Proc of the Int. Oil & Gas Conf and Exhibition, SPE 104255, Dec 5-7.
- Bachu, S. (2003). Screening and Ranking of Sedimentary Basins for Sequestration of CO₂ in Geological Media in Response to Climate Change. *Environmental Geology*. 44:277-289.
- Batzle, M., and Wang, Z. (1992). Seismic Properties of Pore Fluids. *Geophysics*. 57:1396-1408.
- Benson, S., and Cook, P. (2005). Underground Geological Storage. *IPCC Special Report on Carbon Dioxide Capture and Storage*. Cambridge University Press, New York, NY.
- Borg, I., and Groenen, P.J.F. (2005). *Modern Multidimensional Scaling: Theory and Applications*. 2nd ed., Springer, New York, NY.
- Brown, L. T. (2002). *Integration of rock physics and reservoir simulation for the interpretation of time-lapse seismic data at Weyburn field, Saskatchewan*. M.S. Thesis, Colorado School of Mines, Golden, CO.
- Burrowes, G. (2001). Investigating CO₂ Storage Potential of Carbonate Rocks during Tertiary Recovery from a Billion Barrel Oil Field, Weyburn, Saskatchewan: Part 2- Reservoir Geology (IEA Weyburn CO₂ Monitoring and Storage Project). *Summary of investigations 2001*, Volume 1, Saskatchewan Geological Survey, Sask. Energy Mines, Misc. Rep. 2001-4.1.
- Challa, S., and Bar-shalom, Y. (2000). Nonlinear Filter Design Using Fokker-Planck-Kolmogorov Probability Density Evolutions. *IEEE Transactions on Aerospace and Electronic Systems*. 36:309-135.

- Dong, Y., Gu, Y., and Oliver, D.S. (2006). Sequential Assimilation of 4D Seismic Data for Reservoir Description Using the Ensemble Kalman Filter. *Journal of Petroleum Science and Engineering*. 53:83-99.
- Evensen, G. (1994). Sequential Data Assimilation with a Nonlinear Quasi-Geostrophic Model Using Monte Carlo Methods to Forecast Error Statistics. *Journal of Geophysical Research*. 99:143-162.
- Evensen, G. (2003). The Ensemble Kalman Filter: Theoretical Formulation and Practical Implementation. *Ocean Dynamics*. 53:343-367.
- Evensen, G. (2004). Sampling Strategies and Square Root Analysis for Ensemble Kalman Filter. *Ocean Dynamics*. 54:539-560.
- Firoozabadi, A., Nutakki, R., Wong, T.W., and Aziz, K. (1988). EOS Predictions of Compressibility and Phase Behavior in Systems Containing Water, Hydrocarbons, and CO₂. *SPE Reservoir Engineering*. 3:673-684.
- Freund, P., Bachu, S., Simbeck, D., Thambimuthu, K., and Gupta, M. (2005). Annex I: Properties of CO₂ and Carbon-based Fuels. *IPCC Special Report on Carbon Dioxide Capture and Storage*. Cambridge University Press, New York, NY.
- Garcia, J. E. (2001). Density of Aqueous Solutions of CO₂. Lawrence Berkeley National Laboratory, Report LBNL-49023.
- Gassmann, F. (1951). Elastic Waves through a Packing of Spheres. *Geophysics*, 16:673-685.
- Grimston, M.C., Karakoussis, V., Rouquet, R., van der Vorst, R., Pearson, P., and Leach, M. (2001). The European and Global Potential of Carbon dioxide Sequestration in Tackling Climate Change. *Climate Policy*. 1:155-171.
- Hamill, T.M., Whitaker, J.S., and Snyder, C. (2001). Distance-Dependent Filtering of Background Error Covariance Estimates in an Ensemble Kalman Filter. *Monthly Weather Review*. 129:2776-2790.
- Harris, J., Nolen-Hoeksema, R.C., Langan, R.T., Van Schaack, M., Lazaratos, S.K., and Rector III, J.W. (1995). High-resolution Crosswell Imaging of a West Texas Carbonate Reservoir: Part 1 – Project Summary and Interpretation. *Geophysics*. 60:667-681.
- Hepple, R.P. and Benson, S.M. (2005). Geologic Storage of Carbon dioxide as a Climate Change Mitigation Strategy: Performance Requirements and the Implications of Surface Seepage. *Environmental Geology*. 47:576-585.

- Hnedkovský, L., Wood, R. H., and Majer, V. (1996). Volumes of Aqueous Solutions of CH₄, CO₂, H₂S and NH₃ at Temperatures from 298.15 K to 705 K and Pressures to 35 Mpa. *Journal of Chemical Thermodynamics*. 28:125-142.
- Houghton, J., Ding, Y., Griggs, D., Nouguer, M., van der Linden, P., and Dai, X. (2001). *Climate Change 2001: The Scientific Basis*, Cambridge University Press, New York, NY.
- Houtekamer, P.L., and Mitchell, H.L. (2001). A Sequential Ensemble Kalman Filter for Atmospheric Data Assimilation. *Monthly Weather Review*. 129:123-137.
- Hunt, B.R., Kostelich, E.J., and Szunyogh, I. (2007). Efficient Data Assimilation for Spatiotemporal Chaos: A Local Ensemble Transform Kalman Filter. *Physica D*. 230:112-126.
- Isard, M., and Blake, A. (1998). CONDENSATION - Conditional Density Propagation for Visual Tracking. *International Journal of Computer Vision*. 29:5-28.
- Jazwinski, A.H. (1970). *Stochastic Process and Filtering Theory*. Academic Press, New York, NY.
- Jennings, J.W. and Lucia, F.J. (2003). Predicting Permeability from Well Logs in Carbonates with a Link to Geology for Interwell Permeability Mapping. *SPE Reservoir Evaluation & Engineering*. 6:215-225.
- Jiminez, E., Datta-Gupta, A., and King, M.J. (2008). Streamline Tracing in Complex Faulted Systems with Non-Neighbor Connections. SPE113628 presented at the SPE Improved Oil Recovery Symposium, Tulsa, OK.
- Kumar, A. (2004). A Simulation Study of Carbon Sequestration in Deep Saline Aquifers. M.S. Thesis, The University of Texas at Austin.
- Kumar, A., Datta-Gupta, A., Shekhar, R., and Gibson, R.L. (2008). Modeling Time Lapse Seismic Monitoring of CO₂ Sequestration in Hydrocarbon Reservoirs Including Compositional and Geochemical Effects. *Petroleum Science and Technology*. 26:887-911.
- Kumar, A., Ozah, R.C., Noh, M., Pope, G., Sepehrnoori, k., Bryant, S., and Lake, L.W. (2005). Reservoir Simulation of CO₂ Storage in Deep Saline Aquifers. *SPE Journal*. 10:336-348.
- Kwok, J.T.Y., and Tsang, I.W.H. (2004). The Pre-image Problem in Kernel Methods. *IEEE Transaction on Neural Networks*. 15:6, 1517-1525.

- Landro, M., Solheim, O., Hilde, E., Ekren, B., and Stronen, L. (1999). The Gullfaks 4D Seismic Study. *Petroleum Geosciences*. 5:213-226.
- Li, Y. K. and Nghiem, L. X. (1986). Phase Equilibria of Oil, Gas and Water/Brine Mixtures from a Cubic Equation of State and Henry's Law. *Canadian Journal of Chemical Engineering*. 64:486-496.
- Lichtner, P.C., Steefel, C.I., and Oelkers, E.H. (1996). *Reactive Transport in Porous Media*. Reviews in Mineralogy, 34.
- Lin, L., and Phair, R. (1993). AVO Tuning. 63rd SEG meeting, Washington, DC, USA, Expanded Abstracts, 727-730.
- Matos, M.C., Osorio, P.L.M., and Johann, P.R.S. (2007). Unsupervised Seismic Facies Analysis Using Wavelet Transform and Self-organizing Maps. *Geophysics*. 72:9-21.
- Mavko, G., Mukerji, T. and Dvorkin, J. (2003). *The Rock Physics Handbook: Tools for Seismic Analysis of Porous Media*. Cambridge University Press, New York, NY.
- Mukerji, T., Jorstad, A., Avseth, P., Mavko, G., and Granli, J.R. (2001). Mapping Lithofacies and Pore-fluid Probabilities in a North Sea Reservoir: Seismic Inversions and Statistical Rock Physics. *Geophysics*. 66:988-1001.
- Ng, A.Y., Jordan, M.I., and Weiss, Y. (2002). On Spectral Clustering: Analysis and an Algorithm. Advances in Neural Information Processing Systems (NIPS) 14. MIT Press, Cambridge, MA.
- Nghiem, L. (2002). *Compositional Simulator for Carbon Dioxide Sequestration*. Computer Modeling Group Ltd., Calgary, Canada.
- Nghiem, L. (2003). *Compositional Simulator for Carbon Dioxide Sequestration-Part 2*. Computer Modeling Group Ltd, Calgary, Canada.
- Nolen-Hoeksema, R.C., Wang, Z., Harris, J.M., and Langan, R.T. (1995). High-resolution Crosswell Imaging of a West Texas Carbonate Reservoir: Part 5 – Core Analysis. *Geophysics*. 60:712-726.
- Pan, G. (2006). CO2 EOR Sequestration Experience: The Weyburn Story. Workshop on Gasification Technologies, Bismarck, ND.
- Paola, M.D., and Sofi, A. (2002). Approximate Solution of the Fokker-Planck-Kolmogorov Equation. *Probabilistic Engineering Mechanics*. 17:369-384.

- Parkinson, W. and Nevers, N. D. (1969). Partial Molal Volume of Carbon Dioxide in Water Solutions. *Industrial and Engineering Chemistry Fundamentals*. 8:709-713.
- Rumpf, B., Nicolaisen, H., Ocal, C. and Maurer, G. (1994). Solubility of Carbon Dioxide in Aqueous Solutions of Sodium Chloride: Experimental Results and Correlation. *Journal of Solution Chemistry*. 23:431-448.
- Scharlin, P. (1996). *Carbon Dioxide in Water and Aqueous Electrolyte Solutions*, Volume 62 of Solubility Data Series, Oxford University Press, International Union of Pure and Applied Chemistry.
- Scheevel, J.R., and Payrazyan, K. (2001). Principal Component Analysis Applied to 3D Seismic Data for Reservoir Property Estimation. *SPE Reservoir Evaluation and Engineering*. 4:64-72.
- Scheidt, C., and Caers, J. (2007). Using Distances and Kernels to Parameterize Spatial Uncertainty for Flow Applications. EAGE Petroleum Geostatistics conference, Cascais, Portugal, September 10-14.
- Scholkopf, B., and Smola, A.J. (2002). *Learning with Kernels*, MIT Press, Cambridge, MA.
- Scholkopf, B., Knirsch, P., Smola, A., and Burges, C. (1998). Fast Approximation of Support Vector Kernel Expansions, and an Interpretation of Clustering as Approximation in Feature Spaces. DAGM-Symposium, Mustererkennung, 125-132.
- Shekhar, R., and Gibson, R. L. (2005). Fractured Reservoir Characterization Using Seismics. 75th Ann. Internat. Mtg., Soc. Expl. Geophys., Expanded Abstracts, pages 1445-1449.
- Shuey, R.T. (1985). A Simplification of the Zoeppritz Equations. *Geophysics*. 50:609-614.
- Simonson, J. M., Oakes, C. S., and Bodnar, R. J. (1994). Densities of NaCl(aq) to the Temperature 523 K at Pressures to 40 MPa Measured with a New Vibrating-tube Densitometer. *Journal of Chemical Thermodynamics*. 26:345-359.
- Skorstad, A., Kolbjornsen, O., Drottning, A., Gjoystdal, H., and Huseby, O. (2006). Combining Saturation Changes and 4D Seismic for Updating Reservoir Characterizations. *SPE Reservoir Evaluation and Engineering*. 9:502-512.

- Span, R., and Wagner, W. (1996). A New Equation of State for Carbon Dioxide Covering the Fluid Region from the Triple-Point Temperature to 1100 K at Pressures up to 800 MPa. *Journal of Physical and Chemical Reference Data*. 25:1509-1596.
- Spycher, N., Pruess, K., and Ennis-King, J. (2002). CO₂-H₂O Mixtures in the Geological Sequestration of CO₂. I. Assessment and Calculation of Mutual Solubilities from 12 to 100 °C and up to 600 bar. Lawrence Berkeley National Laboratory, Report LBNL- 50991.
- Stumm, W. and Morgan, J.J. (1996). *Aquatic Chemistry: Chemical Equilibria and Rates in Natural Waters*. John Wiley & Sons, New York, NY.
- Syhlonyk, G. (1998). Advanced Rock Properties Study for PanCanadian Resources. Report No: 52132-98-1066 prepared by Core Laboratories Canada Ltd., Calgary, Canada.
- Teng, H. and Yamasaki, A. (1998). Solubility of Liquid CO₂ in Synthetic Sea Water at Temperatures from 278 K to 293 K and Pressures from 6.44 MPa to 29.49 MPa, and Densities of the Corresponding Aqueous Solutions. *Journal of Chemical & Engineering Data*. 43:2-5.
- Teng, H., Yamasaki, A., Chun, M. K. and Lee, H. (1997). Solubility of Liquid CO₂ in Water at Temperatures from 278 K to 293 K and Pressures from 6.44 MPa to 29.49 MPa and Densities of the Corresponding Aqueous Solutions. *Journal of Chemical & Engineering Data*. 29:1301-1310.
- Tsang, C.-F., Benson, S.M., Kobelski, B., and Smith, R.E. (2002). Scientific Considerations Related to Regulation Development for CO₂ Sequestration in Brine Formations. *Environmental Geology*. 42:275-281.
- Tura, A., and Lumley, D. E. (1998). Subsurface Fluid- Flow Properties from Time-Lapse Elastic- Wave Reflection Data. 43rd Ann. Mtg., SPIE, Proceedings, 25-138.
- Vargaftik, N. (1975). *Tables on Thermodynamic Properties of Liquids and Gases*. Hemisphere, Washington, DC.
- Vesovic, V., Wakeham, W.A., Olchowy, G.A., Sengers, J.V., Watson, J.T.R., and Millat, J. (1990). The Transport Properties of Carbon Dioxide. *Journal of Physical and Chemical Reference Data*. 19:763-808.

- Wagner, W. and Pruß, A. (2002). The IAPWS Formulation 1995 for the Thermodynamic Properties of Ordinary Water Substance for General and Scientific Use. *Journal of Physical and Chemical Reference Data*. 31:387-583.
- Wang, Z. and Nur, A. (1989). Effects of CO₂ Flooding on Wave Velocities in Rocks with Hydrocarbons. *SPE Reservoir Engineering*. 4:429-439.
- Wang, Z., Cates, M. E., and Langan, R. T. (1998). Seismic Monitoring of a CO₂ Flood in a Carbonate Reservoir: A Rock Physics Study. *Geophysics*. 63:1604-1617.
- Watts, G., Jizba, D., Gawith, D., and Gutteridge, P. (1996). Reservoir Monitoring of the Magnus Field through 4d Time- Lapse Seismic Analysis. *Petroleum Geosciences*. 2:361-372.
- Widess, M. B. (1973). How Thin is a Thin Bed?. *Geophysics*. 38:1176-1180.
- Wilson, M. and Monea, M. (2004). IEA GHG Weyburn CO₂ Monitoring and Storage Project Summary Report 2000-2004, Petroleum Technology Research Centre, Regina, Canada.
- Yamamoto, H. (2003). Using Time-lapse Seismic Measurements to Improve Flow Modeling of CO₂ Injection in the Weyburn Field: A Naturally Fractured, Layered Reservoir. Ph.D. Dissertation, Colorado School of Mines, Golden, CO.
- Zaytsev, I. D., and Aseyev, G. G. (1992). *Properties of Aqueous Solutions of Electrolytes*. CRC Press, Boca Raton, FL.

APPENDIX I

PROPERTIES OF CO₂ AND CO₂-H₂O MIXTURE

Carbon dioxide (CO₂) injection and sequestration in the hydrocarbon reservoir is one of the key focus areas of this study. In this annex, various physical and chemical properties of CO₂ and CO₂-H₂O mixture are presented. Table I.1 shows the physical properties of the carbon-dioxide (Span and Wagner, 1996; Vesovic *et. al.*, 1990). Figure I.1 shows the variation of CO₂ density with temperature and pressure, while Figure I.2 shows its phase behavior for conditions characteristic of sedimentary basins (Bachu, 2003). Table I.2 shows the thermodynamic data for selected carbon-containing compounds (Freund *et. al.*, 2005).

Table I.1: Physical properties of CO₂ at standard temperature and pressure

Property	Value
Molecular weight	44.01
Critical temperature	30.98°C
Critical pressure	7.38 MPa
Critical density	467.6 kg/m ³
Triple point temperature	-56.5°C
Triple point pressure	7.51 MPa
Normal boiling point @ 14.7 psi	-78.4°C
Density	1.976 kg/ m ³
Specific volume	0.506 m ³ /kg
C _p	36.39 J/mol/K
C _v	27.82 J/mol/K
Internal energy	19.08 kJ/mol
Enthalpy	21.34 kJ/mol
Entropy	117.22 J/mol/K
Viscosity	1.371E+05 Pa•s
Sound Speed	258.08 m/s
Thermal conductivity	0.014674 W/m/K

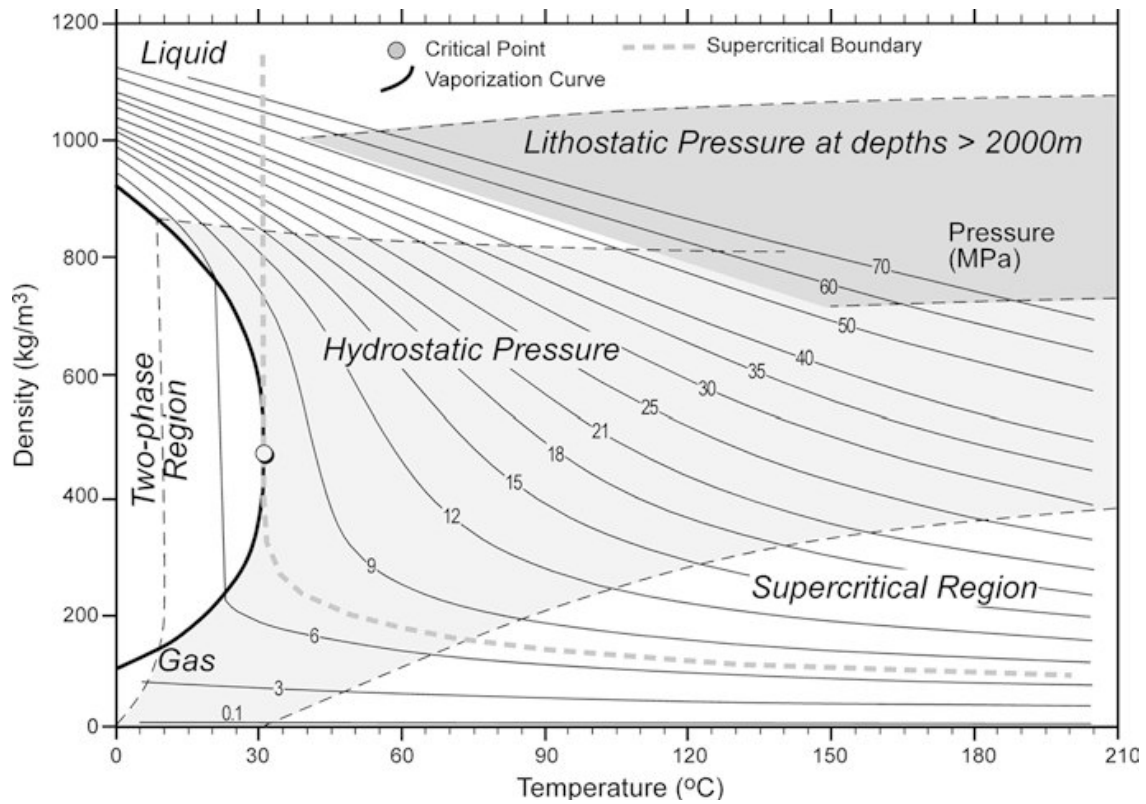


Figure I.1: Variation of CO₂ density as a function of temperature and pressure (Bachu, 2003)

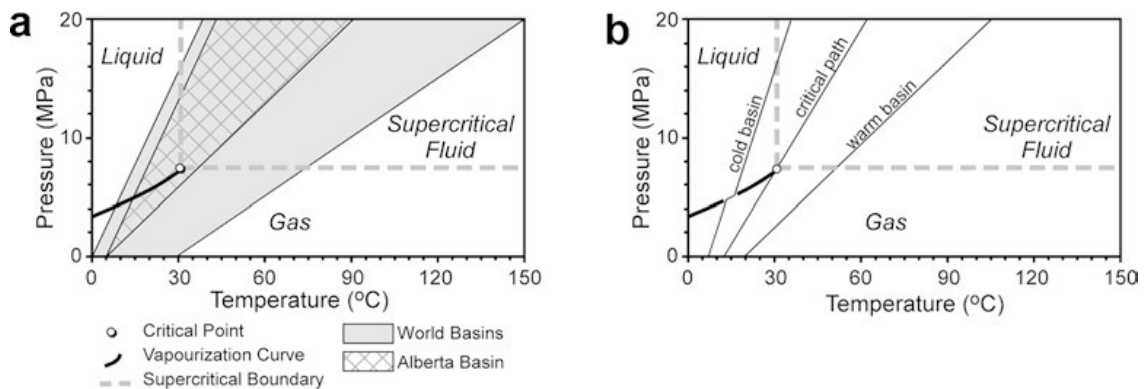
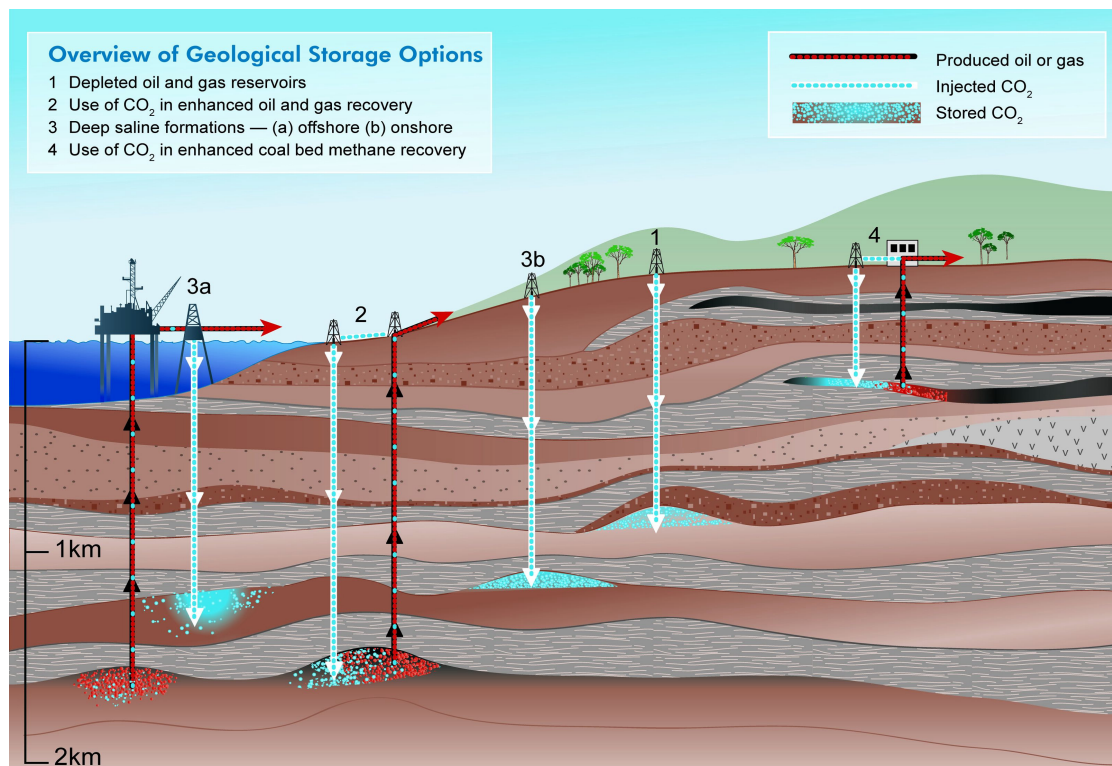


Figure I.2: Phase behavior of CO₂ conditions characteristic of sedimentary basins (Bachu, 2003)

Table I.2: Thermodynamic data for selected carbon-containing compounds (Freund *et. al.*, 2005)

Compound	Heat of formation, ΔH_f° kJ/mol	Gibbs free energy of formation, ΔG_f° kJ/mol	Standard molar enthalpy, S_f° J/mol/K
CO (g)	-110.53	-137.2	197.66
CO ₂ (g)	-393.51	-394.4	213.78
CO ₂ (l)		-386	
CO ₂ (aq)	-413.26		119.36
CO ₃ ²⁻ (aq)	-675.23		-50.0
CaO (s)	-634.92		38.1
HCO ₃ ⁻ (aq)	-689.93	-603.3	98.4
H ₂ O (l)	-285.83		69.95
H ₂ O (g)	-241.83		188.84
CaCO ₃ (s)	-1207.6 (calcite)	-1129.1	91.7
	-1207.8 (aragonite)	-1128.2	88
MgCO ₃ (s)	-1113.28 (magnesite)	-1029.48	65.09
CH ₄ (g)	-74.4	-50.3	186.3
CH ₃ OH (l)	-239.1	-166.6	126.8
(g)	-201.5	-162.6	239.8

**Figure I.3: Methods for storing CO₂ in deep underground geological formations (Benson and Cook, 2005)**

CO₂ sequestration in the geologic hydrocarbon reservoir or aquifer leads to interaction between carbon dioxide and brine (Figure I.3). Various physical and chemical processes need to be correctly modeled for studying this phenomenon. Some of these processes are discussed in the following section.

Phase behavior study using PR-EOS

Compositional simulator was used in this study to model the mass transfer of components between different phases. Peng-Robinson equation-of-state (PREOS) was used for phase calculations. Two components namely 'CO₂' and 'H₂O' were used to model carbon dioxide and brine respectively. Brine is modeled in oil phase so as to have better control on its behavior/properties. When carbon dioxide (component 'CO₂') and brine (component 'H₂O') are brought into contact, two phases are formed. One is the CO₂ rich gas phase, while other is H₂O rich liquid phase. As the simulators are mainly designed to handle oil, so the non-aqueous liquid phase containing mostly brine is labeled as oil phase by simulator.

CO₂ solubility into brine: CO₂ solubility calculated by PR-EOS does not always match the experimentally calculated values. So, we tune the parameter $BIC_{H_2O-CO_2}$ (binary interaction coefficient for H₂O-CO₂ pair), so as to get the correct value for solubility. A correlation was developed for binary interaction coefficient for H₂O-CO₂ pair in PR-EOS by Kumar (2004) and is given below:

$$BIC_{H_2O-CO_2} = -0.093625 + (4.861E - 4 \times (T - 113)) + (2.29E - 7 \times S) \quad (4.1)$$

where, $BIC_{H_2O-CO_2}$ is the binary interaction coefficient for H₂O-CO₂ pair, T is the temperature in Fahrenheit, and S is the salinity in ppm of NaCl. Figure I.4 shows the variation of $BIC_{H_2O-CO_2}$ with temperature and salinity. The computed curves for CO₂

solubility as a function of salinity and pressure for different temperatures are shown in Figure I.5 through Figure I.7 and compared with experimental data points when available.

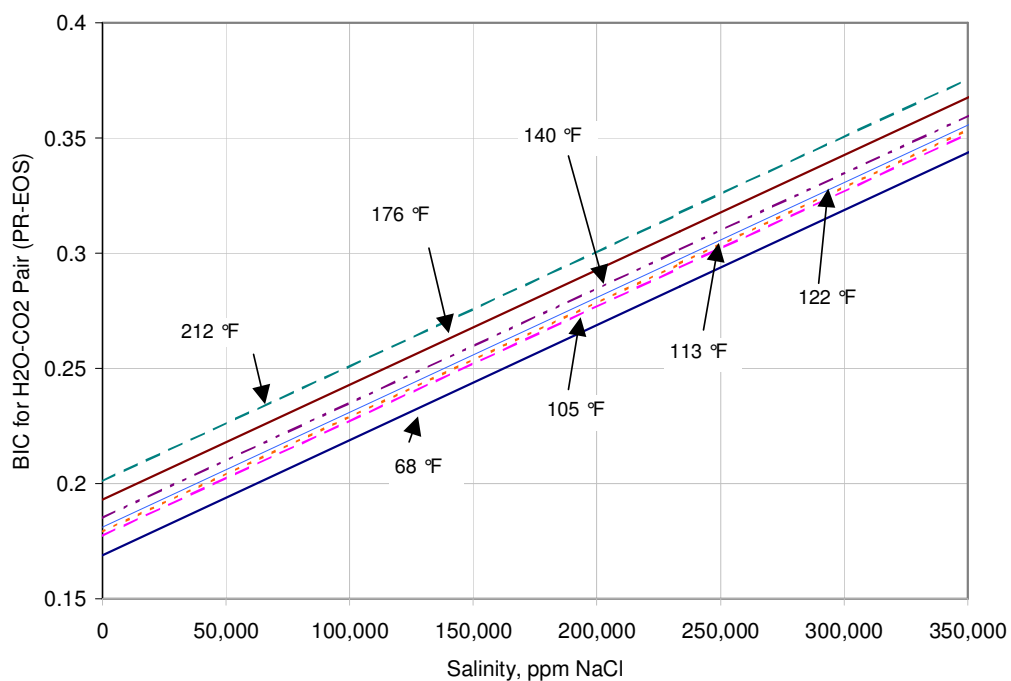


Figure I.4: Variation of Binary Interaction Coefficient for H₂O-CO₂ Pair used in Peng-Robinson Equation of State

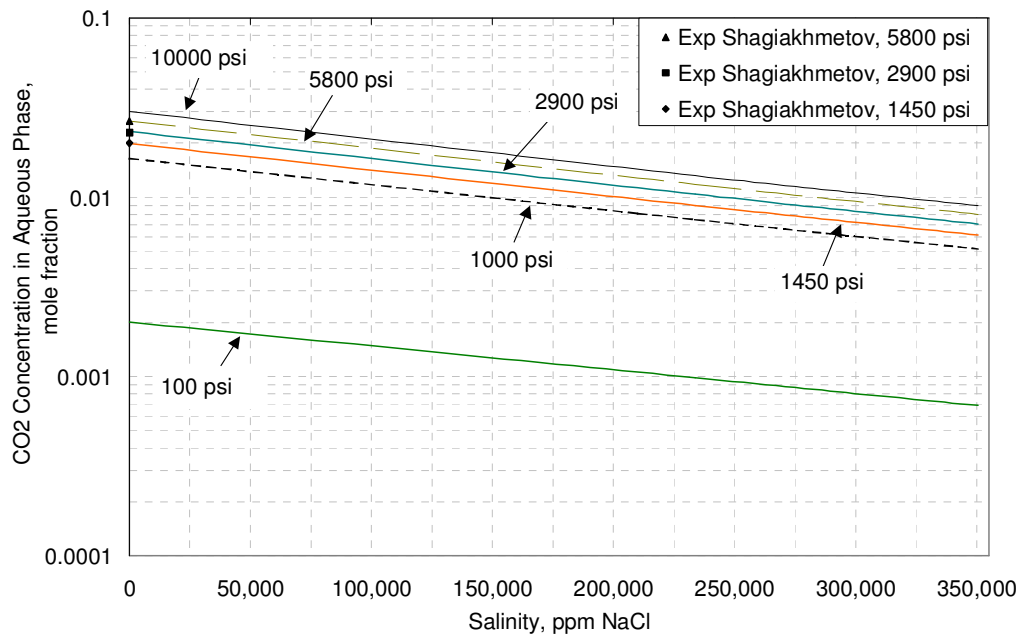


Figure I.5: Effect of Brine Salinity on CO₂ Solubility in Aqueous Phase, T = 122 °F

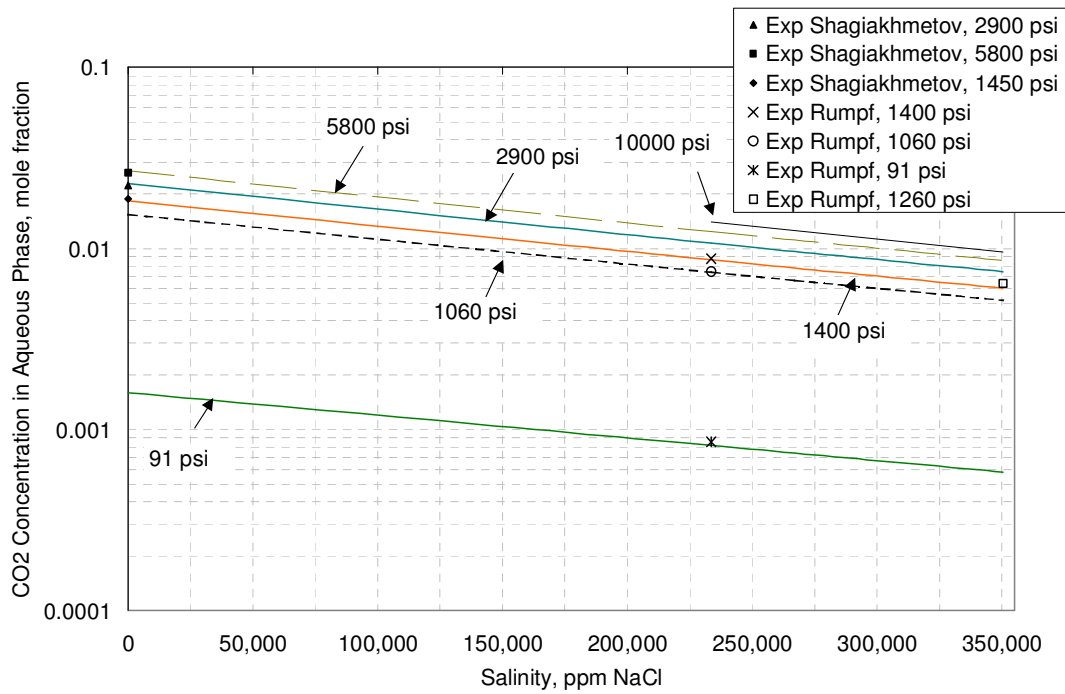


Figure I.6: Effect of Brine Salinity on CO₂ Solubility in Aqueous Phase, T = 140 °F

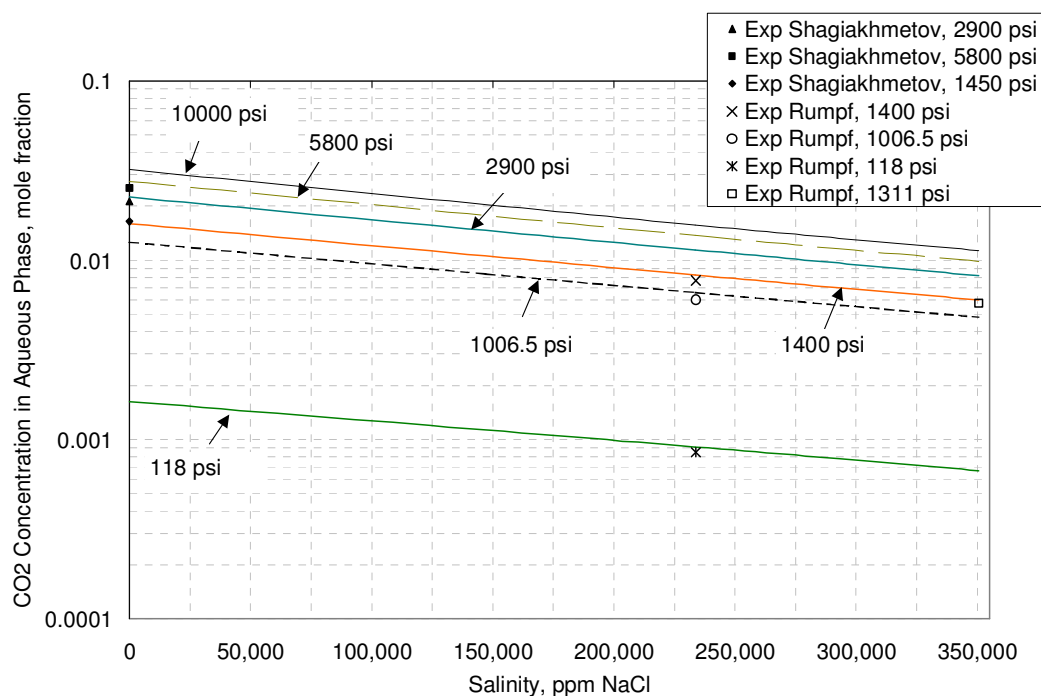


Figure I.7: Effect of Brine Salinity on CO₂ Solubility in Aqueous Phase, T = 176 °F

Brine density: Again to match the density values given by flash calculations to that given by experimental measurements, VSP_{H_2O} (volume shift parameter for component H₂O) needs to be tuned. A constant value of 0.024668 is used for VSP_{CO_2} (volume shift parameter for component CO₂). A correlation was developed for VSP_{H_2O} by Kumar (2004) and is given below:

$$VSP_{H_2O} = 0.179 + (2.2222E - 4 \times (T - 113)) + (4.9867E - 7 \times S) \quad (4.2)$$

where, VSP_{H_2O} is the volume shift parameter for component H₂O, T is the temperature in Fahrenheit, and S is the salinity in ppm of NaCl. Figure I.8 shows the variation of VSP_{H_2O} with temperature and salinity. The computed curves for CO₂-saturated brine density are shown as a function of salinity and pressure for different

temperatures in Figure I.9 through Figure I.11. Also, Figure I.12 through Figure I.14 compares the brine density with CO₂-saturated brine density for different pressure and salinity at 140°F.

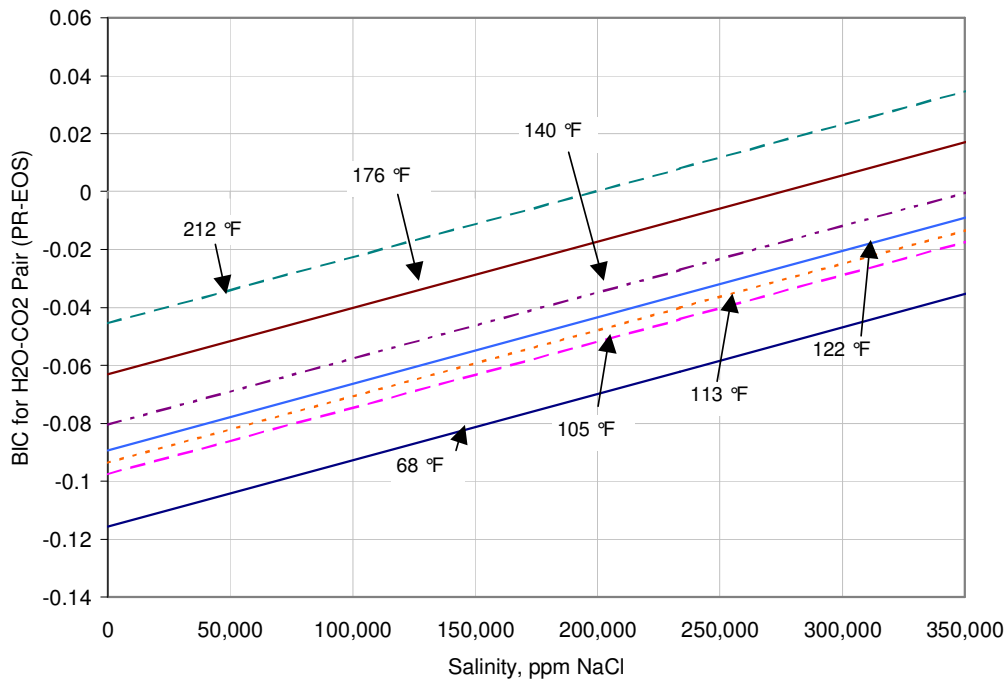


Figure I.8: Variation of Volume Shift Parameter for H₂O used in Peng-Robinson Equation of State

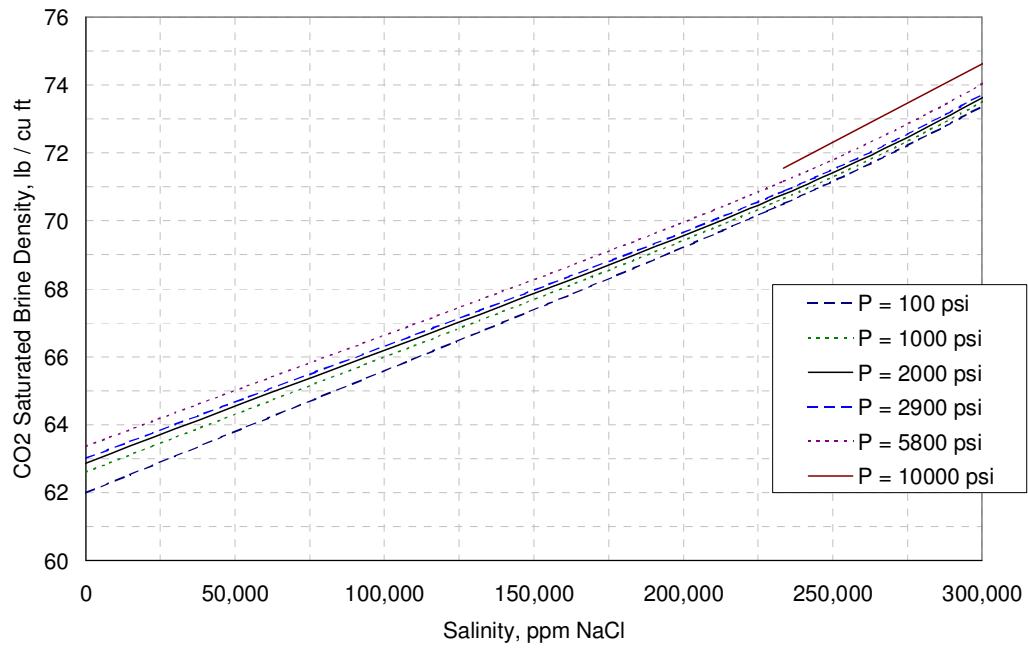


Figure I.9: Effect of Salinity on CO2-saturated Brine Density, T = 122 °F

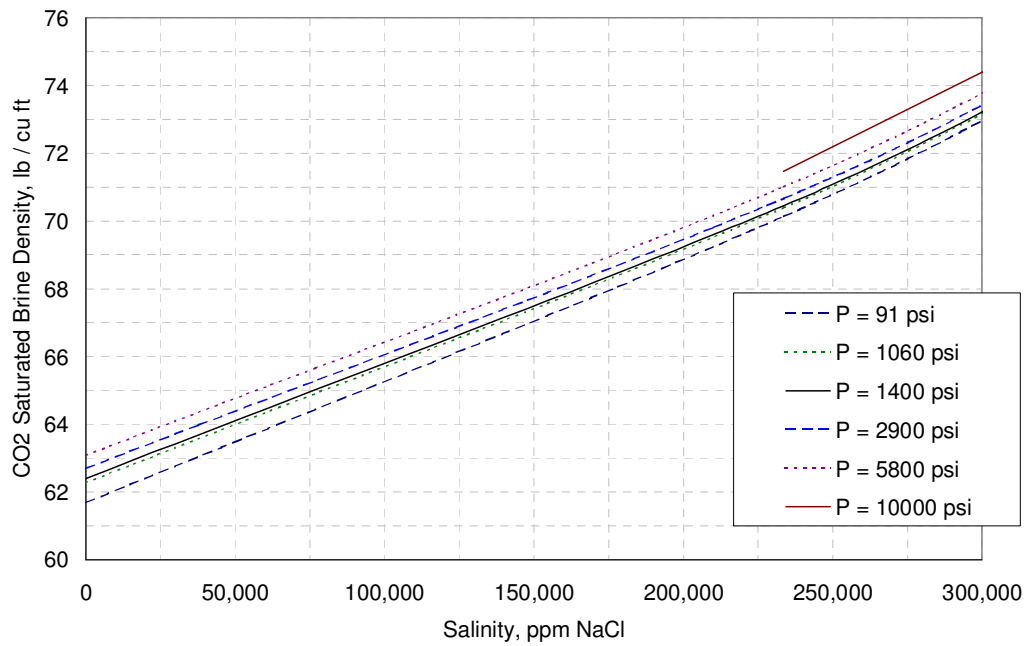


Figure I.10: Effect of Salinity on CO2-saturated Brine Density, T = 140 °F

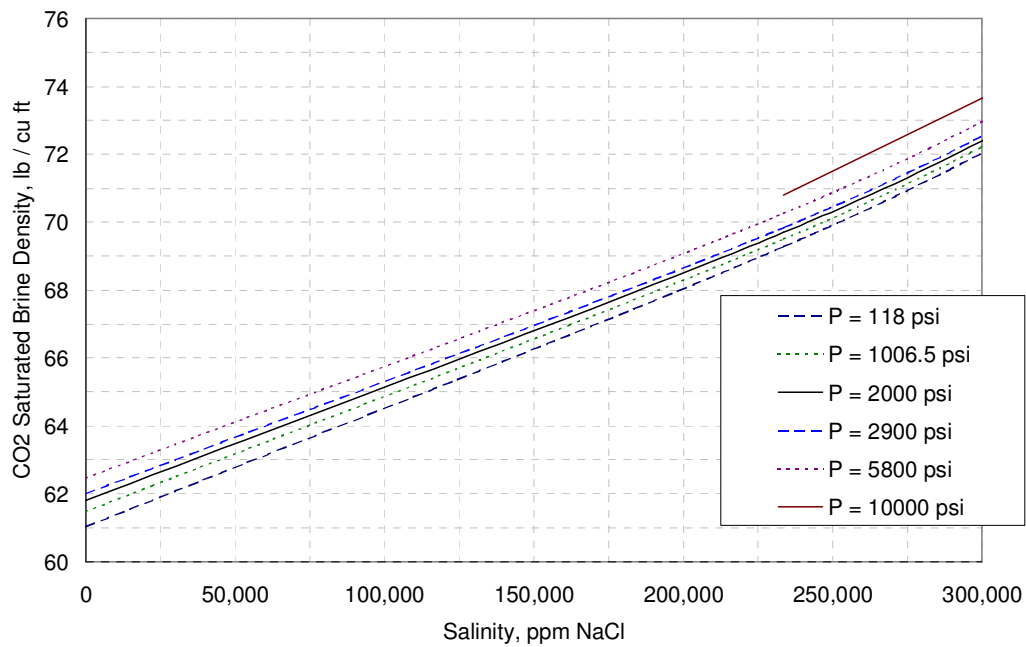


Figure I.11: Effect of Salinity on CO2-saturated Brine Density, T = 176 °F

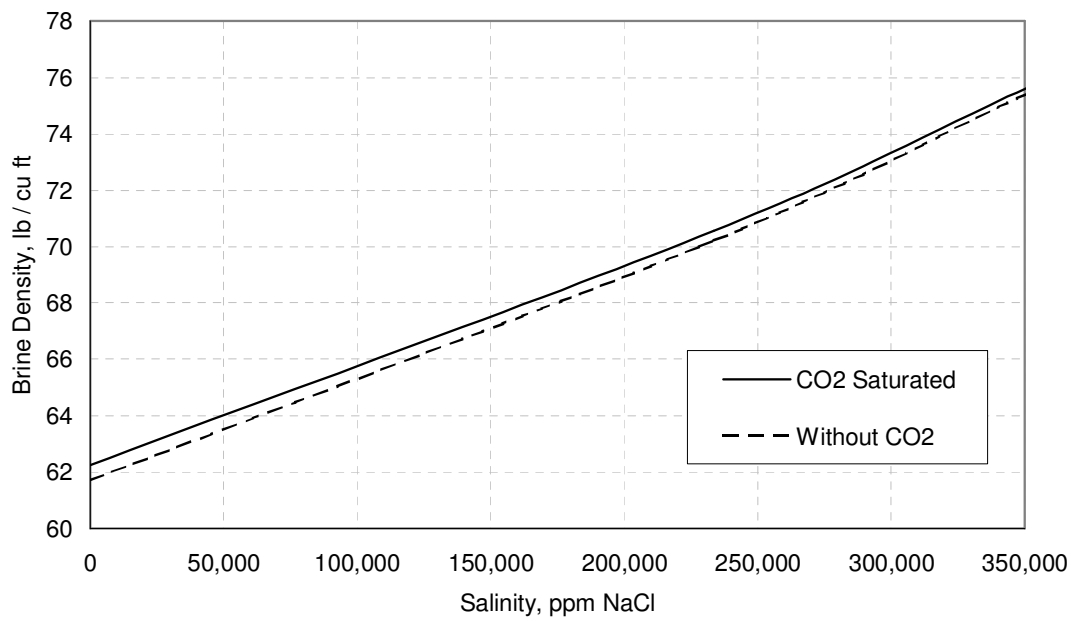


Figure I.12: Effect of CO2 Dissolution on Brine Density, T = 140 °F & P = 1000 psi

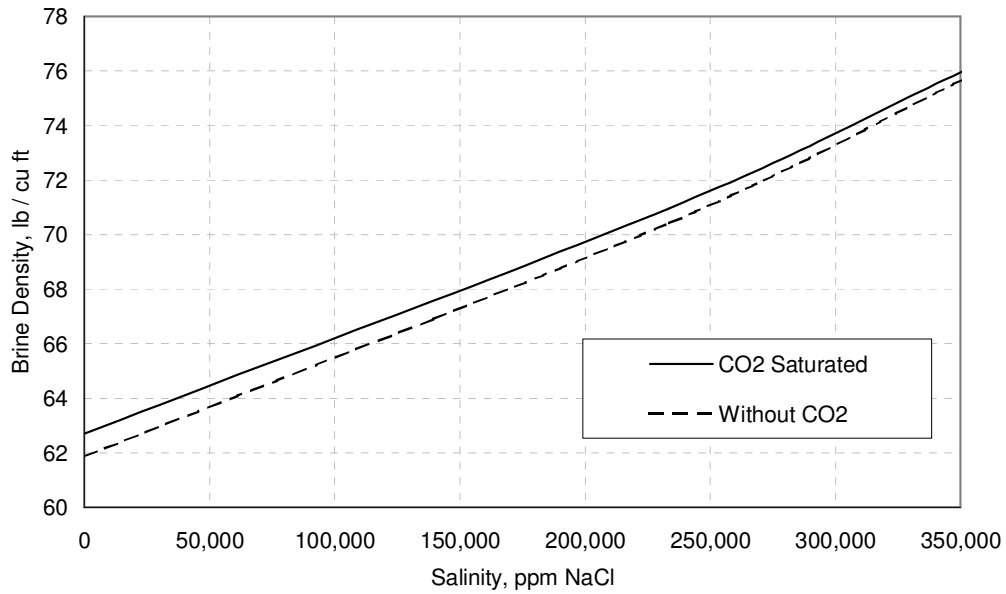


Figure I.13: Effect of CO2 Dissolution on Brine Density, T = 140 °F & P = 3000 psi

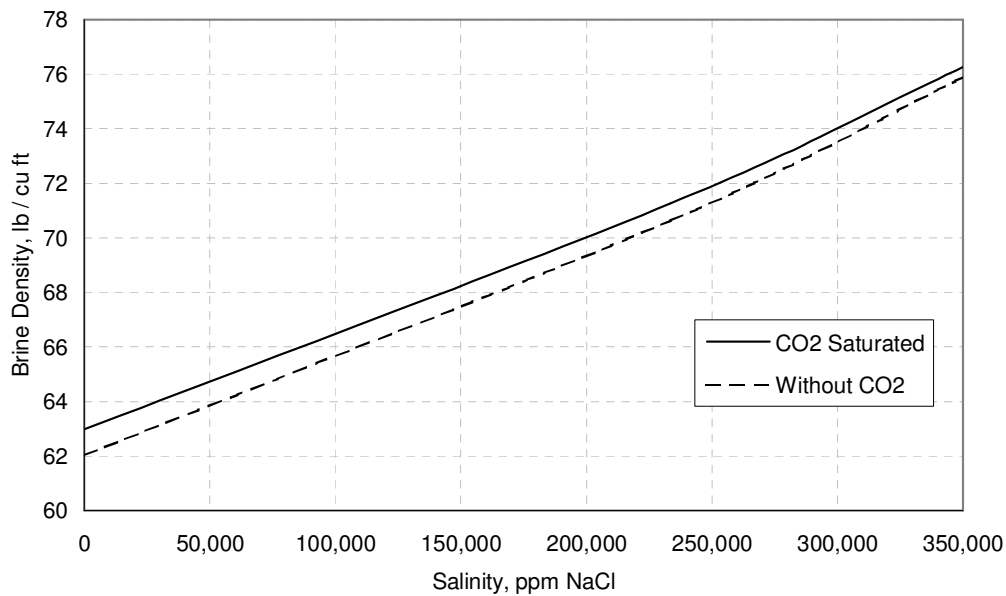


Figure I.14: Effect of CO2 Dissolution on Brine Density, T = 140 °F & P = 5000 psi

APPENDIX II

ROCK PHYSICS MODEL FOR WEYBURN OILFIELD

Encana provided with rock-physics model for the Weyburn oilfield. These were derived from various experimental studies done and are discussed in Syhlonyk (1998). The geologic sections considered for time-lapse study and the corresponding reservoir simulation layers are shown in Table 4.1. Pore pressure ($pore_pres$), water (S_w), oil (S_o), and gas (S_g) saturation, water (ρ_w), oil (ρ_o), and gas (ρ_g) density, and total fluid compressibility (c_{tot}) values at any time is derived from the compositional reservoir simulator. Porosity (ϕ) is assumed to remain constant. Other inputs used in this study are σ_{vert} , σ_{horz_min} , and compression axis pressure ($comp_axis_pres$).

Rock-physics model for marly section is discussed in Section 4.2. The following equations show the steps considered in the calculation for vuggy sections.

Upper Vuggy:

Net overburden pressure, $nob_pres = comp_axis_pres - pore_pres$

Total fluid density, $\rho_{tot} = \rho_w \times S_w + \rho_o \times S_o + \rho_g \times S_g$

Overall density, $\rho = \rho_m + \rho_{dp} + \rho_{df}$, where

$$\text{Matrix density, } \rho_m = 2679.6 \times (1 - \phi)$$

$$\text{Pore density, } \rho_{dp} = 0.$$

$$\text{Pore-fluid density, } \rho_{df} = \rho_{tot} \times \phi$$

Overall shear modulus, $\mu = \mu_m + \mu_{dp} + \mu_{df}$, where

$$\text{Matrix shear modulus, } \mu_m = -69.185 \times (\phi) + 26.352$$

$$\text{Pore shear modulus, } \mu_{dp} = 0.69 \times \log(\text{nob_pres}) - 1.95$$

$$\text{Pore-fluid shear modulus, } \mu_{df} = 0.$$

$$kf_{\log s} = 0.9$$

$$k_{\log s} = -186.09 \times \phi + 49.154 + (1.72 \times \log(\text{nob_pres}) - 4.99) \\ + (2/3) \times (-69.185 \times \phi + 26.352 + (0.69 \times \log(\text{nob_pres}) - 1.95))$$

$$k_s = 49.154 + 1.72 \times \log(\text{nob_pres}) - 4.88 \\ + (2/3) \times (26.352 + 0.69 \times \log(\text{nob_pres}) - 1.95)$$

$$k_* = (k_{\log s} \times ((\phi \times k_s / kf_{\log s}) + 1 - \phi) - k_s) / ((\phi \times k_s / kf_{\log s}) + k_{\log s} / k_s - 1 - \phi)$$

Bulk compressibility,

$$c_{bulk} = (\phi \times c_* \times (c_s - c_{tot}) + c_s \times (c_s - c_*)) / (\phi \times (c_s - c_{tot}) + (c_s - c_*))$$

Where

$$c_s = 1/k_s$$

$$c_* = 1/k_*$$

Bulk moduli, $k_{bulk} = 1/c_{bulk}$

$$\lambda = k_{bulk} - (2/3) \times \mu$$

$$\text{P-wave velocity, } V_p = \left(\frac{\lambda + 2\mu}{\rho} \times 10^9 \right)^{0.5}$$

$$\text{S-wave velocity, } V_s = \left(\frac{\mu}{\rho} \times 10^9 \right)^{0.5}$$

$$\text{P-wave impedance, } I_p = \rho \times V_p$$

$$\text{S-wave impedance, } I_s = \rho \times V_s$$

Lower Vuggy:

Net overburden pressure, $nob_pres = comp_axis_pres - pore_pres$

Total fluid density, $\rho_{tot} = \rho_w \times S_w + \rho_o \times S_o + \rho_g \times S_g$

Overall density, $\rho = \rho_m + \rho_{dp} + \rho_{df}$, where

Matrix density, $\rho_m = 2782.0 \times (1 - \phi)$

Pore density, $\rho_{dp} = 0$.

Pore-fluid density, $\rho_{df} = \rho_{tot} \times \phi$

Overall shear modulus, $\mu = \mu_m + \mu_{dp} + \mu_{df}$, where

Matrix shear modulus, $\mu_m = -57.242 \times (\phi) + 28.89$

Pore shear modulus, $\mu_{dp} = 0.69 \times \log(nob_pres) - 1.95$

Pore-fluid shear modulus, $\mu_{df} = 0$.

$$kf_{\log s} = 0.9$$

$$k_{\log s} = -166.47 \times \phi + 43.66 + (1.72 \times \log(nob_pres) - 4.99) \\ + (2/3) \times (-57.242 \times \phi + 28.89 + (0.69 \times \log(nob_pres) - 1.95))$$

$$k_s = 43.66 + 1.72 \times \log(nob_pres) - 4.99 \\ + (2/3) \times (28.89 + 0.69 \times \log(nob_pres) - 1.95)$$

$$k_* = (k_{\log s} \times ((\phi \times k_s / kf_{\log s}) + 1 - \phi) - k_s) / ((\phi \times k_s / kf_{\log s}) + k_{\log s} / k_s - 1 - \phi)$$

Bulk compressibility,

$$c_{bulk} = (\phi \times c_* \times (c_s - c_{tot}) + c_s \times (c_s - c_*)) / (\phi \times (c_s - c_{tot}) + (c_s - c_*))$$

Where

$$c_s = 1/k_s$$

$$c_* = 1/k_*$$

Bulk moduli, $k_{bulk} = 1/c_{bulk}$

$$\lambda = k_{bulk} - (2/3) \times \mu$$

$$\text{P-wave velocity, } V_p = \left(\frac{\lambda + 2\mu}{\rho} \times 10^9 \right)^{0.5}$$

$$\text{S-wave velocity, } V_s = \left(\frac{\mu}{\rho} \times 10^9 \right)^{0.5}$$

$$\text{P-wave impedance, } I_p = \rho \times V_p$$

$$\text{S-wave impedance, } I_s = \rho \times V_s$$

VITA

Name: Ajitabh Kumar

Email Address: ajitabh.kumar@gmail.com

Permanent Address: 3116 TAMU - 507 Richardson Building,
College Station, TX 77843.

Education:

B.Tech., Petroleum Engineering, Indian School of Mines, Dhanbad, 2001

M.S., Petroleum Engineering, The University of Texas at Austin, 2004

Ph.D., Petroleum Engineering, Texas A&M University, College Station, 2008